A PRAGMATIC APPROACH TO NANOSTAR PLASMONICS

By

THEODOROS V. TSOULOS

A dissertation submitted to the

School of Graduate Studies

Rutgers, The State University of New Jersey

In partial fulfillment of the requirements

For the degree of

Doctor of Philosophy

Graduate Program in Materials Science and Engineering

Written under the direction of

Laura Fabris

And approved by

_____

_____

_____

_____

New Brunswick, New Jersey

January, 2019

ABSTRACT OF THE DISSERTATION

A PRAGMATIC APPROACH TO NANOSTAR PLASMONICS

by THEODOROS V. TSOULOS

Dissertation Director:

Laura Fabris

Herein we present a new modeling approach to nanostar plasmonics that treats nanostar spikes as dual cavity systems where coupled bulk and surface polaritons propagate and form standing waves. Finite element simulations of the optical behavior of gold nanostars in water reveal a new view of collective electron cloud oscillations, where localized surface plasmon resonances coexist with coherent delocalized interface waves, i.e. propagating surface plasmons. Gold nanostar spikes long enough to allow propagating polaritons, and short enough to resonate with the spherical core, serve as the substrate for the observed overlap between propagating modes and localized ones. Transverse plane plots reveal bulk polaritons coupled to surface polaritons. In light of these, we explore the mechanisms that drive the plasmonic coupling in nanostars from the single spike level to multi-spiked systems and to complex interparticle coupling ensembles. Our successful predictions in experimentally synthesized systems of increasing complexity allow us to test our method in various regimes.

First, we explore changes in gold nanostar spike resonances when SiO_2 shells are progressively grown onto the spikes. As the SiO_2 layer thickens, the plasmonic enhancement dampens reaching a minimum due to the disrupted polaritonic coupling

on the spikes. We determine a strong correlation between the nanostar morphology and its silica coating layer, the enhanced electric field, and the surface enhanced Raman scattering (SERS) signal enhancements. The modelled behavior is expressed in terms of power losses maxima and it is compared to the experimentally measured SERS signal enhancement, as both values depend on the absolute value of the electric field. A successful prediction of the trend secures the applicability of our modelling approach to systems with spatially varying and frequency dependent dielectric functions.

We then calculate the shape dependent extinction coefficient, the volume, and the surface area of that real particle by introducing a detailed nanostar tomogram into our computational method and calculating its electric field under illumination with 8 different polarization orientations. In comparison to a semi-empirical, simplified model, used to calculate the same fundamental physical and optical parameters, which assumes a perfectly spherical core and identical protruding spikes, and other methods from bibliography, and based on the close agreement among the values obtained with the various approaches, we are confident that our method could be generalized for nanostars of any dimensions and arbitrary shape synthesized in solution using seed-mediated protocols.

Having successfully applied our approach to structurally anisotropic particles, we propose a method for the rational design of plasmonic particles. Using the conclusions from our computational study and working in parallel with a synthetic team we establish a causal relationship between structural and plasmonic properties. By way of comparison between the observed shifts and the spectral positions of the various resonances in the experiment and the model, we use this relationship to fine

tune the synthesis. Having optimized the synthesis, we focus on the resonances from the isolated single particle level studied via Ultra-Scanning Transmission Electron Microscopy and Electron Energy Loss Spectroscopy (Ultra-STEM EELS), to the highly coupled ensemble level studied via Attenuated Total Reflectance Fourier Transform Infrared Spectroscopy (FTIR-ATR). A new resonant window is covered, stretching to wavelengths in the short- wave infrared (SWIR). We have also showcased a method to determine the level of monodispersity and thus the applicability of our emerging method.

In brief, we have developed a numerical approach for the detailed study of gold nanostars. Tested in anisotropic, asymmetric, and arbitrary shaped systems it proved to be a useful tool for accurate predictions of the optical and the physical properties of plasmonic particles. We utilized this approach for the development of an emerging form of a plasmonic material that covers new grounds in how far, how strong, and how narrow these particles can resonate and enhance the impinging electric field.

Acknowledgements

I would like to acknowledge first and foremost the guidance, the support, the patience and most of all the creatively interactive mindset of my advisor, mentor and one of my dearest true friends Dr Laura Fabris. The present thesis is a miniscule example of the ways that my investigative and perceptive skills have evolved under her leadership.

Throughout the past four years we worked with several investigators that should be acknowledged here. Namely, I would like to thank Dr Philip E. Batson for all the intriguing discussions, the trust and the collaborative spirit, Dr Maureen J. Lagos for his persistent questions and microscopy training, Dr Huolin Xin for the solid microscopy work, Dr George Tsilomelekis for the infrared spectroscopy measurements and Dr Eric Stach for his high-resolution microscopy work.

From the Fabris group I have to acknowledge Mr Supriya Atta for the hours spent in the lab and the synthesis work, Dr Manjari Bhamidipati for the interaction and investigative partnership and Ms Jennifer Weir for her synthesis contribution.

Saepe stilum vertas, iterum quae digna legi sint scriptures.

Satirae, Quintus Horatius Flaccus

Table of Contents Page #

Tables

Page #

Illustrations

Introduction

Gold nanostars have emerged as the cornerstone among plasmonic nanoparticles with respect to resonant strength and tunability. We nonetheless think that they have not yet unraveled their full potential. These gold nanoantennas have shown to possess plasmonic properties with the potential to enable technological breakthroughs in various fields, such as imaging,[1] sensing,[2] and catalysis.[3] Importantly, their limited cytotoxicity[4] promises to enable their use *in vitro* and *in vivo*. However, despite the wealth of applied work[5-7] and the fundamental research both at the experimental and numerical level,[8-10] their application to solve technological challenges has been lagging behind. In addition to that, although broadly referred to as gold nanostars, these particles can show a wide range of morphologies and, therefore, plasmonic properties. As a consequence, both fundamental and applied research on gold nanostars has evolved and diverged rapidly. Accordingly, most of the latest works in the community treat this group of systems as well known and understood. On the contrary, we estimate that much of our fundamental understanding on these systems still shows gaps and inconsistencies.

In 2007, Hao *et al.* proposed a theoretical framework to describe the localized surface plasmon resonances (LSPR) of gold nanostars.[11] In this model, based on the *plasmon hybridization model*,[12] they suggested that the LSPR bands observed in the visible-near infrared (vis-NIR) can be described as hybrid resonances of those pertaining to the spherical core and the individual protruding spikes, leading to bright

and dark modes. They also showed that the position of the multipolar modes depends on the length and sharpness of the spikes, and their relative orientation with respect to the polarization of the incoming field, with longer and sharper spikes displaying more red-shifted resonances.[11] Notwithstanding the availability and the progress of powerful computational electromagnetic methods and the relevant research on related phenomena,[8-10] most of the works that followed did not generate a conversation that could connect the theoretical knowledge established in the 2007 work[11] to the development of reliable technologies. Arguably, one of the reasons hampering this implementation has been the lack of synthetic protocols ensuring sufficient monodispersity and batch-to-batch reproducibility. A limited sample monodispersity yields substantially broadened LSPR bands that cannot be used to unequivocally correlate morphology to plasmonic modes, leading to the necessity to carry out single particle studies, which can be neither straightforward nor scalable.

Contrary to nanostar systems, gold nanorods and nanowires have been successfully studied and understood, and they are now well-established nanomaterials leveraged for technological applications. The clear structure-property relationships that describe their plasmonic behavior has led to their use for the study of localized and propagating plasmons[13-14] and to demonstrate the concept of wave-particle duality.[15] Regardless of the notable improvement in the synthetic protocols, that now achieve monodispersed nanorods with high tunability,[16] and the decrease in plasmon band width through post-synthetic manipulations,[17] the 1D morphology of nanorods and nanowires limits their ability to probe the tridimensional space, unless 3D self-assembly protocols are employed[18]. On the other hand, owing to their inherent tridimensionality, and the numerous possible structural combinations, gold nanostars

are ideally suited for this purpose.

By realizing that nanostars represent the epitome of a 3D plasmonic antenna we strategized a way to connect the dots between the seminal theoretical studies in the field[11], the various types of nanostars and their accompanying plasmonic properties to the need for consistent synthetic methods that result in monodispersed and tunable (thus applicable) plasmonic particles. Starting from a thorough computational investigation that examines gold nanostars from the single spike level to that of a 50-spiked particle, we explored various structural anisotropies and dielectric function spatial variations as, for instance, the selective SiO_2 coating of the spikes and its role on the plasmonic response of the nanostars. Taking a real and realistic, hence pragmatic, look of an actual nanoscale gold star, we explore how to treat real systems and connect the dots between the actual shape of one particle and the cumulative properties of a synthesized colloid. We conclude with focusing on a form of a plasmonic nanostar with few and long spikes that spans a wide resonant window from 500 nm to 2000 nm while exhibiting narrow and tunable resonances. We propose the latter as an ideal form of a gold nanostar for further exploration of the fundamental plasmonic properties and as an actually scalable and applicable nanomaterial.

At this point we would like to outline the evolution of the understanding of gold nanostar systems since the first reported synthesis in 2006,[19] while addressing our proposed hypothesis of the coexistence of SPPs and LSPs on nanostar spikes, in comparison to systems where the interplay between these two different forms of plasmon resonances justifies their possible connection and coupling. Starting from the first reported synthesis of gold star-shaped particles in 2006,[19] we have to mention the

first use of the particles in SERS in 2008,[20] and the first and most notable nanostar modelling work in 2007.[11] Since then, there have been a few works addressing modeling of gold nanostars via the Finite Element Method (FEM),[21-22] in 2012 and 2015 respectively and the Finite Difference Time Domain (FDTD) method[23] in 2018. While reproducing the results by Nordlander and coworkers[11] these works do not provide with any new insight or deeper understanding of the system(s). For this we have to focus on systems like Insulator-Metal-Insulator (IMI) waveguides[24] and nanowires[25]. IMIs can provide us with an insight of our system as a double cavity interface (interfaces on the spikes enclaving the bulk gold of the nanostar spike) and nanowires can stand as a proof that polaritons can propagate on long nanostar spikes. These two combined with the observation of bulk plasmons[26] in plasmonic particles and powered by the idea of polariton-localized plasmon coupling[27] and interplay,[28] drive us to shape the two core hypotheses of this thesis. 1) The coupling between localized plasmon modes and polariton standing waves on nanostar spikes, 2) the coupling and orthogonality between the interface and the bulk modes.

Chapter I: Interface and Bulk Standing Waves Drive the Coupling of Plasmonic Nanostar Antennas

In 2003 Nordlander and coworkers first proposed a working model for explaining the coupling and the spectral positions of plasmonic resonances, in which they explained the plasmonic properties of nanoshells, nanocavities, and nanosphere systems, and generalized the model for more complex nanostructures[12]. In 2007 they also showed that the spectral position of plasmonic resonances on gold nanostars depends on the spike length, the spike sharpness, and the spike orientation with respect to the polarization of the incoming field [11]. Briefly, they showed that both longer and sharper spikes cause a red shift of the plasmon resonance, with the latter being weaker when not oriented along the polarization axis of the incoming field. They also concluded that the plasmon modes of nanostars are the result of the hybridization of plasmons associated with the spherical core and the tips. Since this first paper, only few additional studies on the fundamental properties of gold nanostars have been reported[10, 22].

Motivated by recent exciting applications of gold nanostars by our group and others[1-2, 7] and realizing that the potential of these nanoparticles will never be fully exploited unless we come to terms with the complexity of their optical and structural properties, herein we report a detailed computational work that delves deep into the origin and behavior of their plasmonic resonances. Our model dials back on the complexity of these particles by describing them as a system of discrete geometrical entities with distinguished contributions to the resonant modes, while treating them computationally as inseparable units in the 3D space. This approach takes a unique

stance on plasmonic coupling. Starting from the excellent agreement with previous results on the core-to-spike coupling[11] , we further explore the contribution of the tips and spikes as discrete units. More importantly, we study the plasmonic coupling between spikes starting from one spike and gradually building up to obtain complex, realistic nanostars. In doing so, we explore the interplay between symmetry and polarization as a key factor to peak shifting and merging. In view of these results, and in particular of the calculated electric field norm transverse plane plots, we propose a new view of plasmonic resonances in gold nanostars, which is strengthened by the predicted and observed mode shifts for nanostar pairs coupling in tridimensional space.

Our hypothesis treats the plasmon resonances of nanostars as coupled interface and bulk standing waves. Interface waves of charge occur when plasmon resonances arise on the spikes of plasmonic nanostars as localized plasmons. These charge waves couple to image charge waves in the bulk and propagate together along the spikes giving rise to hot spots at the tips. Gold nanostar spikes long enough to exhibit various harmonics of the fundamental mode shine a light on the nature of these resonances. These coupled interface-bulk standing waves can be similar in nature to surface plasmon polaritons but with a coupling mechanism that follows the behavior observed for localized plasmons. Most of the previously reported work on plasmonic nanoantennas[15, 29-31] has studied the plasmonic resonances of 3D materials as functions of shape and size of one geometrical entity. In our approach, the nanostars are treated as an assembly of inseparable (thus coupled) constituent 3D units (the spikes). As a result, they can sustain propagating plasmons that couple at the metal-dielectric interface of the spikes, while exhibiting intense concentration of

the localized surface plasmon resonances at the tips (hot spots), in an interesting pattern mediated by the electron reservoir represented by the core.

The works of Ritchie[32] and others[33-36] have established that surface plasmon polaritons (SPP) can propagate on metal-dielectric interfaces when the incoming light couples to the interface under restrictive wavevector matching conditions. The wavelength of an SPP is shorter than that of the incoming light and experimental evidence has shown that SPPs can trap light in subwavelength spaces[37-38]. *Au contraire*, localized surface plasmons (LSPs) are described as resonances that arise under illumination with no restrictive wavevector matching conditions. They are highly dependent on the morphology of the nanoparticle, being more confined in locations with small radius of curvature.

Bulk plasmons have been thoroughly studied via electron energy loss spectroscopy (EELS)[39] but they have not been addressed in colloidal plasmonics literature, except in some few cases[26]. They are usually referred to as *volume plasmons*[40-41], implying that the skin depth of gold (20-25 nm in the 500-2000 nm range) allows the plasmonic wave to evanescently travel within these few nanometers inside the particle. Considering that the nanoparticles studied here are characterized by features that do not surpass 20 nm in thickness in any dimension, we suggest that these nanostars could be ideal models for the investigation of bulk-to-surface plasmon coupling.

In brief, our hypothesis starts with coupling of light by means of localized plasmons on nanostars and then treats these plasmons as coupled standing waves of bulk and interface charges, that is, propagating plasmons in a two-sided cavity represented by the bulk and the interface of the spikes. Because of their intrinsically

different nature, SPPs and LSPs have never, to the best of our knowledge, been studied together on the same colloidal nanostructure, except in some cases that focused on their interplay[28, 42]. From an experimental standpoint, this has been due primarily to the lack of synthetic protocols that could yield nanoparticles presenting both long and sharp features with high sample monodispersity and reproducibility that could be used to confirm the theoretical predictions. In a recent work,[43] we demonstrated how this unique nanoparticle can be designed, synthesized, and plasmonically characterized to establish a validated platform supporting the hypothesis described here.

The Begrenzung Effect on a Single Spike Nanostar

To provide a deep understanding on the effect of the morphology on the optical properties of nanostars, and thus clearly define structure-property relationships for these nanoparticles, we have developed a computational model of increasing complexity, starting from that of a 1-spike nanostar (i.e. a spherical core with an individual spike, **Figure 1** and **Figure S1**), to end with a complex 50-spike model that reproduces the resonances of experimentally synthesized nanostars with an excellent degree of accuracy.

In **Figure 1** we report the wavelength dependence of the absorption cross section for an 80 nm 1-spike nanostar, in which the first (1340 nm), second (825 nm), and third (665 nm) harmonics can be observed. The energies at which these harmonics occur seem to follow a pattern unique to the shape and size of this 1-spike nanostar. Contrary to what is expected in one-dimensional systems (e.g. standing waves on a string), there is no frequency doubling (or tripling) between these harmonics; instead,

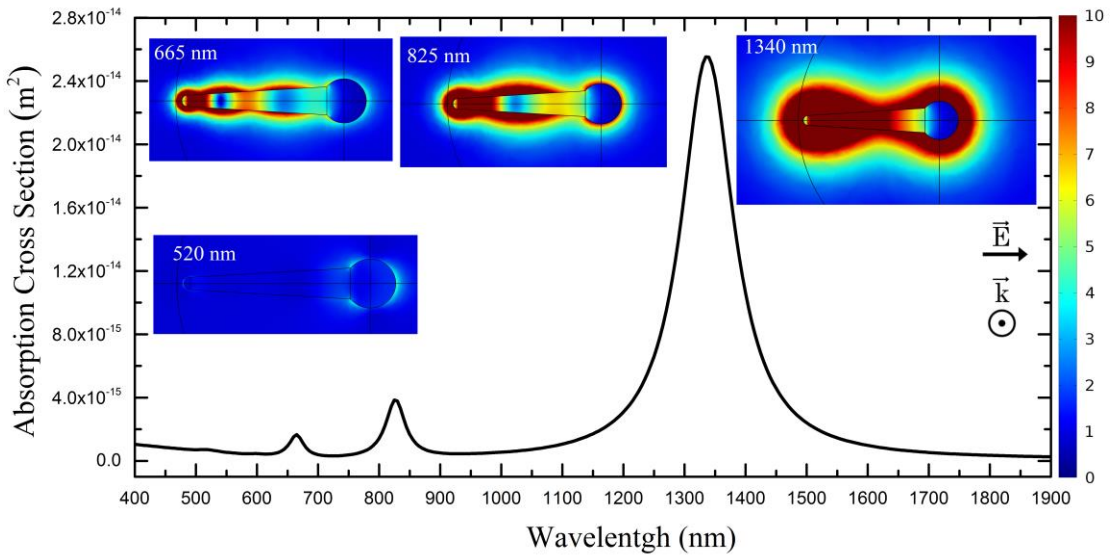

Figure 1. Absorption cross section spectrum of a nanostar with a single 80 nm length spike along with 2D slices of the calculated E-field norm (Equation 5 in Methods). In the scale bar, 1 represents the incoming electric field. Three plasmon resonance modes can be observed in the spectrum; the first harmonic at 1340 nm, the second harmonic at 825 nm, and the third harmonic at 665 nm. At 520 nm it is also possible to observe the isotropic resonant mode of the spherical core which, however, is only minimally enhanced when compared, on the same scale, to the other modes. Importantly, the intensity of the first harmonic is roughly one order of magnitude more intense than the second harmonic, which could be of great importance when designing these particles for specific applications. In the 2D slices extracted from the 3D solution of the electric field it is possible to observe the presence of bulk modes coexisting in node-antinode configuration with their surface counterparts.

there is a 1.62 ratio between the energies of the first and the second harmonic and a 2.00 ratio between the energies of the first and the third harmonic. As a consequence, the resonant bands appear to be squeezed within a shorter wavelength range compared to a 1D case due to the conical shape of the spike. Furthermore, these energy

ratios notably increase for sharper spikes, as seen in **Figure 2** (a and b) below. Both behaviors can be ascribed to longer propagation lengths of the SPP standing waves as the sharpness of the spike increases. Given the same spike length, conical spikes possess longer slant lengths compared to rod-shape spikes, providing longer wave propagation lengths. Because our method is a 3D numerical solution of a Laplacian in charge *continuum*, the result supports our hypothesis that this behavior resembles that of standing waves of SPPs. These harmonics of SPPs can be also interpreted as dipolar and multipolar resonances[29-30, 44]; however, we herein propose a more holistic approach, in which we treat the plasmon resonances observed on the spikes as the sum of propagating SPPs.

Considering our results as a sum over all possible plasmonic states, namely surface polaritons, image charge polaritons, and bulk polaritons, we propose a double cavity system, one cavity being the interface and one the bulk. It has been observed in silver nanospheres that bulk plasmons appear at higher energies compared to their surface counterparts[26]. Our results (Figure 1) seem to suggest however that in gold nanostars with high aspect ratio spikes, bulk plasmons in the spikes appear at the same energy as the surface modes. Another interpretation of this observation comes from considering the image charge waves resonating within the bulk to be the response of the surface charge oscillations. We can assume the bulk plasmons to be coupling to these image charges (due to their similar nature) and as a consequence to resonate with the surface modes. The importance of this observation is that both surface and bulk plasmons utilize a finite set of normal modes unique to the shape and dielectric characteristics of this gold nanostructure. More explicitly, when encountering a surface, a bulk plasmon reduces in intensity in its proximity, similar to how a SPP decays inside the bulk of a material. This was first described by Ritchie[32]

and it is known as the Begrenzung effect[45], sometimes referred to also as boundary rule or Begrenzung sum-rule[46]. This rule is found in a wider class of boundary problems[47] and can be described as a result of a sum rule over all plasmonic modes. To sum up, we treat the resonances observed in Figure 1 as harmonic modes of coupled bulk and surface propagating polaritons. As an unbiased result of a numerical FEM solution, we strongly believe that this conclusion can contribute to the establishment of rationalized structure-property relationship between nanostars and their plasmonic resonances, shining some light on the complicated nature of plasmonic coupling in these structures.

Quantifying the plasmonic shifts

Changes in tip morphology bring about more drastic shifts in the resonant bands than we had initially anticipated, as seen in **Figure 2**. In particular, we have analyzed the effect of the spike sharpness with respect to changing the ratio between the base and tip radii while the base radius is kept constant (Figure 2a). We have also studied the effect of the spike's thickness (i.e. the base radius) at constant radii ratio, and the role of the tip's sharpness (Figure 2c). Furthermore, we have analyzed the case in which spherical protuberances are located at the tip of the spike, effectively serving as electron reservoirs; this particular tip morphology can be observed in some of the kinetically-trapped nanostars we can synthesize following our recently published protocol[43]. Briefly, sharper spikes and sharper tips cause red shifting of the plasmon resonances of the spike; increasing the ratio by 0.1 redshifts the second harmonic by 40 nm (Figure 2a), making the spikes thinner by 2 nm in base diameter redshifts the second harmonic by 75 to 200 nm (Figure 2b), while sharpening the spike

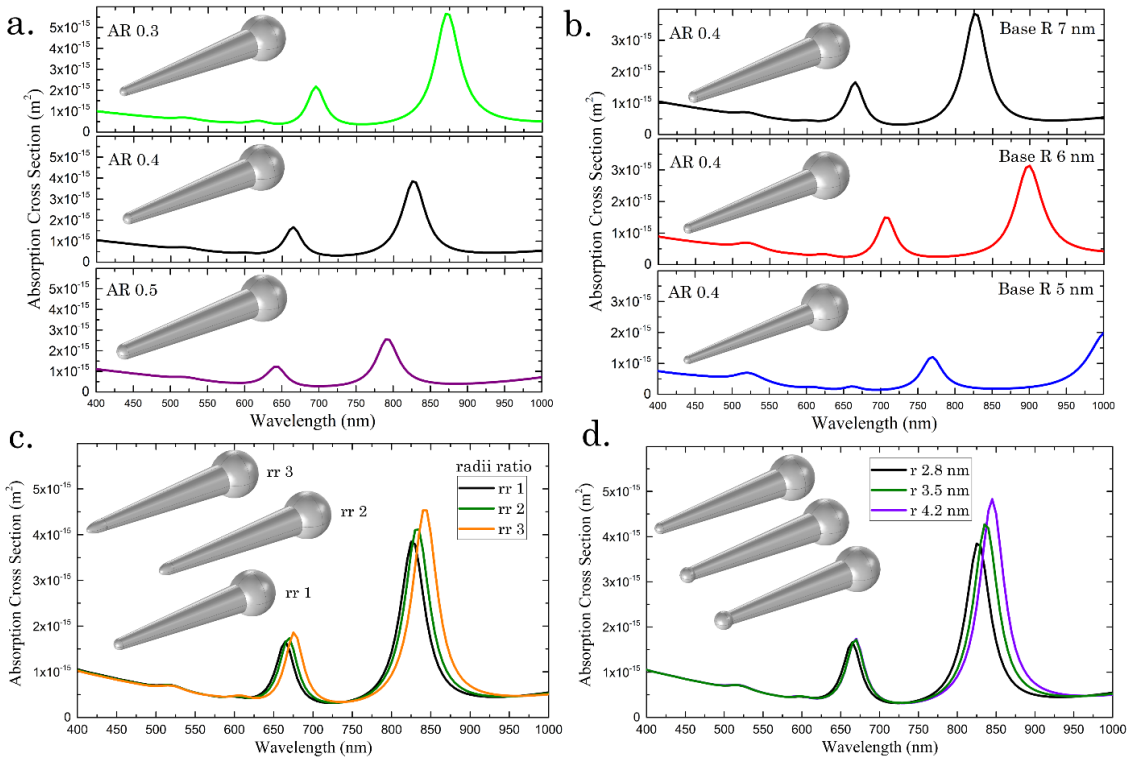

Figure 2. Dependence of the position of the second and third harmonics of SPPs on the morphology of the tip. a) Ratio between the radii of the base and the tip of the spike. Increase of the ratio leads to blue shifting of the resonances and a decrease in the distance between second and third harmonic. b) Base radius of the spike. Increase of the radius leads to blue shifting of the resonance and a decrease of the peak intensity. c) Spike tip morphology. Red shifting of the resonant peaks occurs as the tip morphology goes from hemispherical to prolate spheroidal. *Radii* ratio 1 corresponds to hemispherical tips. d) Redshifting of the resonant peaks as spheres of increasing radius grow at the nanostar tips.

tips from hemispherical (*radii* ratio 1) to hemispheroidal (*radii* ratios 2 and 3) redshifts the second harmonic by 6 and 16 nm, respectively (Figure 2c). Additionally, we observe that when a spherical protuberance grows on the tip of the spike (Figure 2d) it causes the second harmonic band to progressively red-shift at increasing sphere

diameter, thus suggesting its role as a reservoir of electrons that can then couple to the spike's standing wave SPPs, effectively leading it to resonate at lower energies. This is in agreement with what we have previously observed when we were able to regiospecifically bind spherical nanoparticles to the tips of surfactant free gold nanostars at short interparticle gaps[48]. In this case, a 20-25% increase in the radius of the spherical protuberance induces a 9-10 nm plasmon redshift.

Building up the intraparticle coupling spike by spike

More insightful results emerge from the analytical study of the plasmonic modes of a 2-spike nanostar, in which a second identical spike is added to that presented in the model reported in Figure 1. In **Figure 3a** we show the results for collinear spikes (i.e. 180°) and spikes relatively oriented at 45° and 90°. In Figure 3a the coupling between the spikes at 180° redshifts the first harmonic by 310 nm compared to the one-spike case, as expected. Similar behavior is also observed for the second and third harmonic. In addition, the presence of the second spike almost doubles the intensity of the resonant bands, as expected from the additional volume of gold. When the spikes are arranged at 90° and 45°, they exhibit an additional band emerging (for this specific morphology) at 1200 nm. The two bands in the IR (at 1200 nm and 1650 nm) can be interpreted as two different dipolar resonances where the two-spikes and the two-spikes-and-core systems behave as different dipoles, implying that the spike-core interaction depends on the relative angle between the spikes. As a consequence, we can justify the presence of the secondary resonances as due to inter-antenna coupling. In the 90° case these secondary resonances are detectable even for the second and the third harmonics (at 875 nm and 675 nm respectively), as seen in

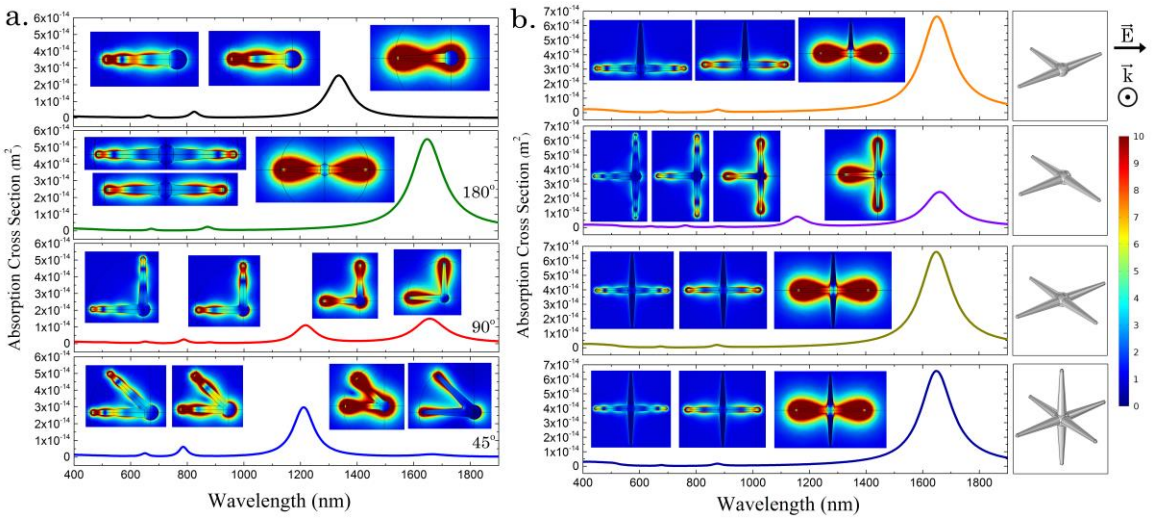

Figure 3. a) Absorption cross section spectra of a nanostar with a single 80 nm lenght spike and of nanostars with two spikes at 180, 90, and 45 degrees; 2D slices of the calculated E-field norm are also shown. Note the secondary resonances appearing in the cases of 90 and 45 degrees. b) Absorption cross section spectra of a nanostar with three spikes placed parallel to and at 90 degrees with respect to the E-field polarization, along with a 4-spike and a 6-spike nanostar with identical spikes, demonstrating the significance of the coupling with respect to collinearity and alignment with the incoming field polarization axis.

the Appendix II (**Figure S2**). Interestingly, in this case, the participation of the core to the second and the third harmonic makes the primary resonances notably stronger, as opposed to the first harmonic case, where the primary and secondary resonances are of comparable intensity. This can be explained as due to increasing gold conductivity as we move to the mid IR, where the first harmonic resonates[49]. Thus, the participation of the core, functioning as electron reservoir, is being overcome by the strength of the two resonating spikes in the mid IR region. In the 45° case the secondary resonant bands in the visible region seemingly disappear, while in reality

they become enveloped within the bandwidth of the main ones; in the short wave infrared (SWIR) the secondary band appears significantly attenuated. In **Figure 3b** we observe that the most important aspect in inter-spike coupling is the relative position of the spikes with respect to the E-field polarization axis. When adding a third spike perpendicularly to two collinear spikes aligned with the E-filed polarization axis, the resulting enhanced field or the spectral positions of the resonances do not appear to change. When doing the same but aligning the perpendicular spike with the

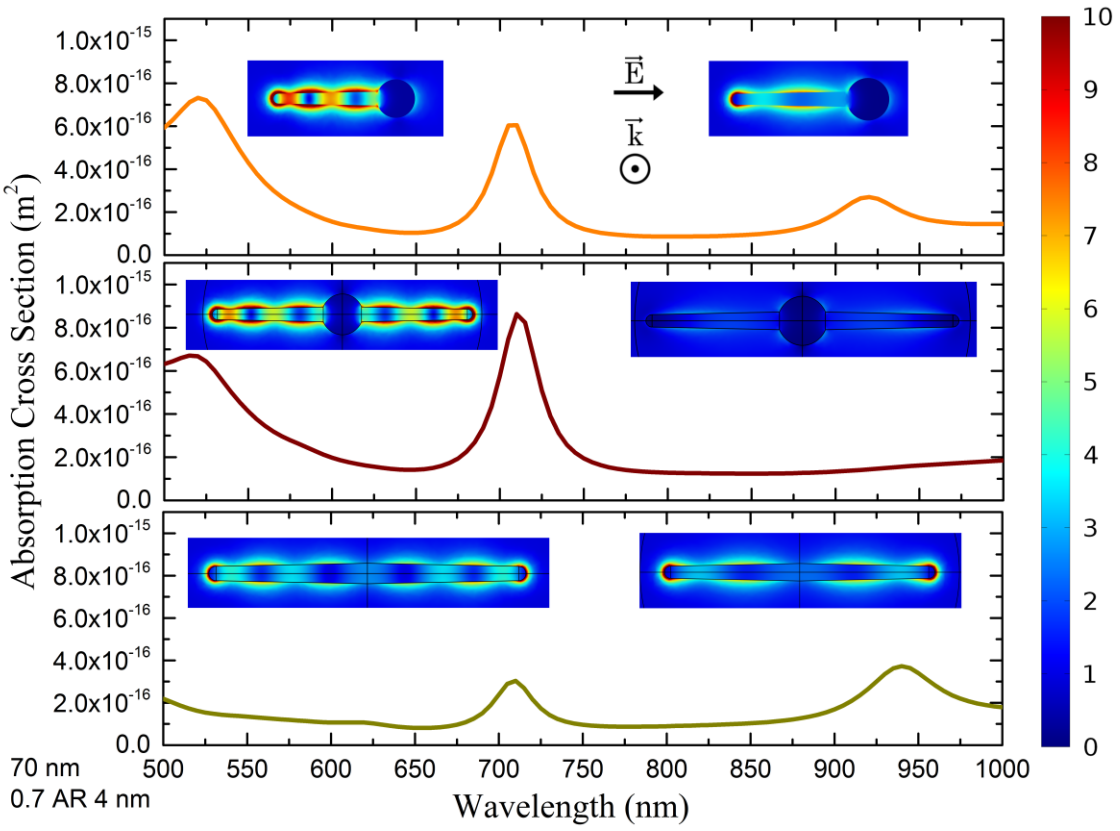

Figure 4. Comparison between absorption cross section spectra of a nanostar with an individual 70 nm spike, a 70 nm 2-spike nanostar, and two 70 nm spikes without the spherical core, along with 2D slices of the calculated E-field norm. Selective attenuation of the second harmonic only in the case of the 2 spike nanostar. A paradigm of destructive interference of SPP standing waves.

E-field polarization axis, we observe something similar to the 2-spike 90° case. However, in this case, the SWIR bands appear asymmetric in intensity, as the collinear spikes couple strongly despite being placed perpendicularly to the E-field polarization axis. Adding spikes symmetrically and creating a 4-spike and a 6-spike nanostar demonstrates that the strong coupling between the collinear spikes aligned along the field polarization axis overshadows all other secondary resonances. The angle-dependent core contribution, the effect of the spike collinearity, and the emerging secondary resonances are important aspects of this new physical interpretation.

Destructive SPP Interference Dampens the Second Harmonic

In **Figure 4** we present the comparison between a 70 nm 1-spike nanostar (base and tip radii ratio of 0.6), a 2-spike nanostar of the same dimensions, and a bipyramid consisting only of the two spikes without the spherical core. As expected, even in the presence of the core, the two identical spikes resonate at similar energies as they would in its absence, further reinforcing the hypothesis that the specific morphology of the spike drives the plasmonic properties. Surprisingly, while the third harmonic does not appear substantially shifted in all three cases, the second harmonic is attenuated to a vanishing point only in the case of the 2-spike star. We view the role of the core as an electron reservoir that interacts with the standing wave oscillating along the collinear spikes, as seen above, resembling the case of a double open-ended waveguide,[50-51] with the core being the closed-end and the spike tips being the open ends. This view suggests the possibility of the existence of a selection rule that phenomenologically translates into the observation of selectively dampened plasmonic

modes in this nanostructure. This selection rule seems to be unique to specific combinations of geometrical parameters, as almost the opposite effect is found in the case of two bipyramids (**Figure S4**), where the second harmonic is attenuated as opposed to what is observed here. This result suggests that there might be a limit in the relative size of the core and the closed-end effect. (We should note here that the core in Figure S2 is relatively smaller than the core in Figure 4). Comparing the same structures to longer length cases we also found an instance in which the second harmonic vanishes for both the bipyramid and the 2-spike nanostar case (Figure S4). The multiple instances in which we observe enhancement or damping of resonances for selected spike features solidifies our hypothesis for the existence of constructive and destructive SPP interference patterns.

Blue Shifts and Intraparticle Coupling

To further strengthen our interpretation, we present in **Figure 5** the inter-spike coupling effect in the case of an increasing number of centrosymmetric spikes (6, 14, 18, and 26). Symmetry allows us to disregard additional polarization-alignment related effects, as we have described in previous works[52-53] and above, thus enabling us to focus on the effect of the inter-spike coupling on the same nanostar. The observed effect is a clear blue-shift of 70, 110, and 175 nm (for the 1st harmonic) when increasing the number of spikes from 6 to 14, 18, and 26, respectively. The same trend is observed for the rest of the harmonics. This blue-shift is attributed to the inter-spike coupling, which amplifies the resonance hence pushing the resonant maximum to higher energies. One could argue that the spikes are merging at the base as we move up in spike number. To counter this argument, and prove that the shift

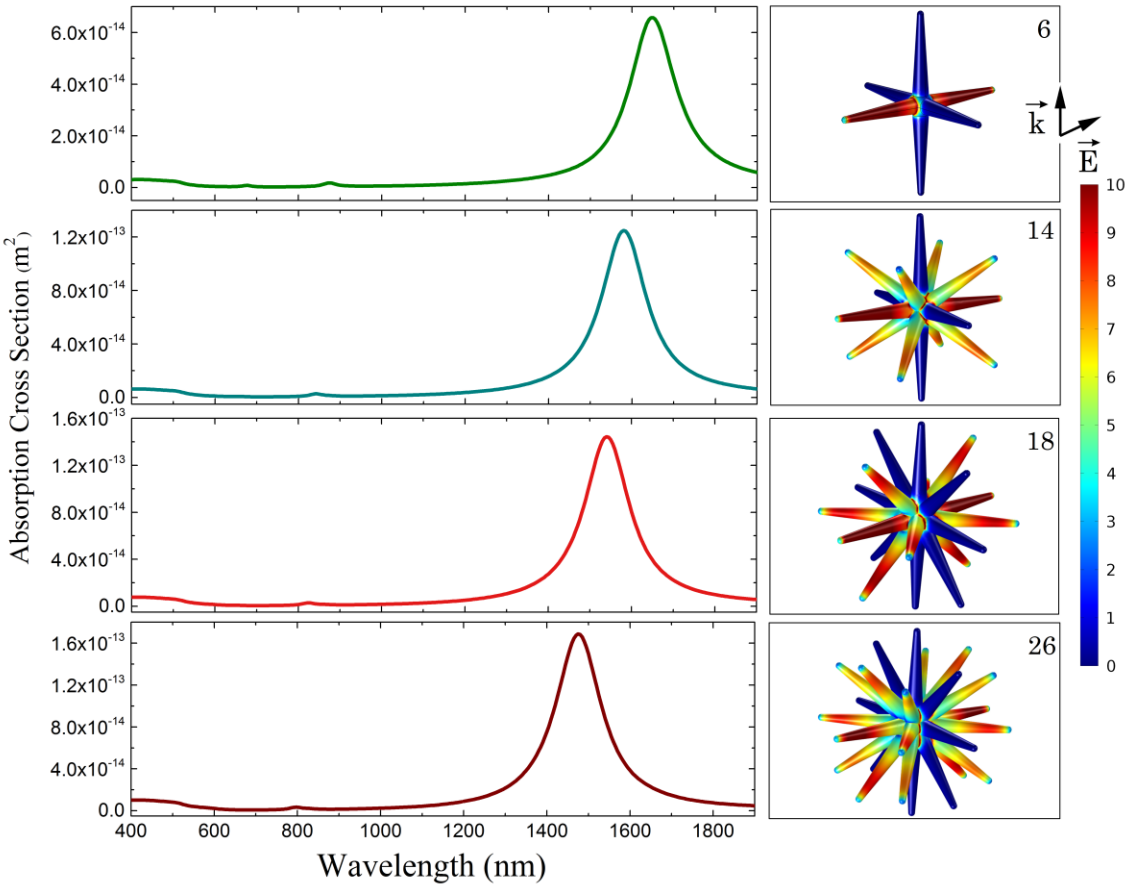

Figure 5. Comparison between the simulated absorption cross sections of nanostars with 6, 14, 18, and 26 spikes and their respective E-field norms mapped in 3D. Note the blue-shift that results from the increasing number of spikes. Inter-spike coupling appears to shift the resonant maxima to higher energies as spikes resonating in proximity feed each others plasmons.

originates only from the collective coupling of the spikes, we ran a test simulation with an oversized core decorated with 18, 26, and 50 spikes as found in **Figure S5**. The exact same blue-shift was observed, thus further supporting our conclusion. The way in which the inter-spike coupling occurs is similar to the case of destructive or constructive interference patterns in nanoantenna arrays, when the antennas are aligned in parallel[54]. The difference in our case is that the nanoantennas (i.e. the

spikes) are attached radially to the same particle which leads them to contribute to the intensity of the resonance in an angle-dependent manner. It should be noted here that the morphology of the spikes dictates the spectral position of the eigenmodes and the polarization alignment dictates the intensity of the resonances. By way of comparison to the isolated nanoantennas, our coupled SPPs-bulk polaritons hypothesis clarifies the inter-spike coupling blue-shift.

Predicting the properties of a highly asymmetric colloid with one symmetric model

To confirm the results of our theoretical approach, in **Figure 6** we compare the absorption spectrum of a 50-spike surfactant free gold nanostar to the modeled absorption cross section spectrum of a perfectly symmetric 50-spike nanostar model. The exact matching of the absorption cross section and the absorbance maxima allow us to conclude that, for a higher number of spikes, a simplified symmetric model of

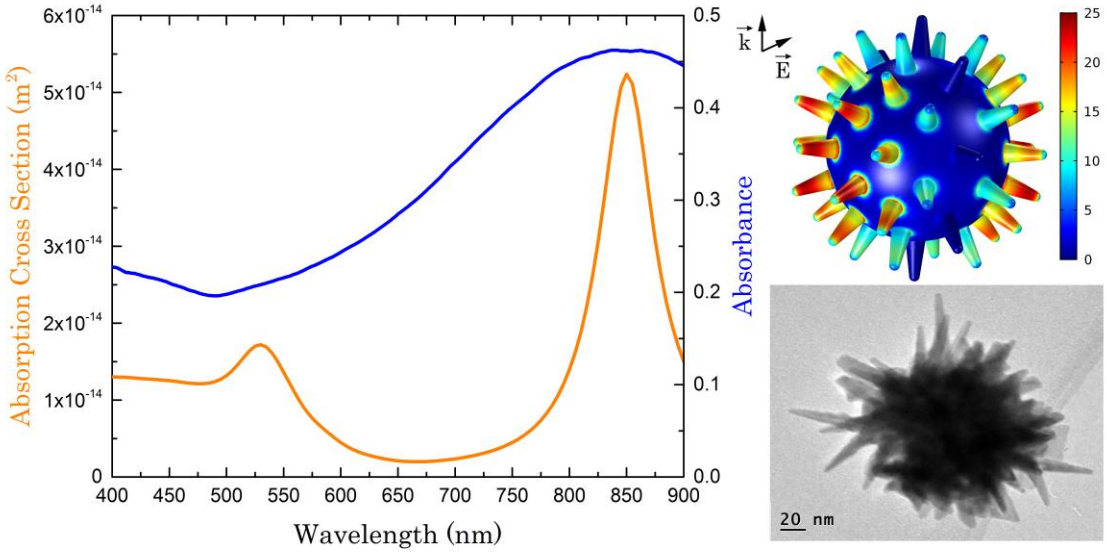

Figure 6. Comparison between the simulated absorption cross sections of a perfectly symmetric 50-spike nanostar model and a colloidal sample of synthesized nanostars of the same average dimensions.

our new approach is more than adequate to recapitulate the plasmonic behavior of a gold nanostar. This, again, also stands as an experimental proof for the inter-spike coupling study described so far.

Interparticle Coupling

We have explored the plasmonic coupling in gold nanostars from the simplest case of a single spike resonating with a core, to a highly entangled case of a 50-spike nanostar. In a synoptic attempt, we conclude with an even more complex form of coupling; the inter-particle coupling. For this study, we employ 6-spike nanostars with five in-plane spikes, experimentally observed when spikes grow from five-fold twinned defects of decahedral seeds, which are commonly observed in gold particles.[55] The in-plane spike configuration, apart from being effectively observed, represents an ideally symmetric model to establish a 3D plasmonic ruler for nanostar coupling, similar and in agreement to what previously reported in gold nanorods[56] and nanospheres[57]. In **Figure 7** we present the plasmonic shifts with respect to inter-particle distance for the resonant first harmonic peak in the case of the coupling of two nanostars under three different configurations. The distance in every case is defined as the physical separation between the metallic surfaces of the two adjacent nanostars. Interestingly, a red-shift is observed in a configuration where the in-plane spikes are kept in-plane as the nanostars are being moved along the E-field polarization axis, while a blue-shift behavior is observed in other configurations where the in-plane spikes are being moved out of plane while the nanostars are kept collinear along the light propagation axis. This draws a parallel to what has been previously observed in gold nanorods[56].

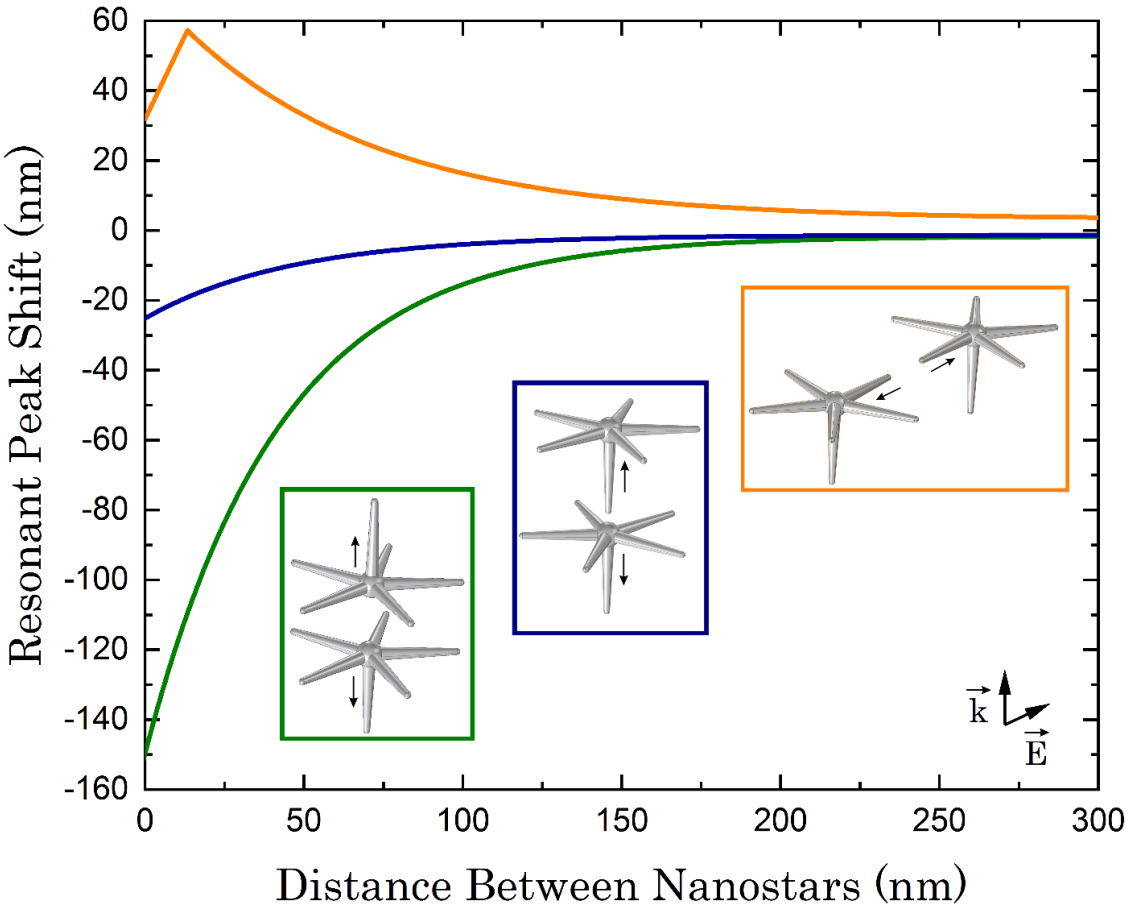

Figure 7. Inter-particle coupling between gold nanostars. When being moved along the E-field polarization axis, the nanostars resonate at red-shifted wavelenghts with linear distance dependence up to a maximum at 13 nm, and exponentially return to the initial resonance position at ~ 400 nm distance. When being moved along the light propagation axis, the nanostars resonate at blue-shifted wavelenghts. The blue shift depends mostly on the physical seaparation of the in-plane spikes and the blue-shift is exponentially reversed as the nanostars diverge, returning to the non-shifted resonance at ~ 200 nm distance.

For a more in-depth analysis of the first configuration, in which the nanostars are being moved along the polarization axis, in Figure 7 (orange curve) we can observe that for two touching nanostars there is a 32 nm red-shift of the first harmonic mode

compared to an isolated nanostar. When the distance between the nanostars increases a further red-shift up to 58 nm can be observed, which then reverses at 13 nm tip-to-tip separation and exponentially decays slowly to return to the single particle resonance position at approximately 400 nm, a distance indicative of the substantial coupling strength between gold nanostars of this shape. The linear region corresponds to the first few nanometers of separation between the tips coupling tip-to-tip. Within this region, because the first harmonic mode of the scattered enhanced field of the first nanostar reaches far enough to enter in resonance with the field localized at the core of the adjacent one, a strong coupling and red-shift occur, leading to an optimal interaction at ca. 13 nm. Beyond 13 nm of tip-to-tip separation the effect is reversed, as the coupling between the core and the spikes of the adjacent nanostars weakens, leading only the tips to interact, similar to two nanorods coupling tip-to-tip. In the case of the nanostars moved along the light propagation axis (green and blue curves), the in-plane spikes are the ones that drive the coupling phenomenon, as their physical separation dictates the strength of the coupling and thus the blue-shift. Although quite intense in close proximity as seen in Figure 7, the phenomenon weakens significantly at approximately 200 nm of physical separation in both configurations.

These theoretical predictions have been extremely useful to explain experimental observations within our recent combined experimental-theoretical work[43]. In ATF-FTIR experiments we reported in that work, additional side peaks appeared within the first harmonic mode when we increased the concentration of the nanostars. We were able to explain them by exploring different geometrical configurations between adjacent nanostars. Understanding the inter-particle coupling needs a solid understanding of the underlying phenomena, as those described in this work. Treating nanostar plasmon resonances as coupled bulk plasmon and surface

polaritons provides a useful insight toward this direction. After presenting how plasmonic coupling in nanostar spikes is driven by interface and bulk polaritons we are going to focus again on Figures 1 and 3. We are intrigued by the coupling pattern between bulk and surface modes. At first look they resonate with the same order-mode. However, with regards to their frequency domain image, the bulk plasmons exhibit maxima where the surface ones exhibit minima, and vice versa. A frequency domain study does indeed provide only a time averaged image of the electric field maps on our nanostructures and their surrounding media, which is indicative of a phase difference in coupled bulk and surface modes. However, at this stage we cannot conclusively state that bulk and surface modes resonate under a specific phase difference. For this we are developing a time-domain solution that we will present in the near future. Nevertheless, it is plausible that, given the skin depth of gold under optical and NIR frequencies, de-phased resonant modes of the same order inside star-shaped nanostructures might develop. This behavior fits well the paradigm of plasmonic nanoantennas resonating at their eigenfrequencies, when propagating SPPs form standing waves at the gold-water interface. Almost simultaneously, polarizing charges form standing waves inside the gold bulk that resonate under a phase difference with the interface SPPs. The existence of these polarizing charges in the bulk is justified by considering the maximum propagation lengths of SPPs in gold,[37] and the skin depth of gold at optical and infrared wavelengths. Seen from a different angle, the SPPs themselves carry enough energy for the creation of image charge waves in the bulk that can couple to the polarizing ones. The time frame of these phenomena could be quite interesting to investigate by further theoretical modeling in the time domain.

Chapter I conclusions

We have presented a new approach to gold nanostar plasmonics that treats the spikes as dual-cavity systems where coupled bulk and surface polaritons propagate and form standing waves. This approach treats localized plasmons as the initial coupling mechanism that allows the formation of standing waves by means of wavevector translation. We have described the mechanisms that drive plasmonic coupling of increasing complexity and confirmed the role of the core as electron reservoir, which becomes more relevant in selected configurations. Some of our predictions were successfully verified in systems of experimentally synthesized nanostars of increasing complexity, thus validating our coupling-based interpretation of plasmonic modes in nanoparticles with multiple high aspect ratio features. These verifications also confirmed the need of fully tridimensional, shape-sensitive, time domain models and experiments to verify the observed phase shifts between surface and bulk plasmons. In view of the ongoing expansion of electron microscopy techniques, such as EELS and cathodoluminescence, to probe plasmon resonances, and because the concept of bulk plasmons is a traditionally more studied phenomenon in electron microscopy, our work could provide an initial link toward a common interpretation of plasmon excitations involving both photons and electrons.

Chapter II: Predicting the Optical Properties of Selectively SiO_2 Coated Nanostars

In the past decade surface enhanced Raman spectroscopy (SERS) has grown to become one of the most important analytical techniques employed by the scientific community for highly sensitive, selective, and multiplexed detection of target molecules with minimal sample preparation, limited to no sensitivity to external conditions (e.g. photobleaching), and amenability to work in complex environments like living tissues.[58] By virtue of the SERS effect,[59] the intrinsically low Raman signals can be enhanced by over ten orders of magnitude when the analyte molecules are placed in close proximity to the surface of a plasmonic nanostructured material or located at so-called *hot spots*, i.e. locations such as edges, vertices, tips, or intermetallic junctions, where the local electric field is expected to be the highest.[60] It has now been well established that two mechanisms are responsible for this enhancement, namely the electromagnetic and the chemical, even though the former plays a dominant role.[61] When employing SERS for chemical analysis, the detection power of each SERS substrate is evaluated by calculating its enhancement factor (EF).[62] EFs depend on the local and impinging electric field as described in **Equation 1:**

$$EF_{EM} = EF_{EM}(\omega_L)EF_{EM}(\omega_R) = \frac{E_{Loc}(\omega_L)^2 E_{Loc}(\omega_R)^2}{E_0(\omega_L)^2 E_0(\omega_R)^2} \quad (1)$$

Here, EF_{EM} indicates the enhancement factor originating from the electromagnetic mechanism, ω_L and ω_R are the frequencies of the excitation and the emission, and E_0 and E_{Loc} indicate the impinging field and the local field at the analyte position,

respectively. When ω_L and ω_R are very close to each other, Equation 1 can be re-written as **Equation 2**:

(2) $$EF_{EM} = \frac{E_{Loc}(\omega_L)^4}{E_0(\omega_L)^4}$$

which brings us back to the well-known fourth-power relationship between EF and the electric field. Similarly, one can calculate the ratio between the SERS and the Raman signal intensities for a particular analyte, and correlate it to the local and impinging fields, as done in **Equation 3**, where any dependence on the polarizabilities is included within the proportionality factor:

(3) $$\frac{I_{SERS}}{I_{Raman}} \propto \frac{E_{Loc}^2(\omega_L)}{E_0^2(\omega_L)}$$

SERS enhancements can be improved by modulating the morphology of the nanostructured substrates 1) to introduce *hot spots* and 2) to bring the localized surface plasmon resonance (LSPR) to be resonant with the wavelength used for SERS analysis. An additional way by which it is possible to increase the SERS response is by modulating the molecular packing of the analyte on the surface of the nanostructure so that higher signals can be achieved. For this reason it is also important to obtain information on the surface properties of the nanostructure (e.g. its crystallography) and to understand how the affinity of specific functional groups for the metallic surface changes with the crystallographic properties, but this topic is beyond the scope of this chapter.

Among various types of plasmonic nanomaterials that can be used for SERS, gold and silver have been the most explored,[63-64] even though alternative metals such as aluminum have started to gain importance in applied plasmonics research community.[64] Gold, in particular, has been studied the most because of its stability and the possibility of manipulating it from the *bottom up* to obtain nanostructures of well-defined morphology that display extensive shelf life. One of the most interesting and perhaps most promising morphologies is the nanostar. Gold nanostars can be synthesized in solution employing both seed-mediated and seedless approaches,[65-66] and their morphology can be tuned to possess spikes of variable tip curvature protruding from the spherical core. Electric field enhancement in nanostars is due both to plasmonic contributions and to the lightning rod effect,[67] and for this reason these nanoparticles display the highest enhancement factors both in direct and indirect detection approaches, as demonstrated by us and others.[2, 68] However, although gold nanostars are widely used in a broad range of SERS and other plasmonic applications, only little is known about their fundamental properties, especially when referring to the case of real nanoparticles in suspension,[69-70] for which extreme LSPR band broadenings are observed.[2] For instance, the extinction coefficient of gold nanostars was only recently estimated and further information on their optical and physical properties is very scarce.[71] For these reasons, we have focused our efforts on understanding, both experimentally and in simulation, what are the various contributors to LSPR position and broadening in nanostars and how their morphology and surface functionalization can affect their electric field enhancement properties and, as a consequence, their applicability in SERS experiments.

In this chapter we discuss how we synthesized surfactant free gold nanostars following a seed-mediated protocol, coated them with silica, and selectively etched the glassy shell away so as to expose only variable amounts of the spike's surface. The nanoparticles were then employed for direct SERS experiments employing a model analyte, aminothiophenol (ATP), from which we then estimated how the signal enhancements depend on tip exposure. Furthermore, we have carried out finite element electromagnetic field simulations employing the software COMSOL Multiphysics and studied the origin of the LSPR broadening and the localization of the electric near field in 3D models of nanostars built following the morphologies observed experimentally. Our results show a strong correlation between nanostar morphology, silica shell thickness, electric field intensity and distribution, and SERS signal enhancements. We believe that our model could be useful to predict the effectiveness of a nanostar as field enhancer in SERS experiments even when its thorough characterization is lacking.

Nanostars as effective SERS platforms

With the increase in the number of applications in which gold nanostars have a fundamental role as near field enhancers,[72] we have become extremely interested in understanding how to rationally link their plasmonic properties to their morphology in order to produce the most effective SERS platforms. In particular, we wanted to find the best way to computationally predict the enhancement and spatial distribution of the electromagnetic near fields for nanostars with morphologies observed experimentally in order to rationally design synthetic protocols producing nanostar morphologies yielding the highest enhancement factors. Furthermore, we wanted to

prove experimentally that the nanostars computationally predicted to produce the highest scattered fields would indeed lead to the highest SERS signal enhancements. However, due to the morphological complexity of these nanostructures, selectively isolating locations on the metallic surface for Raman reporter binding can be experimentally problematic, if successful at all. Therefore, in order to simplify the issue, we have decided to approach it in a different way, that is, by selectively exposing only parts of the metallic surface at a time. In doing so, we wanted to be able to determine, by exclusion, the most effective combinations of nanostar morphology and surface functionalization, and to identify a working correlation linking the calculated E-field enhancements on specific nanostars to the SERS signal enhancement they produce.

Our approach to the problem has been to initially coat the nanostar with a thick silica layer and then etch it gradually away, thus enabling thiolated analytes to bind preferentially to the exposed gold surface. In this study however, we have chosen to use a Raman reporter molecule (ATP) capable of binding also to silica, so as to be able to measure SERS signal enhancements for the fully capped nanostars as well. Although we acknowledge that this may not be a fully comprehensive solution, it is a first step to correlating model and experiment even when a complete nanoparticle characterization is not available or not possible. In the parts, we will compare side by side the experimental and computational results in order to provide a comprehensive description of our strategy. More details on the synthetic method can be found in our relevant published work.[53]

Assimilating asymmetries and resulting peak broadenings

Surfactant free gold nanostars were synthesized as reported in our relevant work[53] resulting in two most common morphologies: an asymmetric and an asymmetric branched (see **Figure 8**). Both nanostructures are expected to provide intense field enhancements, but their optical properties and field localizations differ due to these variations in morphology (vide infra). In **Figure 8**, the experimental optical spectra collected for the asymmetric and asymmetric branched nanoparticles are reported. As can be observed a blue shift of 16 nm (from 851 nm to 835 nm) of the LSPR occurs when going from the *asymmetric* to the *asymmetric branched* morphology. Moreover, a broadening of the LSPR band can be observed and correlated to the presence of the small side branches. For these data the absolute intensities cannot be correlated, as the samples were obtained from different syntheses.

In the computed heat losses spectra reported in **Figure 9** it is possible to pinpoint a distinct broadening of the spectrum in the case of nanostars with asymmetric morphology compared to the symmetric counterpart that further increases when branched spikes are simulated. The resonance peak is also blue-shifted, which is in agreement with the experimental results reported in Figure 2. What can be observed in the simulation is that the intensity of the blue-shifted peak is also higher than that of its non-branched counterpart. This result can be explained by considering that in both asymmetric cases (branched and not) the overall LSPR band becomes more heavily weighted by losses due to smaller features, which are known to absorb at higher energies,[72] and by an overall increase in volume, which is included in the calculation of the heat losses. Moreover, when comparing the symmetric case (blue) to the asymmetric one (red), one can observe, for the latter, a

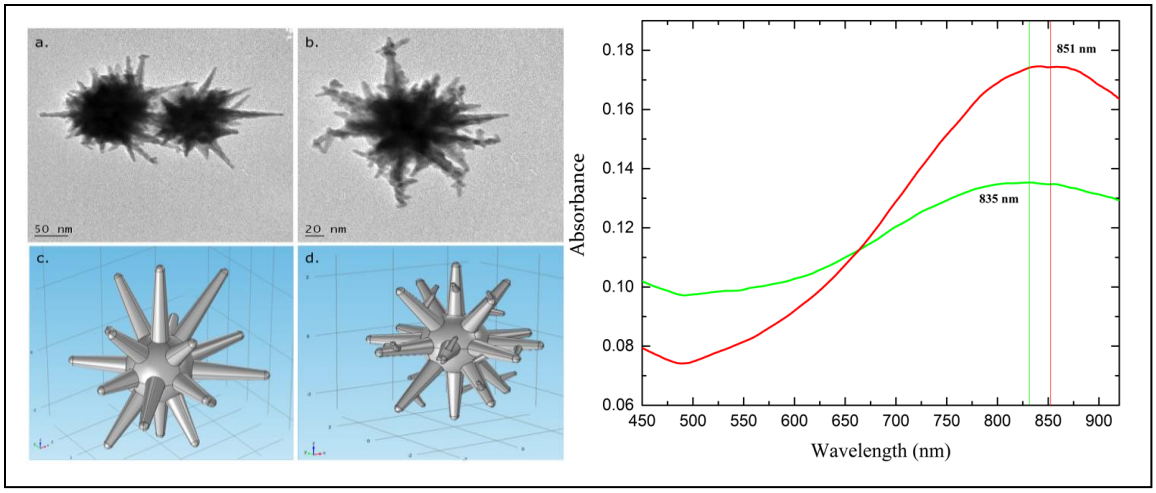

Figure 8. *(Left)* The morphology of gold nanostars can be extremely varied. TEM micrographs (a and b) of gold nanostars synthesized employing the same seed-mediated, surfactant-free, *bottom-up* protocol highlight that the morphology of the nanostars can go from asymmetric with sharp, non-branched spikes (a) to asymmetric highly-branched spikes (b). In order to simulate correctly the field enhancements in these nanostructures we have employed 3D geometrical topography models as close as possible to the non-branched (c) and branched (d) morphologies encountered in the synthesized nanoparticles. Number of spikes for the two 3D models n=18. *(Right)* UV-Vis experimental results show a red shift and broadening of the LSPR going from the asymmetric (red) to the asymmetric branched (green) nanostar morphology.

tail at 700 nm due to the contribution of the longer spikes and a blueshift of the maximum from 655 nm to 645 nm, as a consequence of the presence of the highly-absorbing short spikes, whose absorption convolutes with that of the average-length ones. The effect is even higher for the asymmetric branched case (green), in which the presence of 18 extra lateral branches with lengths between 3 and 6 nm shifts even more the absorption to the blue increasing its overall intensity when compared to the asymmetric case, as longer and pointier spikes are known to cause redshifts as it has

been extensively discussed in chapter I. It should be noted that a direct comparison between experimental and computational results is not possible for the *symmetric* nanostar morphology, as this nanoparticle cannot be obtained synthetically. Moreover, as heat losses and absorption spectra do not represent the same physical

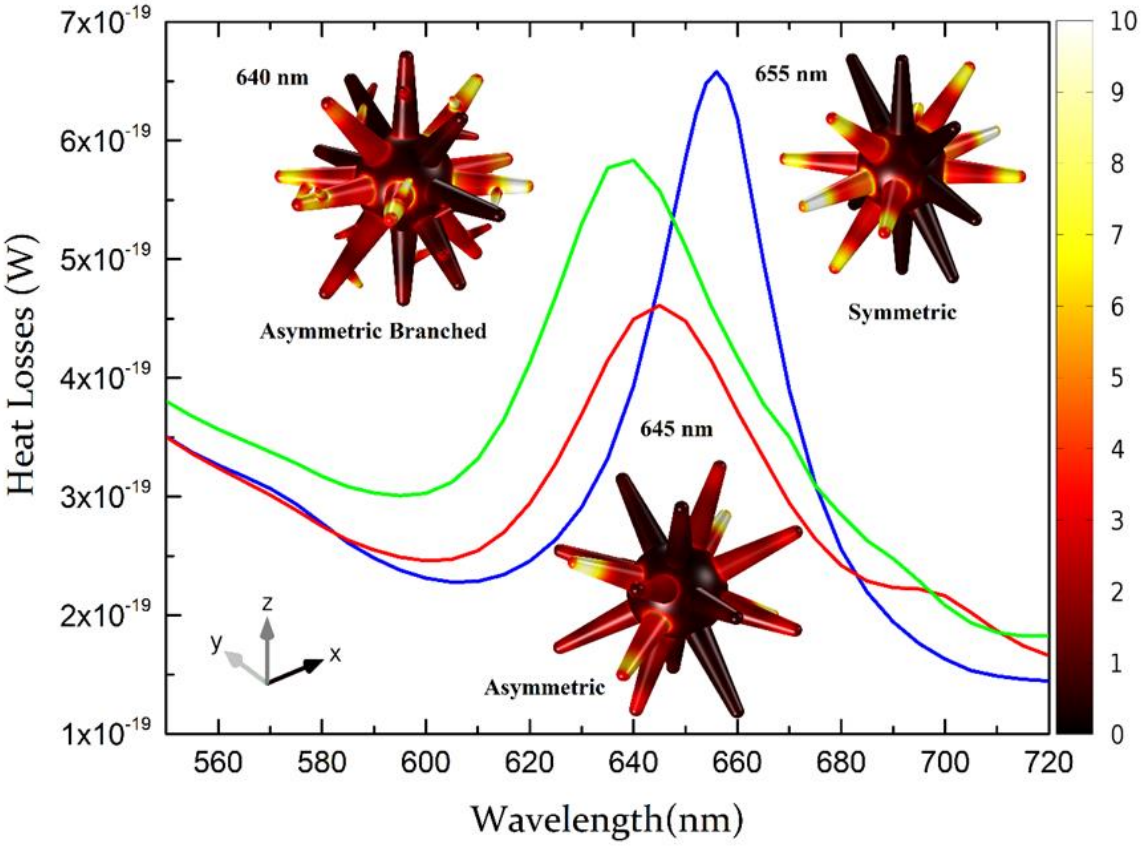

Figure 9. Heat losses and on resonance normalized electric field distributions for a symmetric (blue), an asymmetric (red), and an asymmetric branched (green) gold nanostar. From both spectra and E-field distributions it is possible to observe that the increase in asymmetry for the non-branched morphology (blue to green) leads to less intense LSPR bands, with the same locations on the nanostar providing reduced E-field enhancement. In addition, the increasing asymmetry factor leads to LSPRs that are blue-shifted, as a consequence of a weighted contribution to the losses from progressively smaller features, which absorb more at shorter wavelengths.

phenomenon, we compare only the spectral positions and shifts. Heat losses represent the power losses in Watts (W) taking place in a particle with a specific shape and size. The intensity of the heat losses spectra cannot be accounted in the comparison with the absorption spectra, instead can be utilized in the comparison with the Raman enhancement factor, as we will present in the next subchapter.

In the insets of Figure 9, one can observe how the enhanced field in these nanostars is not located *exactly* at the tip of the spikes. This effect is due to two factors, 1) the spike length of the model nanostar and 2) the radius of curvature of the tip, based to what we have extensively discussed in chapter I. In all cases, the modes assignable to the spherical core do not appear to contribute significantly to these resonances. They do, however, contribute heavily to the resonant mode at 500 nm. This mode appears significantly attenuated, if not disappeared, due to the extent of the coverage of the spherical part of the nanostar from the bases of the spikes.

Gold Nanostars with Selective Silica Coating.

Silica coating was carried out using a modified Stöber method. Partially etched nanostars were obtained as we described in the relevant published manuscript.[53] TEM micrographs of nanostars with partially and fully etched silica shells are reported in Figure 12 in comparison to modelling studies of the same system.

UV-Vis spectra of the bare and silica-coated stars were collected to provide evidence of 1) effective capping, 2) morphology retention, and 3) stability, and to establish a point of reference for the E-field simulations. In **Figure 10** the

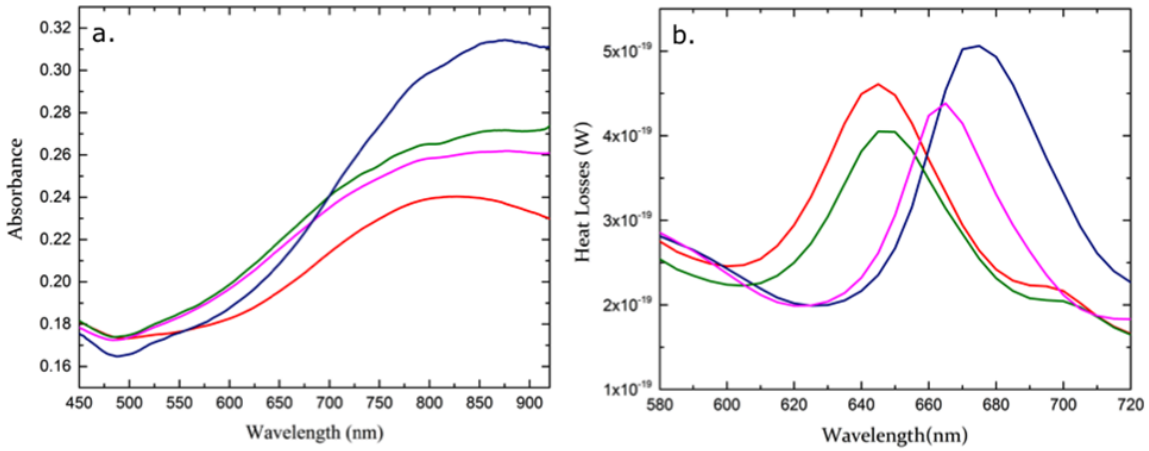

Figure 10. Experimental extinction spectra (a) can be explained using heat losses calculated from the simulation (b). In the simulation for asymmetric bare nanostars (red), asymmetric etched nanostars with 12.2 nm effective silica radius (green), asymmetric etched nanostars with 23.2 nm effective silica radius (magenta), and asymmetric coated nanostars with a 29 nm effective silica radius (blue), the intensity for the heat losses are higher in the presence of a full silica coating compared to the cases of bare and partially capped nanoparticles.

experimental results (Figure 10 a) have been compared to the heat loss spectra obtained computationally (Figure 10 b). As expected, the resonance is red shifted in the presence of a partially etched silica coating (blue, coated tips, no silica overgrowth) compared to the other three cases, as a consequence of the variation of the dielectric constant of the medium surrounding the nanoparticle (from 1.77 to 2.09). The red-shift is more pronounced for nanostars with a higher effective radius of silica, i.e. those presenting a silica overgrowth, with double exponential dependence of the red-shift vs. the effective radius, as reported in **Figure S6**. The overall intensity decreases with the decrease in the amount of silica present, and the position of the LSPR is almost entirely regained in nanostars with close-to-fully etched silica coating (green). As seen

before, the shoulder at ca. 695 nm is attributed to local morphology anisotropies in the individual nanostars. The intensities of the LSPR for the blue curves are higher than those for the red curves, as reported experimentally by Liz Marzan and coworkers for the case of gold nanospheres.[73]

Evaluation of SERS Signal Enhancements

As a consequence of the results reported above, in which both the intensity and position of the scattered electric field depend on the degree of SiO_2 coating, it is expected for the experimental SERS signals to be enhanced with respect to the corresponding Raman counterparts with a dependence from the electric field that varies with the morphology of the nanostructure and its effective silica coating layer, which not only changes locally the dielectric constant, but selectively exposes the tips. As the SERS signal enhancement depends quadratically on the impinging radiation as described in Equation 3, and considering that this second order dependence is the same extracted for the heat losses spectra (see Appendix 1 Equations S16 through S18), we expected to observe significant similarities between the experimental I_{SERS}/I_{Raman} ratios and the heat losses maxima trends, when displayed with respect to the effective silica *radii*.

In order to verify this hypothesis, we ran SERS experiments on surfactant free nanostars, fully coated silica nanostars with an effective silica radius of (54.2 ± 11.8) nm, and partially etched nanostars with effective silica radii of (12.9 ± 3.0) nm, (20.8 ± 7.2) nm, (26.9 ± 4.1) nm, and (40.0 ± 9.8) nm. The Raman reporter chosen was aminothiophenol (ATP), due to its ability to bind to both gold and silica, the former via the formation of Au-S bonds, and the latter through strong hydrogen bonds

between the pendant amino moiety and the silanol groups on the surface of the silica shell.[74] The intensity of the peak at 1080 cm^{-1} (C-C + C-S stretching[75]) was chosen to calculate signal enhancements for all cases (I_{SERS}/I_{Raman}). The experimental SERS spectra, collected for an ATP concentration of 1 μM, can be observed in **Figure 11**.

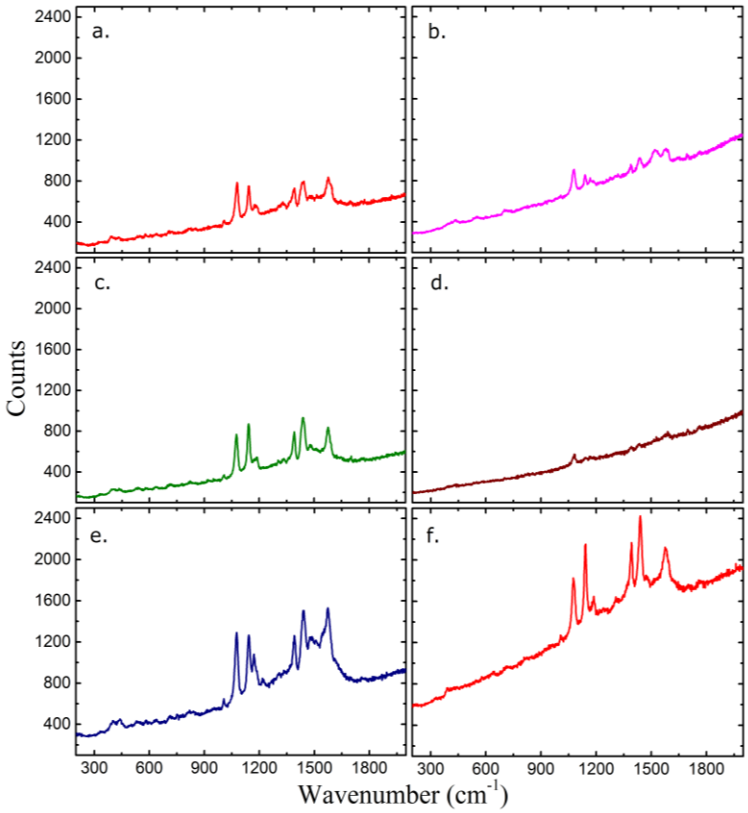

Figure 11. SERS spectra of aminothiophenol (ATP) on surfactant-free nanostars (a), partially silica coated nanostars (12.9 nm (b), 20.8 nm (c), 26.9 nm (d), 40.0 nm (e)), and fully coated nanostars (54.2 nm (f)). Acquisition parameters: 633 nm laser excitation wavelength, 1% laser power, 1 s acquisition time, one accumulation.

Comparing SERS enhancement to power losses

In **Figure 12** we report the computational simulation results describing the E-field localization on nanostars with a variable degree of SiO_2 coating. The 3D E-field

maps were calculated for six effective silica *radii* (i.e. from the surface of the nanostar to the silica-air interface) which represent variable degrees of silica coating. As previously observed, the most intense E-field for nanostars that are not fully coated by silica is not located exactly at the tips, but slightly away from it. On the other hand, in the presence of a homogeneous silica coating, both the position and intensity of the most enhanced E-field change; the intensity increases, and its position is shifted to the tip of the spike.

The I_{SERS}/I_{Raman} ratios vs. the effective silica *radii* trend obtained from the experimental results of Figure 11 are plotted in **Figure 12**, along with the variation of the heat losses maxima vs. the effective silica *radii*. It should be noted here that the two trends are reported in the same graph to highlight their similarities, but no physical meaning should be attributed to the scaling factor used to normalize the x-axes. In both cases, a minimum in enhancement is achieved when a silica layer coats only partially the spikes, while the enhancement is maximum when silica covers completely the nanostars. The maximized enhancement observed for fully coated nanostars can be explained as follows. Because NH_2 groups can bind to silica, albeit less tightly than thiols would do to gold, and because the thickness of the SiO_2 overgrowth is maintained at a minimum, ATP can still experience the enhanced scattered E-field generated by the nanostar. Because the dielectric constant of silica is larger than that of air, the enhanced near field is not only red-shifted but also more intense than that measured in the absence of the silica shell. As a consequence, the SERS signals of ATP measured on the fully coated particles will be larger than those obtained with only partial capping. The partial disagreement between experimental and computational results observed for naked nanostructures (i.e. SiO_2 thickness of 0

nm) might be due to a possible preferential binding of ATP to selective facets on the tips, thus not enabling us to fully probe the enhanced field generated by the nanostars in the experiments as compared to the simulated results. Overall however, there is a very strong correlation between the two trends, indicating that our model could be used to accurately predict the effectiveness of a nanostar of specific morphology at enhancing SERS signals, and hence to potentially improve our ability to preemptively

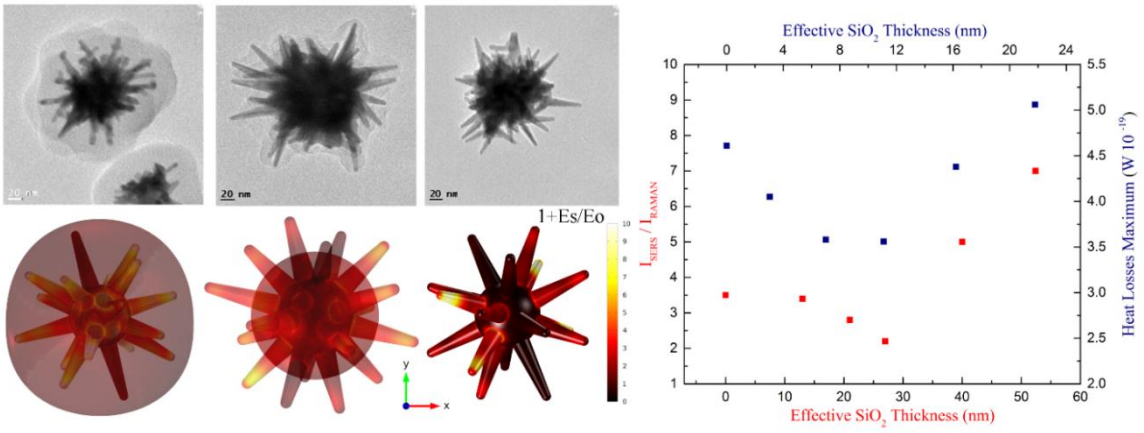

Figure 12. *(Left)* TEM micrographs of regressing degree of SiO_2 coverage in comparison to finite element simulations of the electric field norm of models built in accordance to the synthesized nanostars. SiO_2 coating etched at varying degrees (effective radii 12.2 and 23.2 nm respectively) and of fully capped gold nanostar (effective radius 29 nm), all in water. (Right) Comparison between experimental I_{SERS}/I_{Raman} ratios (red) and computationally calculated heat losses maxima (blue) vs. Effective silica layer thickness trends. Both values depend on $|E|^2$ and their agreement is an indication of the validity of our approach. For the sample with no silica coating (i.e. naked nanostars) the partial disagreement may be due to selective ATP binding to preferential facets of the nanostar spikes that would thus reduce the intensity of the effective scattered field experienced by the molecule compared to what predicted by the simulation.

rule out some nanoparticle morphologies and prioritize others, thus speeding up their use in applied SERS studies.

Chapter II Conclusions

Gold nanostars have demonstrated to be excellent SERS platforms and have been widely used in SERS-based imaging and sensing applications. However, fundamentally understanding how their morphology can impact their effectiveness as field enhancers is a complex task. In this chapter we have sought to understand how nanostar morphology can affect localization and intensity of the scattered electric fields and how these can in turn be linked to the measured SERS signal enhancements. By synthesizing silica-coated nanostars and selectively etching the silica layer away so as to expose increasing amounts of the tips, and by using these particles in model experiments where the Raman signal of aminothiophenol was enhanced in the presence of the nanostars, we were able to determine a strong correlation between the intensity of the nanostar morphology and its silica coating layer, the enhanced electric field, and the SERS signal enhancements. We believe that this model represents a very useful working platform to predict which factors mostly affect the effectiveness of nanostars as SERS substrates.

We do recognize that these particles may be morphologically too complex to achieve an *exact* correspondence between model and experiment; steps into this direction have been taken in the next two chapters.

Chapter III: Zooming in on the Properties of a Real Particle

As we have already mentioned gold nanostars systems suffer from a series of inconsistencies regarding their fundamental physical and optical parameters. In detail, parameters that describe Au nanostars, such as volume, surface area, and extinction coefficient, have not yet been evaluated for all types of nanostar systems. Recently, Hamad-Schifferli and coworkers have estimated, for the first time, the extinction coefficient of nanostars synthesized via HEPES-based seedless protocols;[71] this value is extremely important to estimate the concentration of NSs in suspension and to enable their quantitative application. However, surfactant-free Au nanostars and HEPES-capped ones drastically differ in morphology, thus granting a closer look at nanostars synthesized with seed-mediated approaches.

Recently, our group has demonstrated how Au NSs can be grown via seed-mediated bottom up protocols to possess extremely sharp spikes if ascorbic acid (AA) is employed both as the reducing and the capping agent.[2] The morphology of AA-capped nanostars can be tuned primarily by varying the concentration of gold seeds and $AgNO_3$, leading to multiply-spiked NSs, in which the spikes can further branch out in a characteristic snowflake-like geometry, if aging is conducted in particular experimental conditions or the order of addition of the reagents is modified. The AA ligands can be easily replaced by silanols to grow uniform silica shells that can be then etched with $NaBH_4$ to expose only the tips and lead to NSs with further increased enhancement factors as extensively presented in the previous chapter.[53] However a better understanding of NS morphology is still needed and would dramatically

improve the applicability of these nanoparticles in catalysis, sensing, and plasmonics. For example, the ability to pragmatically correlate the synthetic parameters to the number and length of the tips produced, the overall surface area, and the nanoparticle volume, would give us the opportunity to quantitatively calculate their optical properties, which have until now only been estimated, often in extremely conservative terms.

In this chapter, we have initiated a two-pronged study in which simulations and experiments have been employed jointly to predict and confirm the fundamental physical and optical properties of gold nanostars synthesized following seed-mediated bottom up protocols. Namely, we have determined the volume, surface area, and extinction coefficient by first developing a semi-empirical method in which their values were estimated.

We have then carried out high-resolution (HR) TEM experiments, inclusive of STEM tomography, to confirm them and determine whether our proposed simplified approach could be employed to rapidly estimate these parameters and generalized to calculate them for nanostars of varying dimensions. Finally, we have exported the 3D reconstructed NS topography into the software Comsol Multiphysics, to reconstruct the octahedral elements needed to build the NS finite element geometry, calculate intensity and distribution of local scattered electric fields, and determine the particle's morphology-dependent extinction coefficient.

A Real and Realistic Approach

Our results provide, for the first time, a computational model describing scattered electric fields in real Au nanostars. Importantly, our work provides a practical method that can be used to easily estimate the fundamental physical and

optical parameters of nanostars of any given diameter, spike length and density, and material composition. Although herein we do not discuss explicitly mode assignments on the optical parameters as we did in chapter I, these considerations are closely taken into account in the fundamental physics built within the 3-dimensional approach we use to solve Laplace's homogeneous equation in the non-symmetric nanostar geometry. With this work, our overarching goal was to provide a simplified yet accurate and reliable method that could be used by any scientist needing to confidently employ these particles in applications.

We have synthesized AA-capped AuNSs *via* a bottom up seed-mediated approach in which spherical nanoparticles are employed to seed the growth of variably sharp spikes. The HR-TEM micrograph in **Figure 13** (left panel) shows the morphology of a typical 12 nm citrate-capped seed. A face centered cubic crystal structure (FCC),

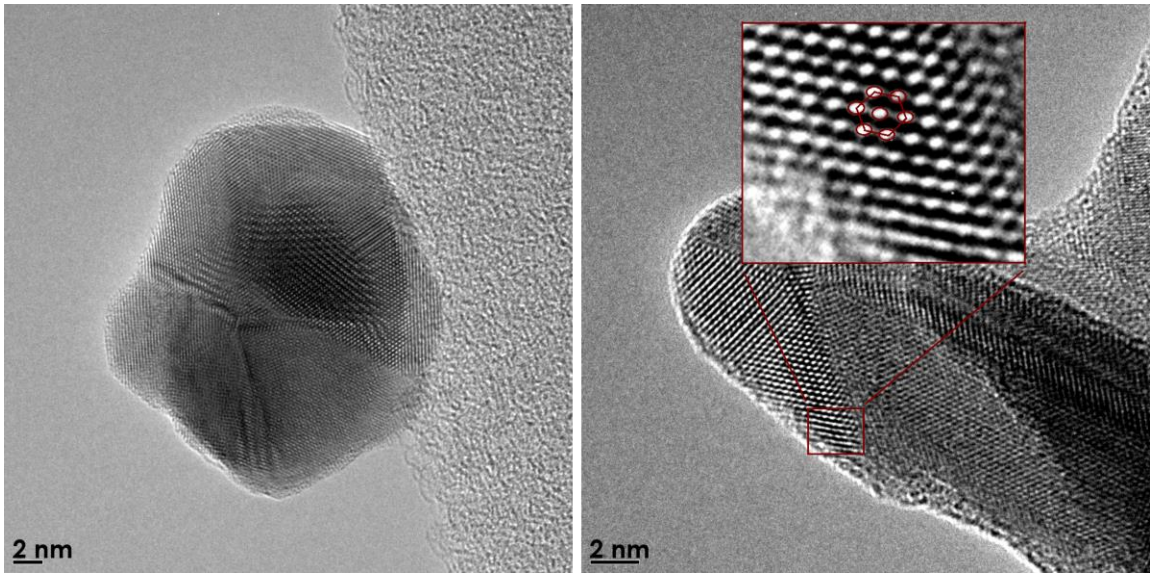

Figure 13. HRTEM micrographs of a gold nanostar seed with 12 nm diameter (left) and of the tip of a nanostar spike (right). Both scale bars are 2 nm. Atomic arrangement in agreement with a FCC crystallographic structure is highlighted on the nanostar spike.

commonly observed in spherical gold nanoparticles within this size regime, characterizes these seeds. A typical FCC atomic packing can be also observed for the AA-capped NS spike (right panel), thus we can confidently assume a density of 59 atoms/nm^3 for the overall NS.[76] We observe the crystal planes in both structures and we recognize five – fold twinning in both the seed and the nanostar spike. Five – fold twinning is quite common in gold nanoparticle synthesis in general as reported by Grzelczak *et al.*[77] The growth of NS spikes is related to and affected by twinning.[78] In the inset of Figure 1 we present a further magnified HR-TEM micrograph where we can recognize the FCC crystal structure as captured on a (100) plane. As [111] planes are known to be the crystal facets of lowest energy in FCC gold nanoparticles,[76] we can expect that these [100] planes are not the result of a thermodynamic-driven reaction, but may be due to kinetic traps occurring during the NS growth. Both [111] and [100] planes are dominating in the spherical Au nanoparticle size regime around 12 nm, while other crystallographic facets appear for larger spherical particles or when the symmetry is broken, as demonstrated experimentally[79] and calculated via Wulff construction.[80-81]

A Semi-Empirical View

Dimensional analysis of the NSs was performed using the ImageJ software, including the spherical core size, the tip base *radius*, the tip's hemispherical cap *radius*, and the distance between the two *radii* (i.e. base and cap), for all spikes that appeared normal to the beam. Tips that were observed but not measurable were accounted for, and their number assumed to be equal by symmetry on the side of the NSs opposite to our viewpoint. Based on the calculated averages and standard

deviations of spike volumes and the volumes of spherical caps formed by the intersection of the spikes with the spherical core, the volumes for the unmeasured spikes were simulated assuming a normal distribution of dimensions. After statistical analysis (see ESI), we modeled our nanostars as possessing 18 spikes with normally distributed lengths, even though we realize that this does indeed represent only a simplified model.

The average AA-capped NS volume was calculated according to **Equation S3** (Appendix I) to be 4.141×10^{4} nm^3, leading to approximately 2.443×10^{6} atoms per NS on average. The exact nanostar concentration was determined taking into account ICP-MS experimental results, in which the concentration of gold in the NS suspension was calculated to be 23.54 mg/mL, leading to a NS yield of 74% for this synthetic protocol, in line with values reported by Hamad-Schifferli and Murphy.[71, 82] Based on these values, the molar concentration of Au NSs was estimated to be $[(5.355\times10^{-3}\ M/ 2.443\times10^{6}\ NS^{-1})\times0.74] = 1.622$ nM. The average nanostar surface area was calculated as according to **Equation S4** to be 4.772×10^{3} nm^2.

Starting from the calculated concentration value and the absorbance of the plasmon peak using Beer-Lambert's Law from **Equation S19**, the extinction coefficient was estimated to be $3.14\times10^{9}\ M^{-1}cm^{-1}$, in agreement with the values reported in the literature.[71] A per-atom estimation of the NS extinction coefficient results in a value of $9.77\times10^{9}\ M^{-1}cm^{-1}$, where the extinction coefficient of a single gold atom is equal to 4000 $M^{-1}cm^{-1}$, as shown by Link *et al.*[83] This differs from the value determined using our semi empirical method and the Beer Lambert's law by a factor of 3.11, which could be due to an overestimation of the number of spikes or to our assumption of a normal spike-length distribution. Nonetheless, the close proximity of the two values leads us

to consider the semi-empirical model we developed a valid approach to calculate extinction coefficient, volume, and surface area of gold nanostars synthesized from seed mediated bottom up protocols starting from the basic NS dimensions determined from TEM analyses.

A Modern FEM-Powered 3D Perspective

To complement and further validate these experimental results, we have employed the software Comsol Multiphysics to calculate the physical and optical properties of our NSs. Whereas we usually employ finite element simulations to exclusively study the optical properties of the nanomaterials we synthesize,[48, 53] in this work we exploited them from an additional standpoint, i.e. to also calculate the total volume and surface area of the NSs and corroborate our proposed simplified approach. By collecting electron micrographs at high tilt (+70°/-70°) (**Figure 14**) and reconstructing the 3D topography of the nanostar (**Figure 15**), we have introduced, after a size adjustment to exactly match the dimensions of the real and simulated particles (**Figure S7**), the 22,000 topographical tetrahedra contained in the tomography into Comsol's RF module, employing Rhinoceros (Rhino3d) software to convert the Virtual Reality Modeling (VRML) topography to a Stereolithography (STL) topography. Through this approach, we have estimated the volume of the 3D reconstructed nanostar to be 5.551×10^4 nm^3, with a surface area of 1.345×10^4 nm^2. The volume calculated is impressively similar to that estimated according to Equation S3 (4.141×10^4 nm^3), while the surface area is roughly 2.5 times larger than the 5.055×10^3 nm^2 calculated with Equation S4, consistent with the fact that the semi-

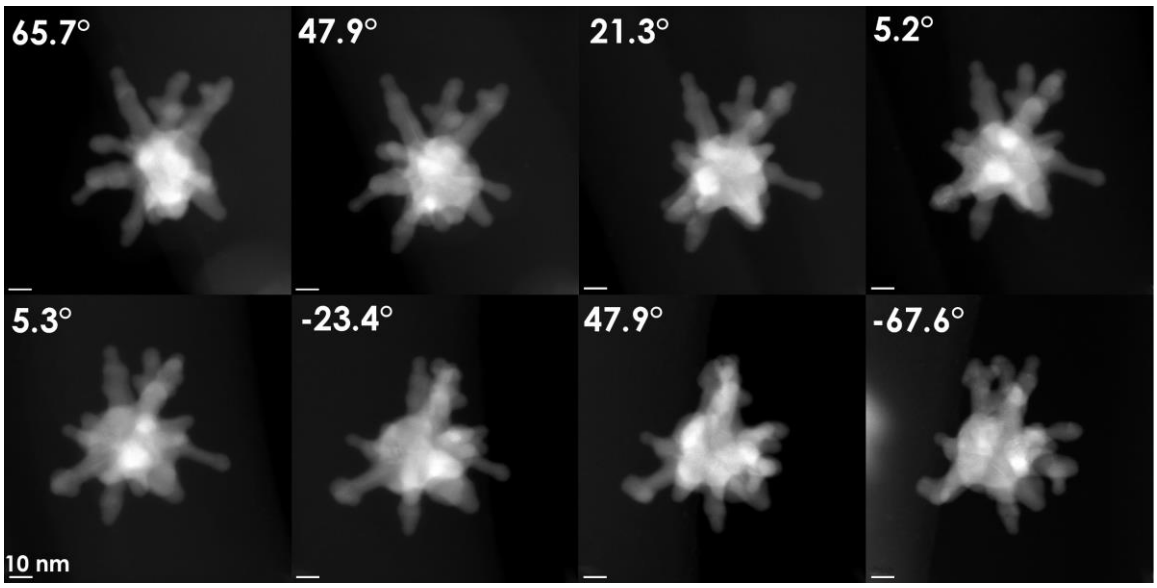

Figure 14. Tilted STEM micrographs of a gold nanostar. Note the crystallographic details that appear at each orientation.

empirical model does not take into account the local roughness at the surface of the NSs, which can instead be picked up by the tomographic analysis. Based on these numbers, a per-atom calculation of the extinction coefficient led to a value similar to that reported above (1.31×10^{10} $M^{-1}cm^{-1}$), slightly higher than what calculated by

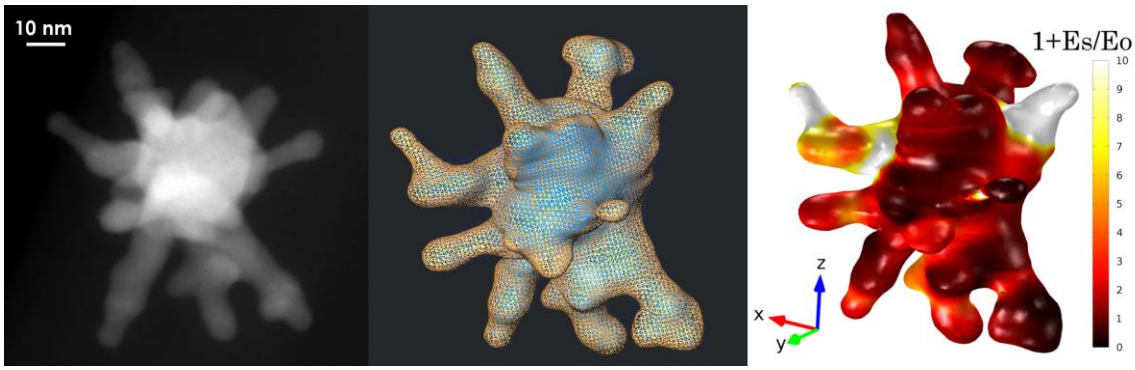

Figure 15. 3D tomogram (left), nanostar topography reconstructed employing 22,000 tetrahedral elements (center), and scattered electric field distribution (right) calculated using Comsol Multiphysics starting from the finite elements extracted from the tomogram.

Hamad-Schifferli and coworkers.[71] These results are consistent with the fact that our NSs are, on average, larger than those analyzed by Hamad-Schifferli and her group (71 nm vs. 22-55 nm spike length), and are thus characterized by higher per-particle extinction coefficients. Compared to values that have been reported in the literature for gold nanospheres of similar volume (e.g. 2.93×10^{9} $M^{-1}cm^{-1}$ for nanospheres with volume of 70,000 nm^3), the values we calculated for nanostars employing the 3D reconstructed model are ca. 4.5 times higher than those of nanospheres with 1.3 times larger volumes.[21] Thus, when normalizing for nanoparticle volumes, we obtain a value for the extinction coefficient of nanostars that is 5.9 times larger than that of nanospheres, thus confirming the superior performance of nanostars in their interaction with light.

Morphology-Dependent Extinction Coefficient

We also determined the morphology-dependent extinction coefficient of the 3D reconstructed nanostar according to **Equation S11.** We first calculated the extinction cross section for 8 different orientations at 720 nm and then determined its weighted average according to **Figure 16**, leading to a value of $\sigma_{ext} = 5.268 \times10^{-15}$ m^2. Assuming again 59 atoms/ nm^3 with a 5.551×10^{4} nm^3 volume per nanostar we obtained 3.275×10^{6} atoms per nanostar. Having estimated (via ICP-MS) the total concentration of gold to be 3.9627×10^{-3} M, and having determined the nanostar volume via tomographic reconstruction, we could determine the final concentration of nanostars to be 1.210 nM. The number density of nanostars was found as $C\times N_A = 1.210$ nM $\times$ 6.02214×10^{23} $= 7.287 \times10^{14}$ NS / L or 7.287×10^{17} NS / m^3. According to **Equation S11** the

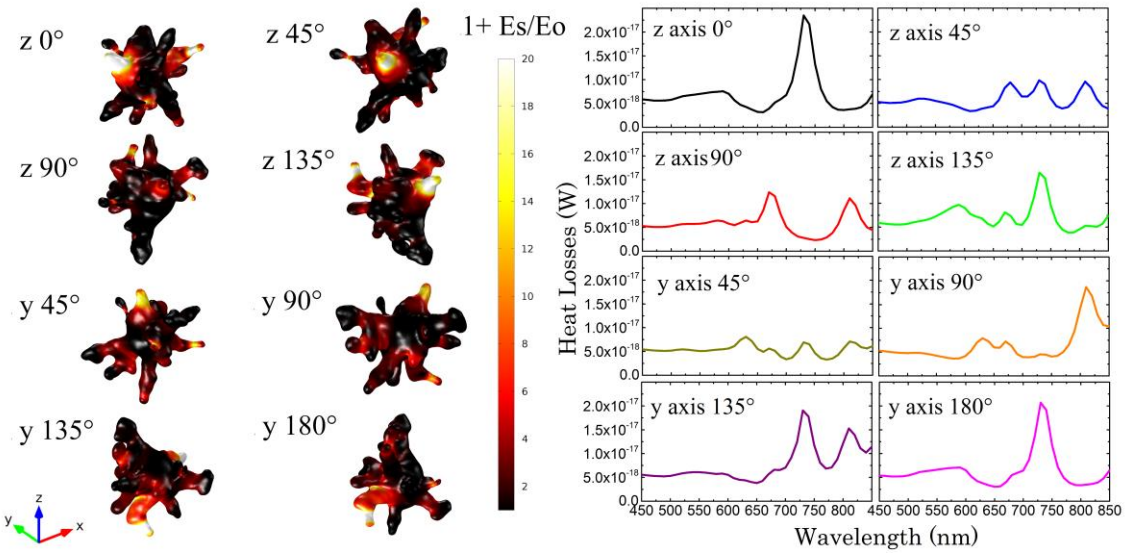

Figure 16. Electric field plasmonic enhancement maps of the 3D reconstructed nanostar under 8 different orientations along with their respective heat losses spectra.

concentration dependent extinction coefficient was found to be ε_{dep} = (5.268 ×10^{-15} m^2) × (7.287 ×10^{17} m^{-3}) = 3.839 ×10^3 m^{-1}. Finally, the concentration independent extinction coefficient was calculated as $\varepsilon = \varepsilon_{dep} / C$ = (3.839 ×10^3 m^{-1}) / (1.210 nM) = 3.173 ×10^{12} M^{-1} m^{-1} or ε= 3.173 ×10^{10} M^{-1} cm^{-1}. This morphology-dependent extinction coefficient value, significantly larger than those determined with the other methods, stresses the importance of taking into account the role of morphology in particles such as nanostars.

The Optical Behavior of a Real Nanostar

To correlate not only the intensity but also the spectral features of the calculated and experimental data, we have then calculated the scattered E-field maps and the associated heat losses and, following the approach we have previously

reported in chapters I and II, compared the heat losses spectra to the experimental UV-Vis-NIR absorption spectra. We have calculated the heat losses spectra of the 3D reconstructed nanostar under eight different orientations, when keeping the x-axis as the polarization axis of the incident electric field. By assuming every orientation as equally probable, we double the probability of the 0° orientation, as the 180° orientation gives the exact same spectrum. This case is not applied for the 45° and 135° cases, as seen in **Figure 16**, as the NS does not possess a C_4 axis of symmetry. Each individual orientation appears to excite different plasmonic modes on the spikes, as observed in Figure 16. Interestingly, only select spikes localize a *hot spot* at each orientation, with some spikes localizing the highest enhanced scattered fields at slightly offset positions with respect to the tip of the spikes, as we observed in Chapter II. Symmetric nanostructures have been reported to exhibit multiple resonant modes of different order, studied as extension to the dipolar image of plasmon resonances.[84] In the case of this highly asymmetric nanostars, it is noteworthy how plasmonic modes of different order, contributing to the resonances seen in the spectra, can still be observed. Several dominant resonances can be identified in the simulated spectra, at 675 nm, 720 nm, and 800 nm, which can be assigned to dipolar (720 nm and 800 nm) and multipolar (675 nm) plasmon modes of the spikes. The broad resonance around 550 nm is attributed to the spherical "bumps" on the nanostar body (most likely non-fully grown or reconstructed spikes). As opposed to other computational studies carried out by us and others, in this simulation it is difficult to assign a mode to the spherical core, as it is not possible to determine whether or not it has remained intact during the growth of the spikes, even though it most likely does contribute in part to this resonant band.

We have then considered a weighted average of all the heat losses spectra in an attempt to reproduce the peak broadening observed in UV-Vis-NIR ensemble-averaged measurements, as presented in **Figure 17**. In addition to the broadening due to tumbling of the nanoparticles in solution, we need to take into account the morphological differences intrinsic to the sample, as AA-capped NSs are known to be very inhomogeneous, as observed in **Figure S8**. Small differences in the shape, length, and orientation of the spikes result in large differences in the absorption profiles, as seen in **Figure 16**. Thus, even in the case of a very uniform batch of NSs with multiple spikes, small differences result in large peak broadenings. Nonetheless, despite the fact that we are herein comparing an individual nanostar modeled under eight different orientations to thousands of nanostars of significantly different shape under many possible orientations, the comparison provides an excellent insight into the nature of the plasmonic resonances of nanostars. By carrying out additional TEM tomography experiments over a larger number of nanostars per sample and reconstructing the heat losses spectra at different orientation with respect to the incoming light, as demonstrated herein, one could take further into account the shape effects on the peak broadening and build an even more detailed model. Our purpose here was, however, to demonstrate the applicability and reliability of the method and identify ways in which it could be used for nanostars of different overall diameter, spike size and density, and nature of the metal.

The UV-Vis-NIR spectrum of the nanostar suspension (**Figure 17 and S10**) exhibited a plasmon resonance peak centered at 778 nm at the time of the synthesis. At the time of the microscopy studies we repeated the measurement noticing a blue-shift of the plasmon resonance peak to 672 nm, due to a dynamic shrinkage of the NS

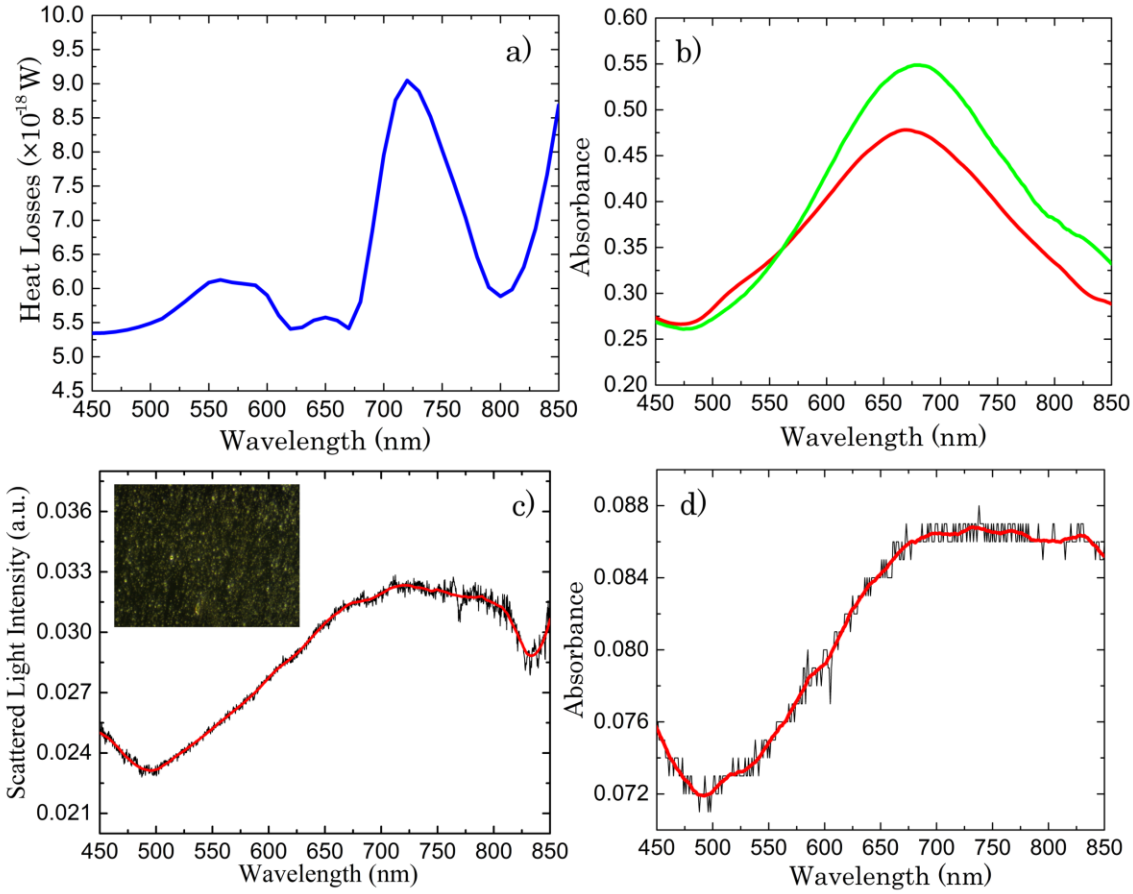

Figure 17. Computational simulation and experimental characterization of the optical properties of the nanostars studied. Weighted average of the heat losses spectra of the 3D reconstructed nanostar (a), UV-Vis-NIR spectrum of aqueous nanostar suspensions when TEM tomograms were collected (b, red line), and when dark field spectra were recorded (b, green line). Dark field scattered light spectrum (black line scattered light intensity signal and red line mean average) (c), UV-Vis-NIR spectrum of nanostars deposited on a microscope slide (black line signal and red line mean average) (d).

spikes, as reviewed by Jiang and coworkers.[85] Based on an additional UV-Vis-NIR spectrum taken 18 months after the synthesis, which exhibits a maximum at 676 nm,

we can confidently state that the nanostars studied possess the final, kinetically-trapped morphology and that their properties can be analyzed side-by-side.

In **Figure 17** (a) we compare the weighted average of the heat losses spectra of the 3D reconstructed nanostar presented in **Figure 16**, along with the UV-Vis-NIR spectra of aqueous nanostar suspensions (b), a dark field scattered light spectrum (c), and the UV-Vis-NIR spectrum of nanostars deposited on a microscope slide (d). In general we see good agreement among the experimental spectra collected for dried nanostars ((c) and (d)), in which the plasmon resonance appears redshifted compared to what observed in suspension. This fact is consistent with the higher dielectric function for glass, onto which the nanostars are deposited, compared to water and air. By comparing the experimental data with the heat losses spectra of nanostars in water we can observe how the latter display a much narrower plasmon band which is centered at 715 nm. While we can confidently justify the broadening as due to the heterogeneous nanostar morphology and their brownian motions in suspension, the discrepancy concerning the peak position deserves more insight. Overall, we believe this to be due to the fact that our 3D reconstruction has only focused on one nanostar, which is not representative of the entire sample; for instance, by examining a larger sample composed of nanostars with more numerous, shorter spikes, we would have observed a substantial blue shift of the plasmon resonance peak, as our model showed in Chapter II.

Nonetheless, despite the mild mismatch between our modeled and experimental data, we can observe an overall agreement in the observed trends, which can justify the use of our proposed, simplified model for the study of morphology and optical properties of gold nanostars synthesized from seed-mediated protocols. In

prospective, one can imagine to be able to use the semi-empirical or tomography-based tools we described herein to study not only nanostars of different morphology and constituting metal, but also, more broadly, nanoparticles of any arbitrary shape and composition, thus further strengthening our understanding of the structure-property relationships of nanoparticles and link them to the various protocols used to synthesize them.

Chapter III Conclusions

In conclusion, in this chapter we developed a semi-empirical, simplified model to calculate the fundamental physical and optical parameters (i.e. volume, surface area, and extinction coefficient) for nanostars grown in solution using seed-mediated protocols. Starting from nanostar dimensions and dominant morphologies determined from TEM and STEM analyses, we calculated quite accurate extinction coefficient values, that we confirmed by comparison with the literature[71] and carrying out combined UV-Vis-NIR and ICP-MS experiments. Based on the close agreement among the various values, we are confident that our approach could be generalized for nanostars of various dimensions synthesized in solution using seed-mediated protocols. In addition, we have further validated our calculations by introducing into Comsol Multiphysics the 22,000 tetrahedra constituting the nanostar's 3D topography reconstructed via STEM tomography, and calculated volume and surface area values, and morphology-dependent extinction coefficient. The remarkable agreement between these and the values determined semi-empirically once more confirms the validity of our simplified model and highlights how NS morphology plays a non-negligible role in enhancing the value of the extinction coefficient, as clearly evidenced by a comparative

Table 1. Fundamental physical and optical properties characterizing gold nanostars as estimated in this work and reported by others.[64]

Approach	Volume [nm^3]	Surface Area [nm^2]	ε [$M^{-1}cm^{-1}$]	$\varepsilon^{b)}$ [$M^{-1}cm^{-1}$]
Semi-empirical Method	4.141×10^4	5.055×10^3	$3.14\times10^{9a)}$	9.77×10^9
STEM Tomography	5.551×10^4	1.345×10^4	3.17×10^{10}	1.31×10^{10}
Literature	1.0×10^3 $3.2\times10^{3\ c)}$	3.0×10^3 1.2×10^4	- -	5.7×10^8 $2.7\times10^{9\ d)}$ 7.8×10^8 $3.5\times10^{9\ e)}$

[a)] Beer-Lambert law; [b)] Per-atom; [c)] AutoCAD reconstruction; [d)] Per-atom; [e)] Discrete Dipole Approximation.

analysis of the values reported in **Table 1**. Overall, we believe that our approach could drastically improve the application of gold nanostars by providing the fundamental parameters necessary to calculate concentration, ligand density, or SERS enhancement factors and thus finally enabling the quantitative application of this remarkable nanomaterial.

Chapter IV: Rational Design of Gold Nanostar Antennas with Tailorable Plasmonic Properties.

In this final chapter we attempt to tackle the recognized intrinsic weaknesses of gold nanostars, as presented in the introduction and the work discussed above. As we have mentioned, these intrinsic weaknesses stem from the insufficient monodispersity currently achievable during synthesis and the discrepancies in plasmonic behavior usually observed between single particle measurements and ensemble studies of coupled colloids. Referring back to the 2007 seminal paper by Hao *et al.*[11], we further investigated, with a holistic computational-experimental approach, the relationship between nanostar structure and relevant plasmonic properties. While various methods for the synthesis of these particles exist, both seeded and non-seed-mediated, either employing surfactants or not,[55, 78] and although substantial improvements have been reported by several protocols,[53, 86] reproducibility and monodispersity have so far not met the necessary quality levels.

Therefore, starting from first principles, we focused here on the simplest type of a nanostar, composed of a spherical core and few, separated, high aspect ratio spikes. The rationale behind the choice of this unique type of nanostar is two-fold: 1) Separated spikes can be hypothesized to only weakly couple, and 2) high aspect ratio spikes should be expected to display multiple narrow harmonics of a fundamental plasmonic mode, as observed in long nanorods and nanowires[31].

In this effort, we approached the study of these nanostars in a deconstructed way, first by computationally building nanostars with increasing numbers of spikes,

and then backing up to a number of spikes that would provide the narrowest plasmon bands with minimized cross-talk. We then optimized a published synthetic protocol to obtain 6-spike gold nanostars with high monodispersity.[87] Utilizing a first-principle method, we carried out an optimization study working in feedback loop between computational predictions and experimental verifications. Herein, we describe how we were able to successfully establish the causal relationship between morphology and plasmonic behavior. Numerically, we demonstrate the presence of an intense fundamental mode in the short-wave infrared (SWIR) regime and its higher harmonics at higher energy. Synthetically, we report on a protocol that displays exceptional monodispersity and reproducibility (for more in depth details on the growth mechanism please refer to [87]). The unbiased agreement between experimental and computational results, both at the single-particle level and in ensemble, proves the validity of our model and confirms the monodispersity of our synthetic approach. We believe that this work can provide a much-needed impulse for the implementation of these nanostars in technologically-relevant applications and possibly for the development of scale-up strategies relevant to industrial-level synthesis.

Gold nanostar resonances extend into the short-wave infrared

By employing 3D finite element simulations *via* the Comsol Multiphysics software (see Supporting Information for details), we have implemented a computational framework to study the plasmonic properties of gold nanostars in which the core and the spikes are considered to resonate as *inseparable* units, thus contributing interactively to the number, position, and intensity of the resulting LSPR modes. Motivated by the need for simple geometries, we focused on gold nanostar

systems formed by few conical spikes, with lengths between 70 and 100 nm, radially grown on spherical cores and decorated by small hemispherical tips. These morphologically simple systems reveal some interesting plasmonic properties, in particular the role of the long spikes on the overall plasmonic response, which can be confirmed experimentally both at the ensemble and single particle level. While reproducing the results initially reported by Nordlander,[11] our study offers interesting new insights. We have observed an intense resonant band at wavelengths longer than 1000 nm, that can be assigned to the first harmonic of the LSPR spike mode. As expected, higher order harmonics (*i.e.* second and third) also appear, that resonate between 600 and 1000 nm, with spacing between the three that depends on the slant length of the conical spikes. Interestingly, our model predicts a linear dependence between the position of the harmonic modes and the spike length, a correlation that we confirmed experimentally *via* Vis-NIR-SWIR spectrophotometry and ATR-FTIR spectroscopy, as seen later on.

These frequency domain numerical simulations also suggest that bulk plasmons might exist in the form of image charges of the interface modes, resonating inside the spikes, owing to their limited thickness. More importantly, we have indications of the presence of propagating polaritons along the spikes that form standing waves and drive the localized resonances, which strongly resonate at the nanostar spike tips. Our modelling results additionally show that the core appears to affect the position of the resonant modes, thus acting as an electron reservoir and interfering with the charge distribution along the spikes. This prediction has been confirmed *via* single particle electron energy loss (EELS) experiments.

Experimental verification

In order to determine the accuracy of the model and corroborate the numerical predictions, we realized that a synthetic protocol was needed that could provide nanostars with 1) a limited number of spikes, 2) tunable spike length, 3) high monodispersity, and 4) consistent batch-to-batch reproducibility. So far, such a detailed synthetic protocol ensuring that all these requirements would be met simultaneously has not been reported. Leveraging and optimizing a synthetic protocol in which the concerted action of Triton X, ascorbic acid, and silver nitrate leads to gold nanostars characterized by LSPR bands that can be tuned through the addition of increasing amounts of $AgNO_3$,[88] we have been able to synthesize highly monodispersed 6-branched gold nanostar samples with enhanced batch-to-batch reproducibility and tunable spike morphology, as reported in[87].

To deepen our understanding of the plasmon resonance-morphology relationship, we synthesized samples with spike lengths of 70 nm, 80 nm, 90 nm, and 100 nm and compared the optical spectra collected spectrophotometrically in ensemble averaged experiments with the results of our calculations (**Figure 18**). We have compared the vis-NIR spectra with the absorption cross section spectra obtained through our model (Figure 18 a-d); in particular, the very good agreement between the position and normalized intensity of the bands modeled and measured (Figure 18e) confirms the validity of our model. The experimental validation, both at the single particle level and in ensemble, suggests that plasmonic resonances in gold nanostars should be interpreted as harmonics of the main LSPR mode. When nanostars with shorter and thicker spikes are studied, the higher harmonics, being less intense and more closely spaced compared to the case of nanostars with high aspect ratio spikes,

seemingly disappear giving rise to the well-known broad LSPR bands observed for

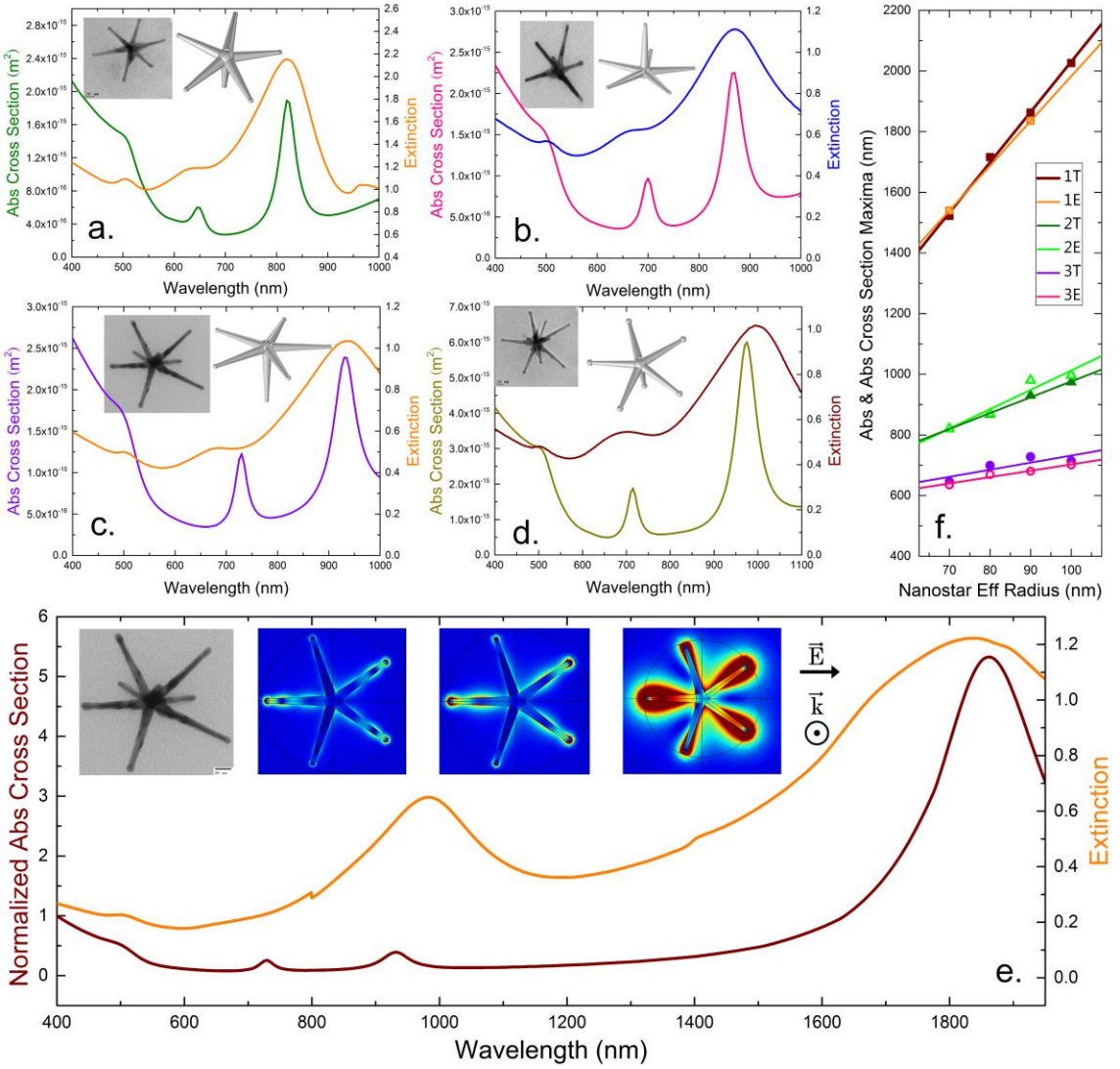

Figure 18. Experimental and theoretical spectra of 6-spike nanostars of a) 70, b) 80, c) 90 and d) 100 nm spike lengths. e) Long range theoretical and experimental spectra of 90 nm radius 6-spike nanostars. E-field norm (calculated *via* Eq. S5 in Methods section in Appendix I) maps of the first, second, and third harmonic modes at 1865 nm, 930 nm, and 730 nm, respectively. Spectra normalization was carried out with respect to the photon energy of each wavelength compared to the photon energy at 400 nm. FWHM for first and second harmonic are 242 nm and 65 nm, respectively, for the calculated spectra, and 500 nm and 190 nm, respectively, for the experimental ones. f) Linear dependence (actual fits) between the harmonic modes resonant maxima (1, 2, and 3) and the nanostar spike lengths. Note the decreasing slope as we move towards higher harmonics and the very good matching between theoretical (T) predictions and experimental (E) results. Details on the normalization of Figure 18e are reported in **Figure S13**.

surfactant free gold nanostars.[21, 89] In reality they become simply enveloped within the more intense fundamental mode. Inter-spike coupling, common in the case of multi-spike nanostars (again observed in surfactant free gold nanostar syntheses) also causes them to slightly blue shift, further broadening the LSPR band. Importantly, disruptions in nanostar morphology lead to substantial modifications in the plasmonic response, as shown in **Figure S14**. Our study, proposing a more generalized approach to the interpretation of LSPR bands in gold nanostars, predicts very well the position of the harmonics based on the detailed morphology of the nanostar in exam. The core diameter, the length, and the sharpness of the spikes, along with the tip morphology (**Figure S15**), dictate the position and distance between the harmonics. The relative position of the bands governs the linear relationship reported in Figure 3f, and follows a simplified rule in agreement with antenna theory (Figure 3f).[29] In the long range 400-1950 nm spectrum in Figure 3e we report both the Vis-NIR-SWIR spectrum and the calculated normalized absorption cross section of a 90 nm nanostar, along with three E-field maps highlighting the spatial distribution of the field at the position of the *maxima* for the three observed harmonics. The very good agreement between position and intensity modeled and experimentally measured provides a solid experimental proof of the validity of our computational approach, which is further supported by the FTIR and EELS results presented onwards. Interestingly, our model suggests that the first harmonic mode, in addition to displaying substantially higher intensity compared to its higher harmonics, appears to extend in space much farther from the surface than the other two, which could be leveraged in techniques such as surface enhanced Raman scattering (SERS) where E-field enhancements lead to higher signal intensity and assay sensitivity.

Ensemble coupling study

In **Figure 19**, we present the ATR-FTIR spectra of highly concentrated aqueous solutions of gold nanostars with spike lengths spanning between 70 nm and 100 nm. The full spectral range, 700-7500cm^{-1}, is reported in **Figure S16**. In the 4000 – 6500 cm^{-1} spectral range, we observe the peak *maxima* for the first harmonic to be centered at ~5700 cm^{-1}, 5180 cm^{-1}, 4930 cm^{-1}, and 4830 cm^{-1} for the 70, 80, 90, and 100 nm respectively. The peak positions of the four different samples fit nicely the E-field norm introduced by the theoretical predictions and the Vis-NIR-SWIR spectroscopy measurements. A noticeable shift in the observed first harmonic peaks can be attributed to interparticle coupling effects (**Figure S17**), since the FTIR measurements took place in concentrated solutions as compared to the Vis-NIR spectrophotometric measurements. Interestingly, the observed center of each peak appears to be linearly dependent on the average size of the gold nanostars in solution, demonstrating the strong dependence of this plasmonic mode on the length of the spike, as described in the previous section and plotted in Figure 4d and 4e.

The results obtained from the ATR-FTIR spectra further underscore the ability and reliability of the developed protocol for the synthesis of colloidal nanostars with plasmonic properties that can be rationally tailored for specific applications. It is worth mentioning here that contrary to the well-defined, Gaussian-type predicted peaks by the model, in our ATR-FTIR spectra the first harmonic appears to be a convolution of more than one contribution in the overall spectral envelope. To address this issue, all the spectra were deconvoluted using Gauss functions based on the Levenberg–Marquardt algorithm as shown elsewhere.[90-93] The deconvoluted spectra show two or three major peaks separated by approximately 800 cm^{-1}. To further

investigate the latter, in Figure 4b and 4c we report the comparison between the deconvoluted ATR-FTIR spectrum and the calculated absorption cross section for 90 nm-spike nanostars. The distinct peaks in ATR-FTIR can be attributed to the same plasmonic mode under different geometrical configurations (Figure 4f). Numerical

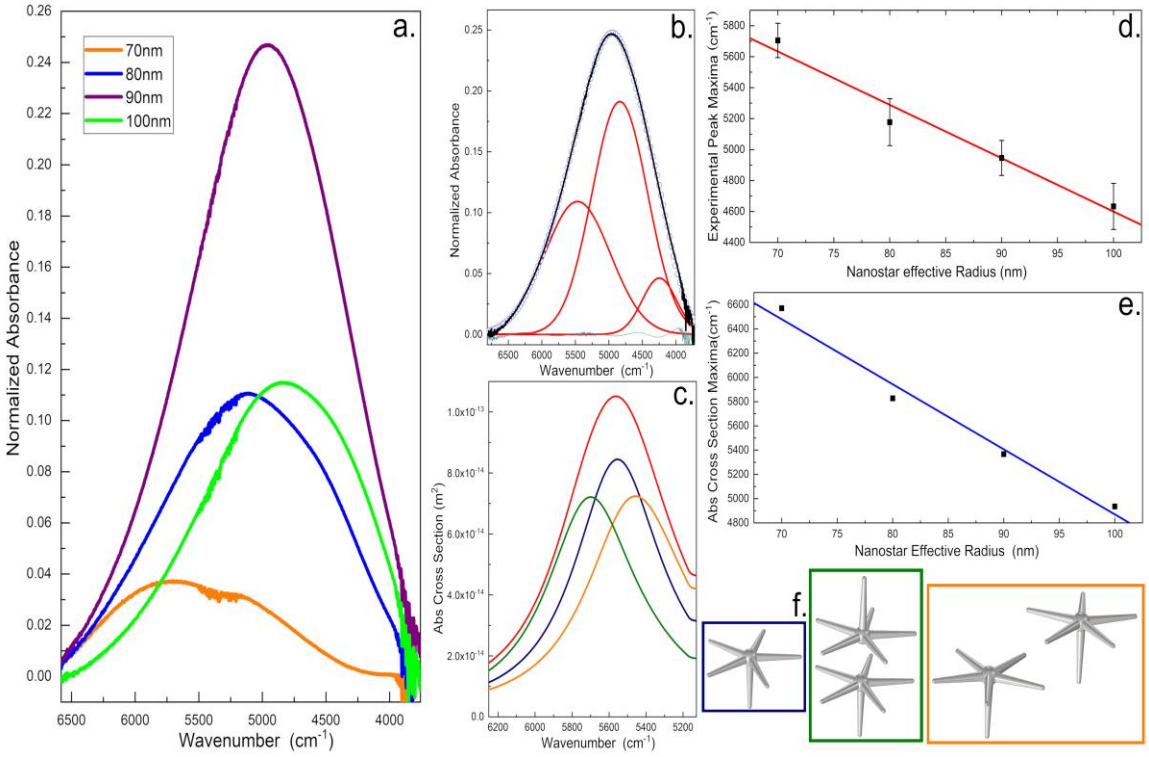

Figure 19. FTIR spectra collected on nanostars with 70 nm, 80 nm, 90 nm, and 100 nm spike lengths. Normalization carried out with respect to the area under the curve of each spectrum (a). Spectrum of a suspension of nanostars with 90 nm spike length deconvoluted with Gauss function (b). Theoretical absorption cross section spectra of 1) a single 90 nm nanostar, 2) two nanostars with their in-plane spikes kept parallel at 50 nm distance, 3) two nanostars aligned tip-to-tip at 50 nm, along with the average of these three spectra shown in red (c and f). Linear fitting of the observed FTIR peak maxima shows a strong interdependence between the first harmonic resonances and the spike length experimentally (d) and theoretically (e). Error bars in d) calculated from peak deconvolution, as reported in **Figure S7.**

results (Figure 4c and 4f) show that changing the distance as well as the configuration between two adjacent nanostars can both blue shift and red shift the plasmonic mode. The computational treatment to nanostar coupling aims to outline the importance of considering multiple geometric configurations between randomly dispersed adjacent nanostars at high concentrations when interpreting the experimental results. We have investigated three of these numerous possible configurations and report the shifts of the first harmonic with respect to the distance between nanostars (**Figure S17**).

Single particle measurements

To further prove that our model correctly predicted position and relative intensity of the resonant modes, we performed EELS studies to evaluate the plasmonic response of the gold nanostars at the single particle level. While single particle scattering data could be in first principle proposed to assess the plasmonic response, the presence of the substrates, coupling anisotropically to the nanostars, would have further complicated the experimental response, and was therefore not deemed accurate to assess the LSPR bands in this particular study. **Figure 20** exhibits EELS spectra acquired on a 6-spike nanostar with the electron beam probing the nanostructure in non-intersecting and intersecting geometries. Since the plasmon coupling between spikes is very weak due to their large physical separation,[94] one can in principle analyze their plasmonic behavior considering an isolated spike coupled to the star core. This approach allows us to probe a single spike and then repeat the process for the other spikes of the stars. We obtained the same findings for all the

spikes, as illustrated in Figure 20 (left side–spike 1; right side–spike 2). Note that the spectra can exhibit up to two resonances associated with the first (670 meV) and second (1360 meV) harmonic excitations, depending on the beam location. The resonant energies are similar to those found by optical techniques (UV-Vis-NIR and ATR-FTIR, Figures 18 and 19 respectively) and match well the computational findings. While we recognize that comparing mode excitation via electron beam and plane wave illumination involves different physical phenomena, we can consider the connection between electron and photon excitation to be valid in the aloof mode (*i.e.*, when the electron beam does not intersect the nanostructure). In intersecting geometry, on the other hand, two phenomena occur: a) The electron beam can probe coupled core-spike resonances with sufficient sensitivity to measure shifts due to the varying electron density, which increases as we move from the tip to the base of the

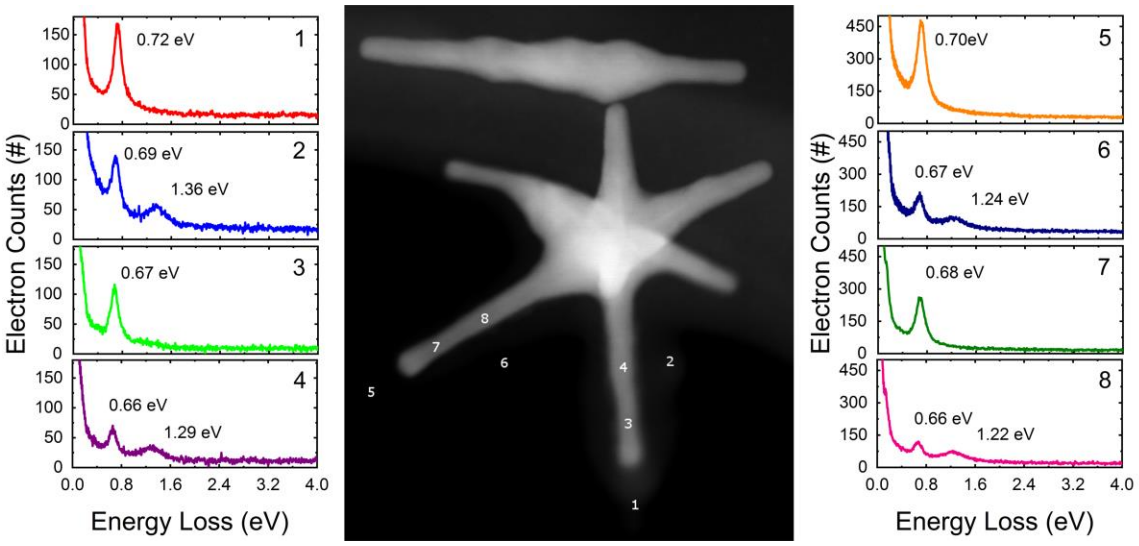

Figure 20. EELS spectra collected at the positions depicted in the STEM micrograph presented in the middle. Up to two resonances associated with the first (670 meV) and second (1360 meV) harmonic excitations can be observed, with slight energy shifts that depend on the proximity to the core of the position probed by the electron beam.

spike; b) The electron beam perturbs the local electron density leading to resonant mode damping. When the electron beam is located in regions near/within the tip (position 1, 3) the excitation of the first harmonic dominates the EELS spectra. This is expected due to the dipolar configuration of that mode in rod-like structures,[95] which is highly efficiently excited in the non-intersecting configuration (position 1). It is also important to note that there is a slight shift to lower energies of the characteristic resonance of the first harmonic, as we move along the axis of the spike (position 3), as explained onwards. We also probed the middle regions of the spikes producing an additional excitation at around 1290 meV, which corresponds to the excitation of the second harmonic. A blue-shift trend can be observed for the resonances excited, as we move from the middle regions of the spikes to their extremities and to the aloof mode. When the beam intersects with the spikes it disturbs the local charge distribution, which gives rise to the mentioned damping of the spike modes, giving rise to a red shift, notable in the case of the first harmonic as the beam moves from the aloof mode to the inner part of the spikes.

Chapter IV conclusions

In conclusion, the 6-branched nanostars reported herein offer an example of highly anisotropic, colloidally-synthesized plasmonic material in which the optical properties of the nanostructure can be predicted computationally and observed experimentally owing to the high monodispersity and reproducibility of the synthetic protocols. While other non-spherical nanoparticles (*e.g.* nanorods) have been synthesized with high degree of monodispersity and synthetic control, the morphology of the particles shown herein is substantially more complex to achieve. In-depth multi-

technique characterization has shown that the peak positions of the plasmonic resonances linearly depend on the length of the spikes, with slight variations originating from the specific tip- and spike-morphologies. The proposed model has predicted a strong plasmonic mode, along with its higher order eigenmodes, in excellent detail. EELS data, collected on isolated spikes, have confirmed the influence of the electrons of the core on the spectral position of the various harmonics; in addition, they have underscored the importance of taking into consideration the effect of the electron beam in intersecting probing geometries. From the single particle level to the highly interacting ensemble, the agreement between modeling and experiment advocates for the need of a combined approach towards a rational and effective evolution of plasmonic materials and methods. The high monodispersity and batch-to-batch reproducibility of the samples, ensured by our synthetic protocol, suggest that these 6-branched nanostars might be ideal testbeds for the experimental validation of plasmonics theory. The model has also suggested the presence of bulk image charges within the tips, that couple with the surface charges owing to the reduced thickness of the spikes. In addition, it appears to indicate that propagating polaritons, traveling along the high aspect ratio nanostar spikes, might coexist and interact with the highly localized modes at the tips. Ongoing studies in our lab are further investigating these observations and will be the focus of future work.

Chapter V: Conclusions and Perspectives

We introduced an approach to plasmonics that treats gold nanostar spikes as dual-cavity systems. One cavity is represented by the bulk of the spike and the other by the interface. Coupled bulk and interface polaritons propagate and form standing waves. As the boundary rule dictates, bulk standing waves exhibit maxima where interface standing waves exhibit minima. Contrary to what is known so far, gold nanostar tips are not-so-hot spots as the maximum field enhancement is evidenced on the surrounding medium directly next to the tip and not on the tip surface. We explored plasmonic coupling in systems of increasing complexity showing that FEM methods are complementary to hybridization theory and other methods that treat plasmonic particles as coupled systems of isolated domains. Exploring the coupling properties revealed vanishing harmonics and secondary resonances that occur when the distinct domains are studied together. In agreement to previous works otherwise, we also demonstrated systems where our view might be crucial to understanding the coupling mechanisms. Following the ongoing evolution of electron microscopy techniques, such as EELS and cathodoluminescence, we pinpointed the importance of bulk plasmons and their coupling to surface modes in a more holistic approach to plasmon resonances in elongated structures.

In comparison to experimentally synthesized particles we explored the relation between structural asymmetry and plasmonic shifts and broadenings. Driven by the demonstrated excellence of gold nanostars as SERS platforms, we utilized a partial SiO_2 coating of gold nanostar spikes to tune the intensity and position of the resonant bands. In very good agreement with experimental results of the same system, we

secured the usability of our method in structurally anisotropic and dielectrically complicated systems. Furthermore, and in line with the spirit of this work, the effects of the structural asymmetry and the presence of a dielectric medium can be successfully predicted with a modelled system based on many assumptions as long as it represents the average colloidal ensemble. Driven by this loose connection to the average sample behavior, we decided to take a closer look into the properties of one, real, isolated nanostar. By 3D STEM reconstruction and modelling, in parallel to and in comparison with a semi-empirical method, we examined the plasmonic properties of a real gold nanostar, shedding some more light into effective comparisons between isolated particles and synthesized colloidal mixtures. Lastly, we were the first to calculate the shape-dependent extinction coefficient of a plasmonic nanostar.

After having successfully studied most of the problems and inconsistencies of gold nanostar systems, as we describe them in the introduction, we took the next and final step of focusing on a form of nanostars that could potentially exhibit maximum tunability and applicability. The synthesis of this form of gold nanostars, 6-spiked and with spike lengths around 70-100 nm was optimized as described in chapter IV working in parallel between modelling and experiment. In-depth multi-technique characterization determined a linear dependence of the peak positions of the plasmonic resonances and the length of the spikes, promising to provide effective design rules for the synthesis on nanostars targeting specific properties and applications. The proposed model predicts a strong plasmonic mode, along with its higher order eigenmodes, covering a resonant window from 600 to 2000 nm. Single particle EELS confirmed the numerically predicted influence of the core electrons on the spectral position of the various spike harmonics. An experimental study of the

interparticle coupling, as numerically described in the first chapter, was experimentally explored with ATR-FTIR spectroscopy of a very dense colloid.

The accuracy of our modelling method in predicting the resonant properties of plasmonic nanostars from the single particle level to that of a highly entangled colloid, along with the detailed methods described in the first three chapters of this thesis, open a new chapter in what was known and expected so far from gold nanostars. There are still many questions however to be answered on the incredible properties of gold nanostars demonstrated by our group and others. From understanding the mechanisms of MRI signal enhancement to explaining most of the aspects of the various methods of nanostar synthesis and scalable production. Our work provides a detailed description of the mechanisms that drive the plasmonic coupling on multiple levels, focusing mostly on the electric field enhancement in the frequency domain. We have in the later stages of this work begun expanding our studies into the time domain. There are many interesting questions that arise, such as the phase information that characterizes the coupled bulk and interface polaritons and the limits where a resonance can be considered localized or propagating. This is perhaps the most astounding question elicited by this work. We have bulk and interface polaritons forming standing waves on the nanostar spikes. At what size limit do these resonances start to behave as localized and what is the timeframe at which the coupling occurs?

While still working computationally on these questions, our approach of gold nanostar spikes as dual coupled cavities can be utilized in the study of the fundamental properties of various types of plasmonic particles with electron microscopy methods that allow the detailed determination of the local and non-local

character of the resonant mechanisms. By adapting the incoming field to the field of an electron beam introduced in our method as e.g. a 1D current, one can explore and predict in detail what we have introduced in the first chapter and experimentally explored in the EELS study in the fourth chapter. The demonstrated coupling properties of spikes placed under different relative orientation with respect to the incoming field polarization can be utilized in the production of nanoparticle substrates (e.g. with oriented nanorods or bipyramids) with tunable and broad-band resonances. Our method for the 3D determination of the properties of real particles can be applied to the study of particles of any shape and size. The predictions of the SiO_2 coated nanostars can be applied to any system with nanoparticles covered with any semiconducting dielectric. Most importantly, the optimized, tunable and monodisperse few spiked nanostars presented in the fourth chapter stand as a paradigm of how we should work with nanoscale particles from now on. This concludes also the spirit of the present work. How to accurately predict the plasmonic properties of a 10^{14} nanostar colloid? 1) Model one average particle. 2) 3D Reconstruct one of the many and randomize the resonant conditions. 3) Or, start with modelling the system by strategically adding the constituent parts and studying their contribution individually and in coupled ensemble; and 4) optimize the synthesis method of the colloid by establishing a structure-property relationship.

Appendix I: Methods

FEM Simulations

Using a linearly polarized (LP) incident light source, as seen in **Equation S1**, with an electric field of amplitude 1 V/m, we simulated the optical properties of nanostars using a model developed in the RF Module of COMSOL Multiphysics 5.0.

(S1) $$\boldsymbol{E} = e^{-j\boldsymbol{k_0 z}}\,\hat{\boldsymbol{x}}$$

The simulations were based on numerical solutions of a time-averaged Laplacian, seen in **Equation S2**, employing the widely used Finite Element Method.

(S2) $$\nabla \times \frac{1}{\mu_r}(\nabla \times \boldsymbol{E}) - {k_0}^2\left(\varepsilon_r - \frac{j\sigma}{\omega\varepsilon_0}\right)\boldsymbol{E} = \boldsymbol{0}$$

The geometry was built on three concentric domains. A fully absorbing spherical layer, usually referred to as perfectly matched layer (PML), a layer assigned the dielectric properties of water, from Hale and Querry,[96] and a core domain including the various nanostar models assigned the dielectric properties of gold from the Lorentz–Drude model by Johnson and Christy[97]. The relative permeability μ_r was taken to be 1 in all geometry domains without loss of generality. The angular frequency ω was calculated from the input wavelength values.

The nanostar models were also developed in Comsol Multiphysics using mostly a spherical core, eccentric conical spikes with hemispherical, oblate, and prolate hemi

ellipsoidal tips. The volume and surface areas of these models are defined by **Equations S3** and **S4** with *i* being the number of spikes, varying from 1 to 50 in this work.

(S3) $$V = \frac{4}{3}\pi a^3 + \sum_{i=1}^{n}\left\{\frac{h_i}{3}\pi(R_i^2 + R_i r_i + r_i^2) + \frac{2}{3}\pi r_i^3 - \frac{\pi}{6}\left(a - \sqrt{a^2 - R_i^2}\right)\left[3R_i^2 + (a - \sqrt{a^2 - R_i^2})^2\right]\right\}$$

(S4) $$A = 4\pi a^2 - \sum_{i=1}^{n}\left\{2\pi a\left(a - \sqrt{a^2 - {R_i}^2}\right\}\right. + \sum_{i=1}^{n}\left\{\pi\left(r_i + R_i\right)\sqrt{(R_i - r_i)^2 + {h_i}^2} + 2\pi {r_i}^2\right\}$$

Furthermore, *a* is the radius of the spherical core, *R* is the base radius of a spike, *r* is the radius of the hemispherical tip of a spike, and *h* is the distance between *R* and *r*. Note that these equations describe only the cases of nanostars with hemispherical tips.

The various nanostar models were built to match the shapes and complexity of nanostars synthesized experimentally, and characterized via transmission electron microscopy (TEM), as described below. Herein, for sake of completeness, we compared the results collected via simulations to both those obtained on individual nanostars via electron energy loss spectroscopy (EELS) and to the ensemble averaged ones derived from the large-number statistical analysis of nanostar suspensions. Importantly, the excellent sample monodispersity and batch-to-batch reproducibility achievable with the synthetic protocol described herein, allow us, for the first time, to exactly match the plasmonic resonances observed experimentally to those calculated computationally, thus enabling us to identify new resonant and coupling modes in these nanoparticles.

The layered geometry was meshed employing randomly distributed tetrahedra, whose size was kept between 0.1 and 2 nm within the NS domain and at less than 4 nm in the surrounding medium domain. Numerical solutions of Equation 2 were accomplished through an iterative method in which the difference between individual solutions in the constituent tetrahedral elements is minimized within a tolerance of 10^{-6}. The whole procedure is based on convergence of the individual solutions within the above tolerance.

From the solution of Equation 2, we provide plots of the normalized scattered electric field. Three dimensional plots of the electric field norm (**Equation S5**) on the surface of the various NSs along with two-dimensional slice plots of the electric field norm are presented. 2D slice plots are fundamental to study, at the same time, surface and bulk plasmon modes in these nanoparticles.

(S5) $$|\boldsymbol{E}| = \sqrt{{E_x}^2 + {E_y}^2 + {E_z}^2}$$

In parallel, we calculate the absorption, scattering, and extinction cross sections, as defined by **Equations S6** and **S7**.

(S6) $$\sigma_{abs} = \frac{\boldsymbol{W}_{abs}}{\boldsymbol{P}_{inc}} \qquad \sigma_{sca} = \frac{\boldsymbol{W}_{sca}}{\boldsymbol{P}_{inc}}$$

(S7) $$\sigma_{ext} = \sigma_{abs} + \sigma_{sca}$$

The absorption and scattering cross sections are defined by the energy rates absorbed and scattered by the nanostar volume, defined in **Equations S8** and **S9** respectively, and divided by the incident irradiance, given by **Equation S10**:

(S8) $$\boldsymbol{W}_{abs} = \frac{1}{2}\iiint_{xyz} [\,\mathrm{Re}[(\sigma\mathbf{E} + j\omega\boldsymbol{D}) \cdot \mathbf{E}^*] + j\omega\boldsymbol{B}) \cdot \mathbf{H}^*]\ \mathrm{dxdydz}\ \ (\mathrm{W})$$

(S9) $$\boldsymbol{W}_{sca} = \oiint [\boldsymbol{E} \times \boldsymbol{H}^*] \cdot \mathbf{n}\mathrm{dS}\ \ (\mathrm{W})$$

(S10) $$\boldsymbol{P}_{inc} = \frac{1}{2Z_0}|\boldsymbol{E}_0|^2$$

where Z_0 is the impedance of free space and E_0 is the amplitude of the incident electric field, 1 V/m as seen in Equation 1.

Additionally, given the extinction cross section, we calculate the shape- and concentration-dependent extinction coefficient by multiplying the extinction cross section with the number density of nanostars as seen in **Equation S11**:

(S11) $$\varepsilon_{dep} = \sigma_{ext}\, n$$

Similarly, the absorption coefficient is given by **Equation S12**.

(S12) $$a = \sigma_{abs} n$$

This is a concentration dependent quantity, since it contains the number density of nanostars n. In this work, it is compared to the experimental absorption coefficient,

obtained from the measured absorbance from **Equation S15.** We deduce **Equation S15** by combining **Equation S13**, the Beer-Lambert law and the definition of absorption coefficient **Equation S14**, where Abs is the experimentally measured absorbance, I and I_0 the incident and transmitted light intensities, z the light path length through the cuvette holding the aqueous NS suspensions, and α_{exp} the experimental absorption coefficient.

(S13) $$Abs = log_{10}\frac{I_0}{I}$$

(S14) $$I = I_0\, e^{-\alpha_{exp} z}$$

(S15) $$\alpha_{exp} = \frac{\ln(10) Abs}{z}$$

The relationships described above allow us to directly compare the calculated absorption cross section spectra to the UV-Vis-NIR absorption spectra obtained experimentally. Furthermore, for an accurate representation of light-matter interactions in nanoscale objects, we will report both absorption and extinction coefficients, the latter to take into account the scattering contributions to the UV-Vis-NIR spectra collected experimentally.

Calculation of the Heat Losses Spectra

The physical quantity of resistive losses is given by **Equation S16**, where J is the current density vector and E* the complex conjugate of the electric field vector.

(S16) $$\text{Resistive Losses} = \frac{1}{2}\,\text{Re}[\mathbf{J}\cdot\mathbf{E}^{*}]\ \left(\frac{\text{W}}{\text{m}^3}\right)$$

Resistive losses are calculated as power per unit volume for each wavelength studied. Heat losses are calculated accordingly by integrating resistive losses over each nanostar total volume according to **Equation S17**.

(S17) $$\text{Heat Losses} = \iiint_{\text{xyz}} \left[\frac{1}{2}\,\text{Re}[\mathbf{J}\cdot\mathbf{E}^{*}]\right]\ \text{dxdydz}\ \ (\text{W})$$

Since that the current density vector is given by $\mathbf{J}=\sigma\mathbf{E}$, we can state that the heat losses are proportional to the square of the magnitude of the electric field vector in **Equation S18**.

(S18) $$\text{Heat Losses} \propto |\mathbf{E}|^2$$

Raman Measurements

Raman measurements were carried out with a Renishaw InVia Raman microscope equipped with a cooled charge-coupled device (CCD) detector using a 633 nm laser excitation and a 50× short working distance objective with NA of 0.75. Gold nanostars (0.5 nM) were deposited on microscope glass slides by tethering them via aminopropyltriethoxysilane (APTES). The slides were then incubated in a 1 μM solution of the Raman reporter molecule, aminothiophenol. The substrates were then washed, air-dried, and used for Raman analysis. The spectra were collected between 200 and 2000 cm^{-1} using a grating with 1200 l/mm. Spectra for each sample were

collected over six different locations and averaged for statistical significance. No relevant variation in the peak pattern was observed within each individual sample.

UV Vis Spectrophotometry

UV-Vis-NIR spectra of Au NS suspensions were obtained using a Thermo Scientific Evolution 300 Spectrometer.

High Resolution TEM

The NSs were imaged with high-resolution transmission electron microscopy (HR-TEM) at the Center for Functional Nanomaterials, at Brookhaven National Laboratories, employing a FEI Titan 80-300 kV. The highest spatial resolution achieved was 0.14 nm.

Semi-Empirical Study

Nanostar dimensions were measured using ImageJ software developed by the National Institutes of Health. To calculate the volumes of Au NSs, the cores were modeled as spheres and their spikes as eccentric cones with hemispherical tips; the spherical cap where each spike intersected with the core was subtracted. The volume of an individual Au NS modeled with this shape is given by **Equation S3** (*vide supra*). The number of atoms in a nanostar was determined from its volume and gold density as described in detail in Chapter III. Similarly, the surface area of a gold NS is calculated according to **Equation S4** (*vide supra*). The molar concentration of NSs in solution was calculated as the ratio between the total atomic gold concentration and the previously determined number of atoms per NS as determined via inductively

coupled plasma mass spectrometry (ICP-MS). The extinction coefficient was determined from Lambert Beer's Law (**Equation S19**):

(S19) $$\varepsilon = \frac{Abs}{bC}$$

Where ε is the NS extinction coefficient, *Abs* is the absorbance of the plasmon peak, C is the molar concentration of NSs, and b is the cell path length of the spectrophotometer (0.1 cm). The concentration of gold in solution was determined via ICP-MS, using a ThermoScientific Neptune Plus instrument.

Annular dark-field STEM tomography and 3D Reconstruction

A project image series of the NS was acquired from -70 degrees to +70 degrees with two-degree intervals in the high-angle annular dark-field scanning transmission electron microscopy (HAADF-STEM) imaging mode. The use of HAADF-STEM signals reduces diffraction contrast and renders image intensities approximating those of the projected atomic mass of the NS. The 3D tomograms of the NS were subsequently reconstructed using a custom-written MATLAB code with the multiplicative simultaneous iterative reconstruction technique. The isosurface rendition of the 3D reconstructed NS was performed in Avizo 6.0.

Dark Field Scattering Spectroscopy

Dark field scattering spectra were obtained using a Nikon Optiphot 66 optical microscope and an Andor Shamrock SR 303i imaging spectrometer equipped with a

250 µm slit. A CCD camera attached to the microscope was employed to collect 110×83 μm^2 images of the samples.

Transmission Electron Microscopy.

Nanoparticle morphology was determined using a Topcon 002B transmission electron microscope depositing the nanoparticle suspension on Ted Pella Inc. PELCO TEM grids.

ATR-FTIR Spectroscopy.

A Thermo Fisher iS50 FTIR spectrometer equipped with a deuterated, L-alanine-doped triglycine sulfate (DLaTGS) detector, and a Golden Gate single-reflection diamond ATR was used for all spectroscopic studies. The instrument was equipped with a purge gas of dehumidified air (Parker-Balston 75-45) to remove water vapor. The resolution of the instrument was set at 4 cm^{-1} for the whole set of measurements and the number of scans varied from 16 to 32. For each measurement, ~100 µl of the gold nanostar aqueous solution were placed on the ATR crystal and left there for 5 mins to settle. The spectra were collected at 25°C by using air as reference background.

Electron Energy Loss Spectroscopy.

A Nion high energy resolution monochromated EELS-STEM (HERMES™) with 60 keV acceleration voltage was employed to collect the reported EELS data.[98] Experimental conditions of high-beam current probes were used, typically attained

with a condenser-lens setting, favoring higher beam current over spatial resolution. The spatial resolution was kept between 1.5 Å and 2.0 Å. The EELS spectrometer entrance aperture subtends a 20-mrad (2.5 $Å^{-1}$) half-angle at 60 kV. The EELS spectra were acquired in the aloof and intersecting geometries over 500 ms and 1s, respectively, with 20 meV energy resolution. Plasma cleaning and mild heat treatment at 75°C for six hours were employed to pretreat the sample to eliminate the surfactant layer and avoid carbon contamination under the electron beam.

Spike Length Measurement of Gold Nanoparticles. (Chapter IV)

The core diameter, spike length, and aspect ratio of nanostars were measured *via* ImageJ and Gatan GMS3 software packages. The spike length was measured from the center of the core to the tip of the spike. We have measured 150 spikes for each different type nanostar to generate the reported statistics in Chapter IV.

Appendix II: Additional Data

Chapter I Supporting Data

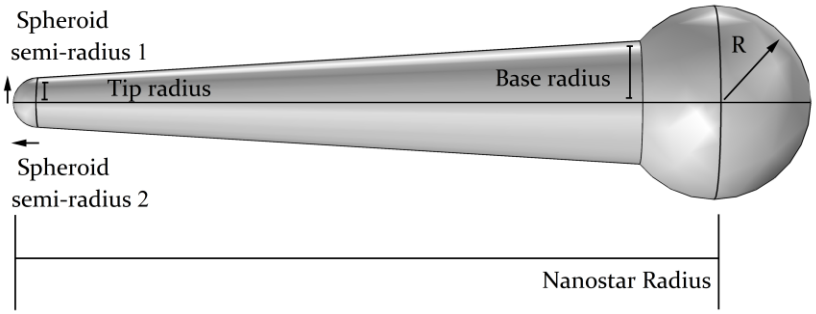

Figure S1: Constituent elements and geometry definitions of the simplest of the 3D models used in the numerical simulations performed in this work.

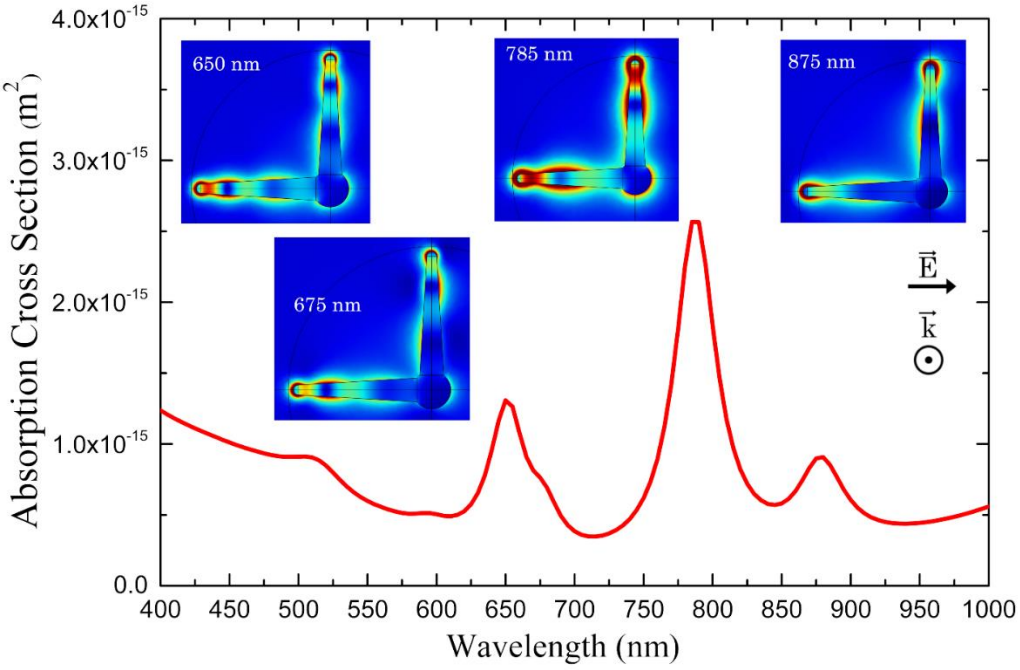

Figure S2: Secondary resonances observed in the case of a two-80 nm spike nanostar with the spikes kept at 90°. A very weak 4th harmonic resonance is also depicted at 595 nm. The secondary resonance in the case of the 3rd harmonic appears as a shoulder at 675 nm. Note the participation of the core in the main and stronger resonances at 650 and 785 nm and the asymmetric electric field distribution in the secondary resonances at 675 and 875 nm observed on the spikes perpendicular to the electric field polarization axis.

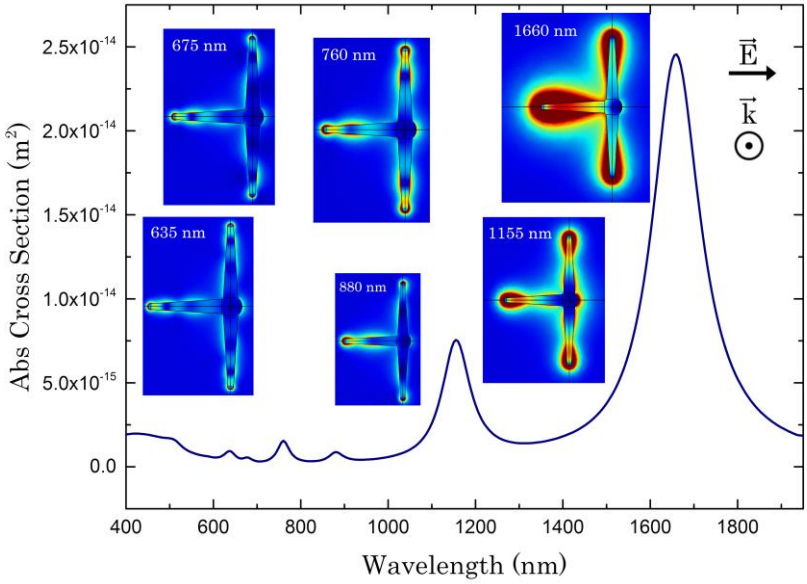

Figure S3: Secondary resonances observed in the case of a three-80 nm spike nanostar with two collinear spikes kept perpendicular to the electric field polarization axis. Note the relative intensity of the secondary modes at 675 and 880 nm in the visible range and the mode at 1155 nm in the SWIR. The secondary modes in the visible appear attenuated and redshifted compared to the main ones as the secondary mode in the SWIR appears attenuated and blue-shifted. Note also the asymmetric electric field profile of the secondary modes of the spikes perpendicular to the electric field polarization axis.

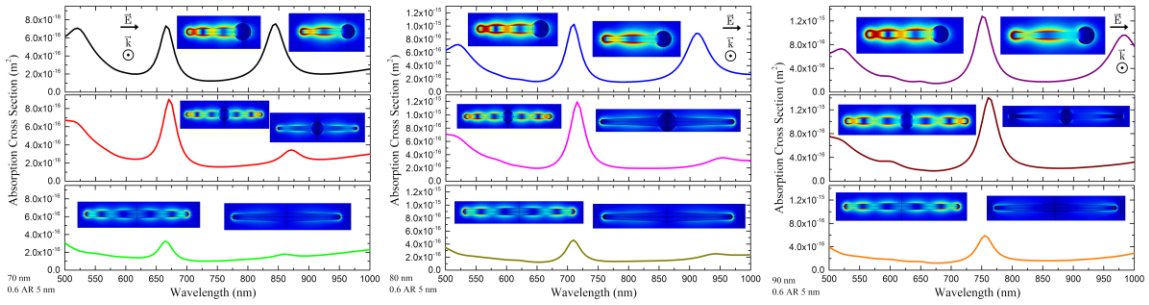

Figure S4: Progressive damping of the second harmonic as we vary the spike length from 70 to 80 to 90 nm while keeping the ratio between the base and tip *radii* and the spike thickness constant. Contrary to what is reported in the main text, both in the case of a bipyramid and a 2-spike nanostar we observe the damping of the second harmonic.

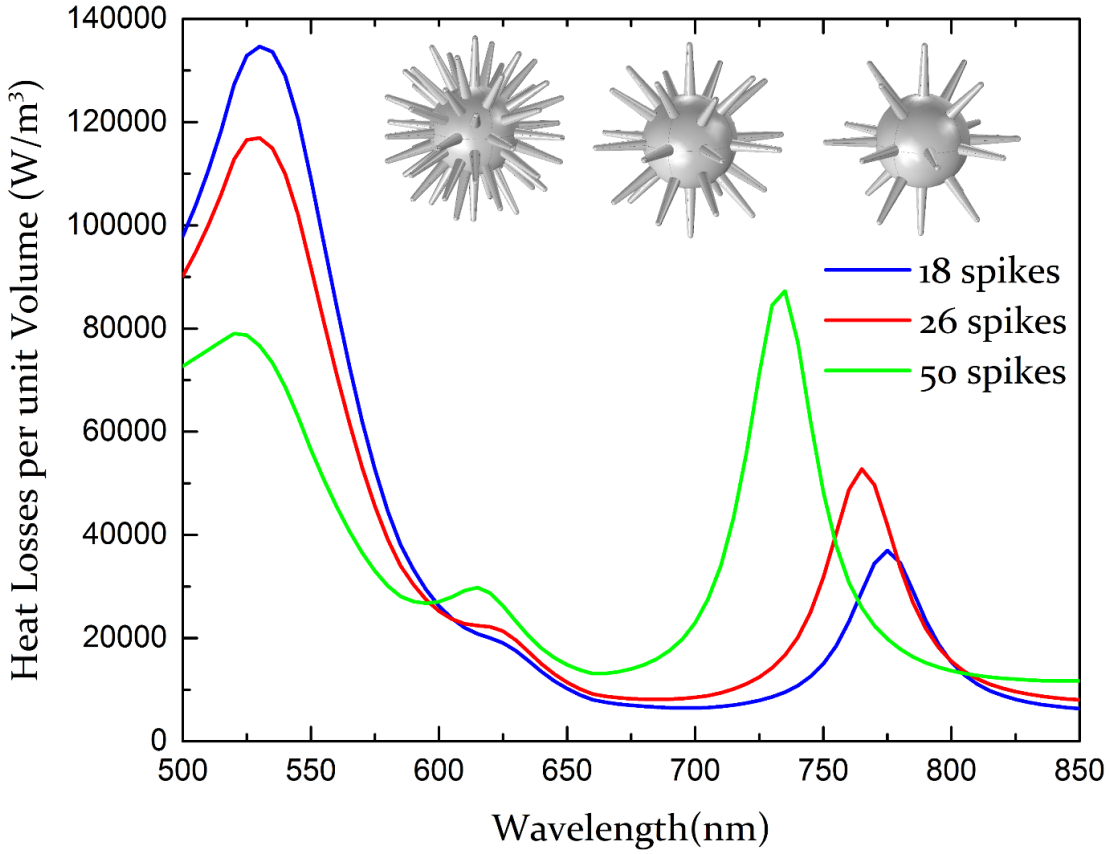

Figure S5: Test simulation with an oversized core decorated with 18, 26, and 50 spikes. We present the power losses per unit volume of each of the nanostars. A clear blue shift is observed as we increase the number of spikes, while the oversized core avoids spike intersection and ensures that the entire spike length participates in the charge oscillation and is responsible for the observed resonant modes. This ensures that our observation of the blue-shift is only due to the inter-spike coupling.

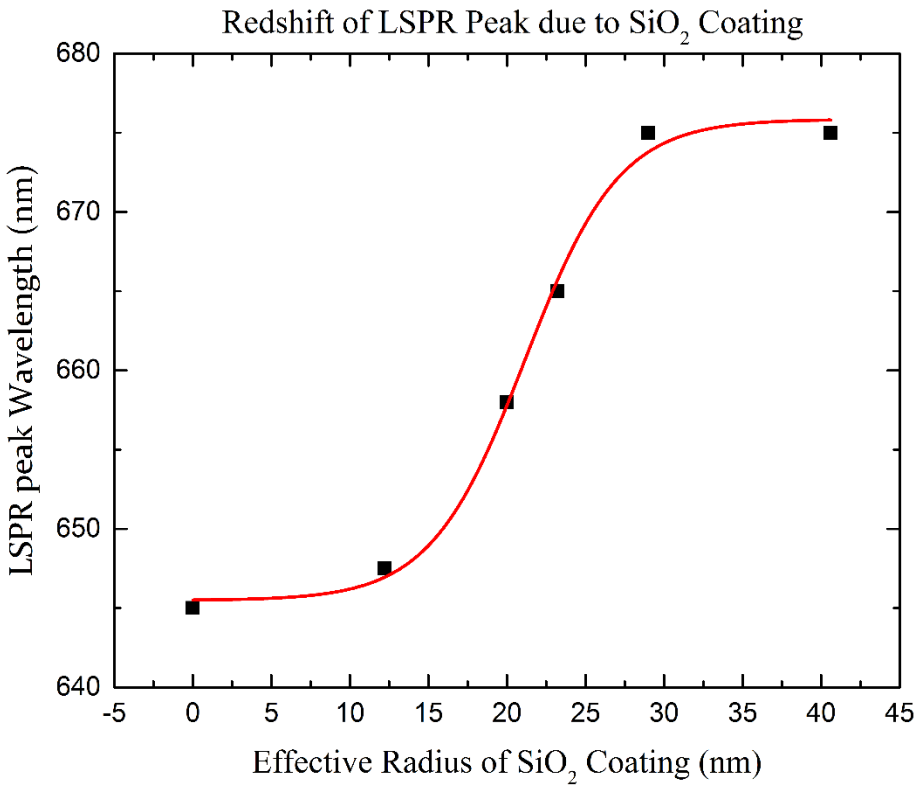

Figure S6: The LSPR position can be calculated for nanostars with silica coating of variable thickness by calculating heat losses. The resonance of the maximum red-shifts with the increase in shell thickness, following a double exponential dependence.

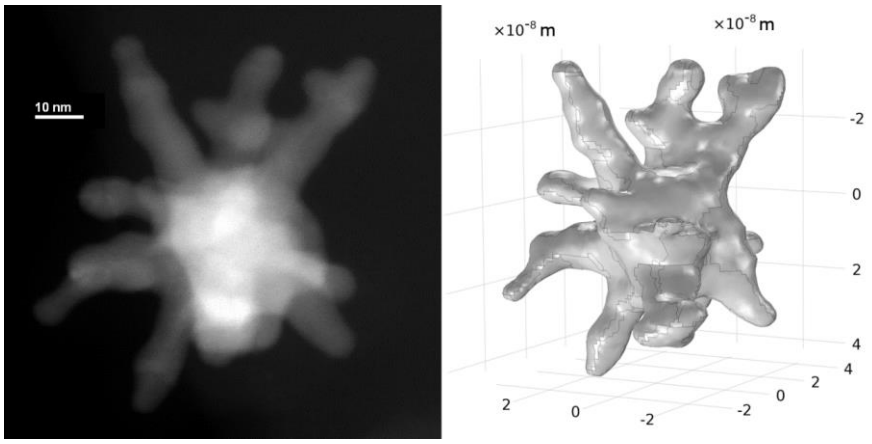

Figure S7. Comparison of STEM tomogram and model as employed for dimensional matching.

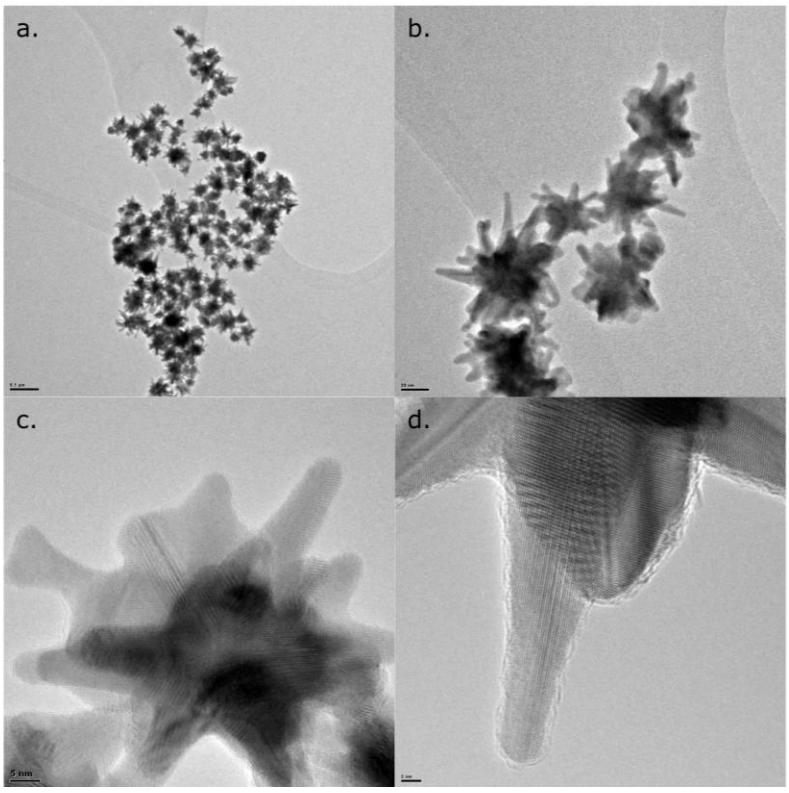

Figure S8. Additional TEM micrographs, collected at increasing magnification, of representative NSs used in this work. Scale bars are 100 nm (a), 20 nm (b), 5 nm (c), and 2 nm (d). Atomic packing in both core and tips can be observed.

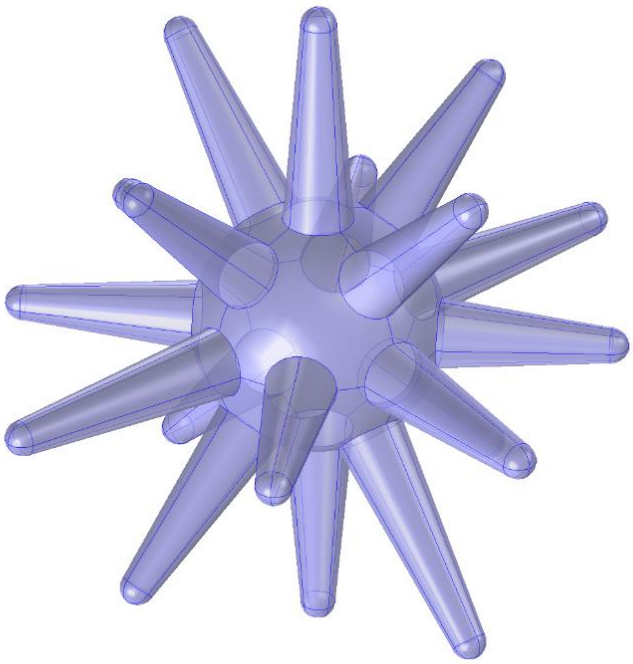

Figure S9. Representation of the nanostar model as defined by the analytical equation for its volume for a number of 18 spikes. (Equation S3 vide supra.)

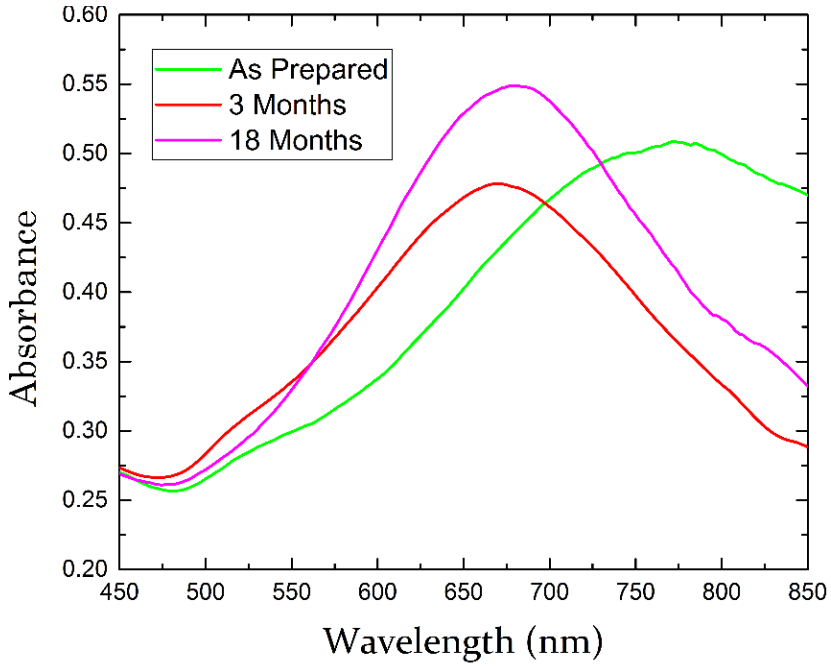

Figure S10: UV-Vis-NIR spectra of an aqueous suspension of gold nanostars, as prepared (green line), at the time that the STEM measurements took place (red line) and at the time that the dark field spectroscopy measurements took place (magenta).

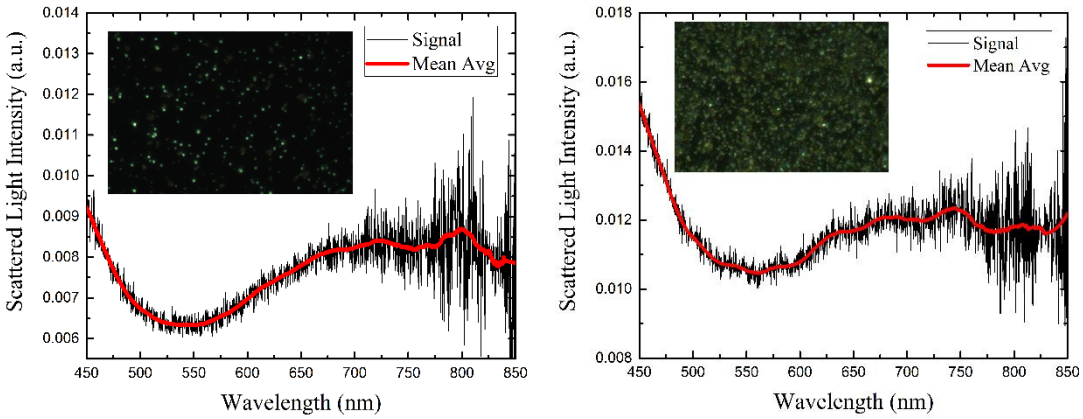

Figure S11. Additional Dark field spectra collected from the areas of the attached photographs depicting a broadening and a slight redshift in the case of a denser

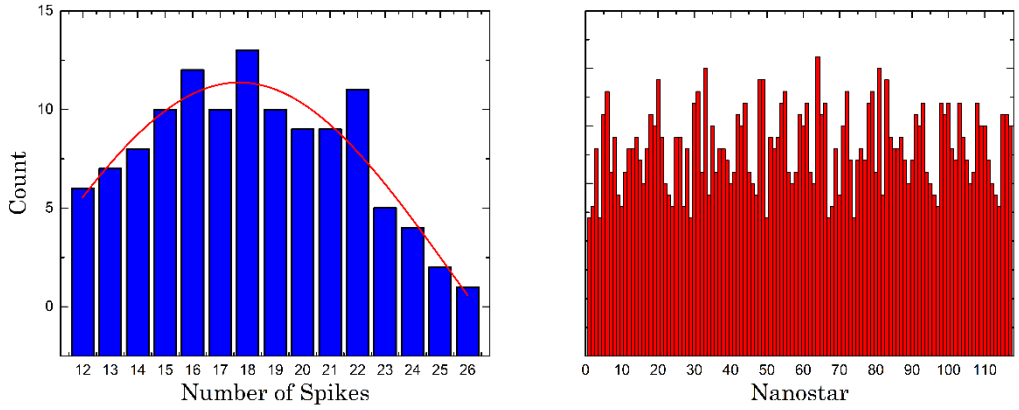

Figure S12. Number of spikes calculated from the 117 nanostars observed in the TEM micrograph of **Figure S2 a.** Raw data on the right and categorized frequency

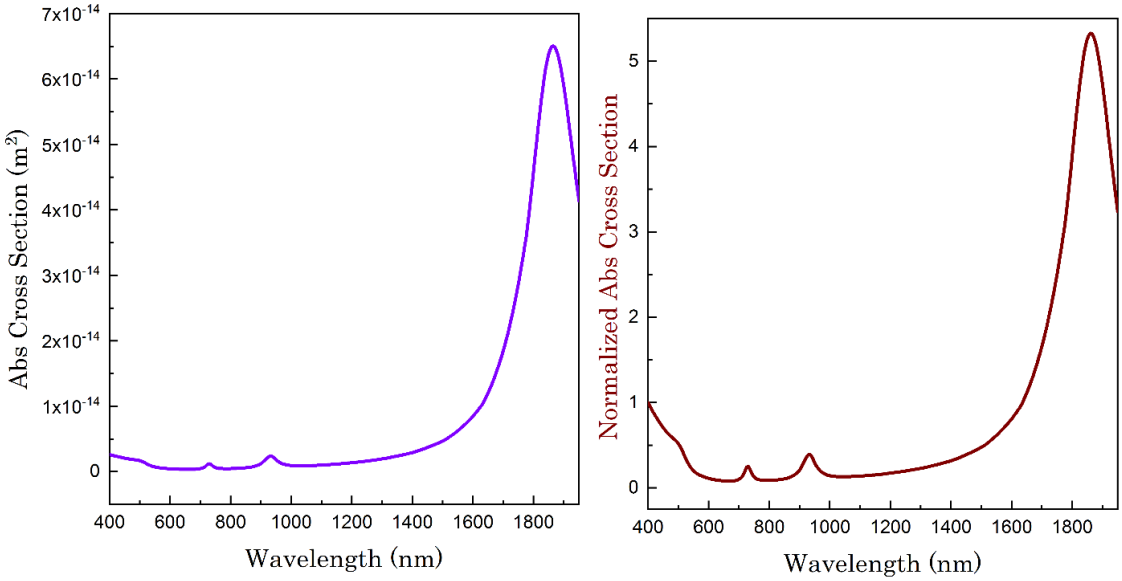

Figure S13: Comparison between the normalized absorption cross section spectrum (left, as presented in Figure 3e) in comparison to the full-range absorption cross section spectrum presented in Figure 3c. The normalization method consists of two steps. First, we divide the absorption cross section spectrum by the absorption cross section value at 400 nm. Second, we multiply the resulting values by the ratio between the photon energy at each wavelength and the photon energy of a 400 nm photon. As it can be observed, the relative peak intensities (normalized and not) do not change substantially, underscoring that the substantial intensity observed for the first harmonic mode is indeed an intrinsic property of the system studied.

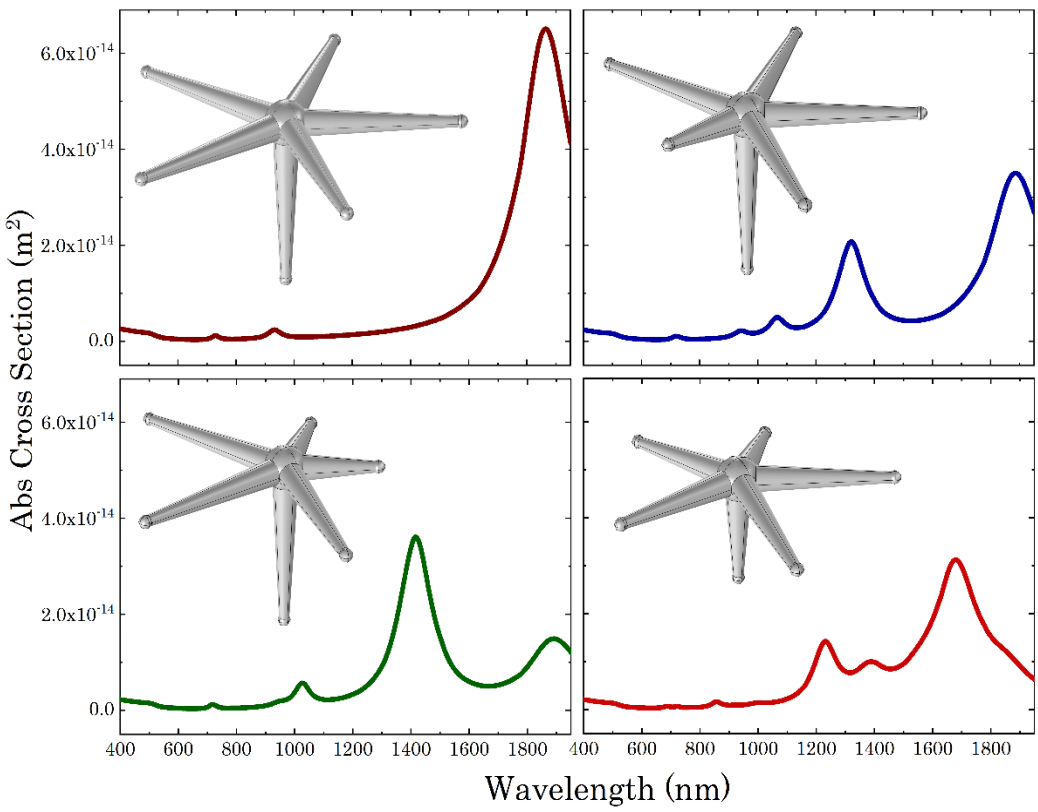

Figure S14: We demonstrate the shifts of the harmonics and additional hybrid resonances that arise when we introduce disruptions in the geometry of a 90 nm-spike gold nanostar. Starting by halving the length of one of the spikes, we elaborate by halving the length of two spikes, and end up with a nanostar with 6 spikes with different lengths. Clearly there are additional resonances appearing that correspond to shifted resonances of the shorter spikes and hybrid ones that correspond to mixed states, *e.g.* the second harmonic of one spike resonates with the third harmonic of another spike. It is important to note also that, contrary to the symmetric structure depicted in the first graph (as also presented in the main text), the 6th spike placed perpendicular to the five in-plane spikes participates with higher intensity to all of the resonances in all of the three disrupted cases presented.

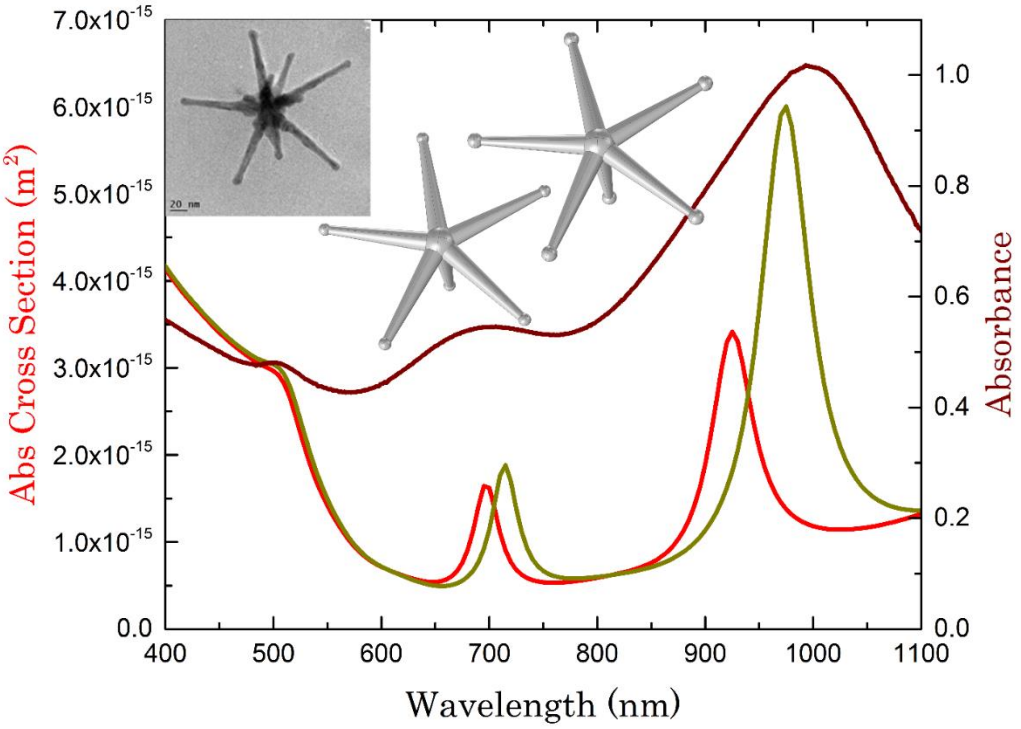

Figure S15. Juxtaposition of the experimental absorption spectrum collected on a suspension of nanostars with 100 nm spike length (TEM micrograph in inset) and two theoretical absorption cross section spectra calculated to model the optical response of nanostars characterized by spikes of slightly different aspect ratios, as defined in the main text (0.5 and 0.45 respectively). The resulting theoretical spectra exhibit notable shifts both for the second (at ca. 1000 nm) and the third (at ca. 700 nm) harmonic modes, while no shift is observed in the case of the spherical mode (at ca. 520 nm). Given that the two theoretical spectra were calculated to model individual nanostars while the experimental spectrum was collected on an ensemble of approximately 10^{14} nanostars suspended in aqueous medium, the peak broadening observed experimentally can be safely assigned to only slight differences in nanostar morphology within a batch. The good agreement between theory and experiment confirms not only the validity of our model but also the monodispersity achievable with our synthetic approach.

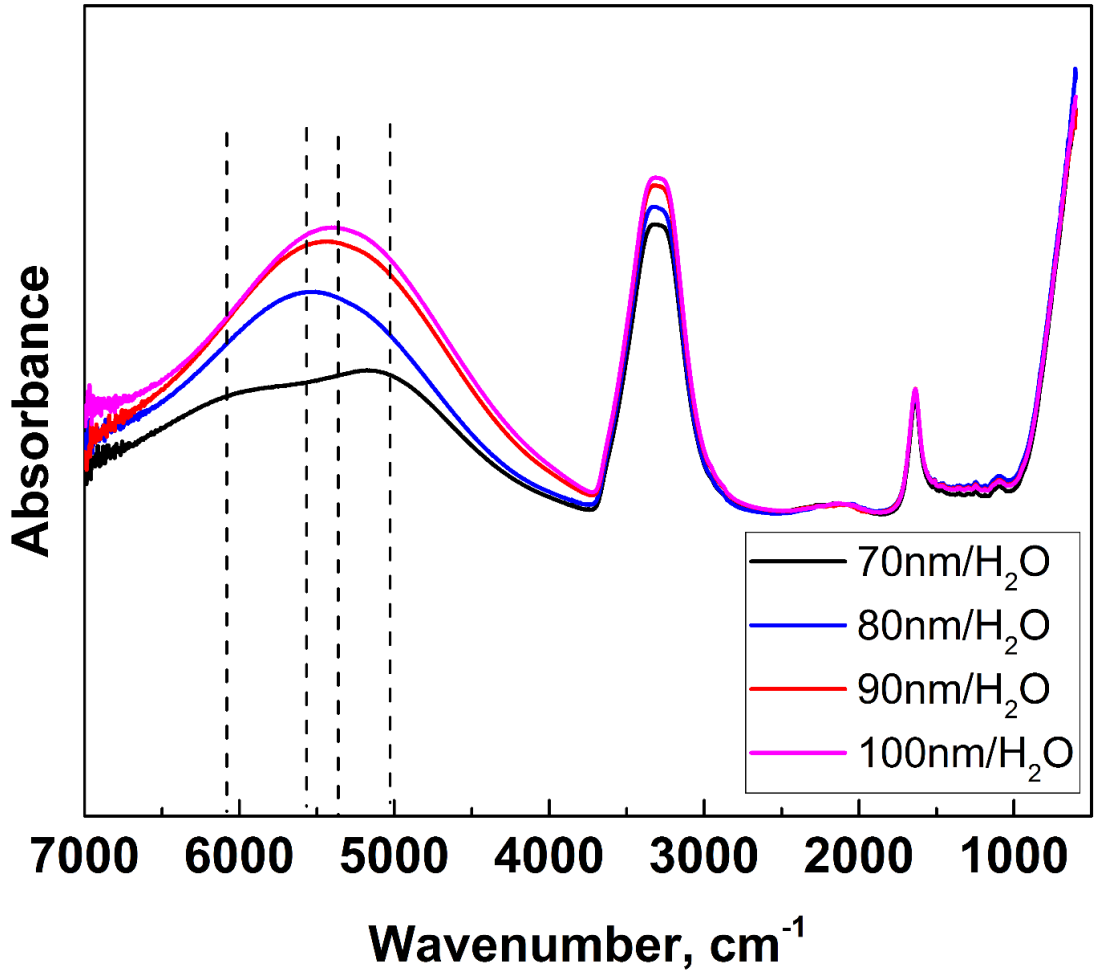

Figure S16. ATR-FTIR spectra of highly concentrated aqueous dispersions of gold nanostars with spike lengths spanning between 70 nm and 100 nm. Full spectral range, 700-7500 cm^{-1}.

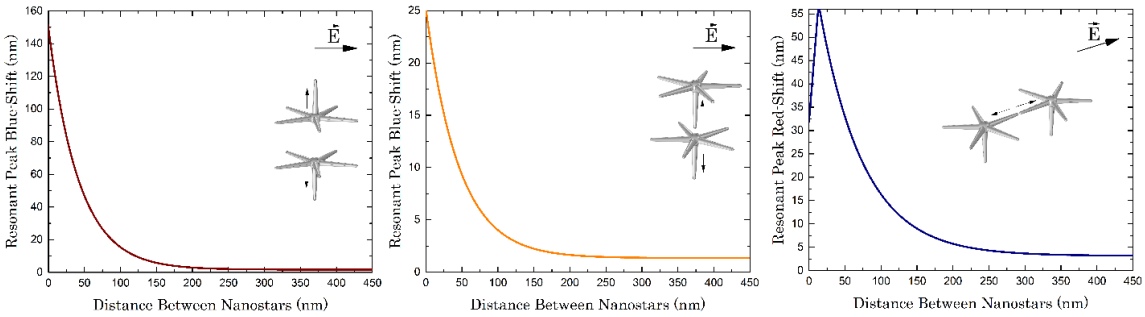

Figure S17. Quantification of the plasmonic shifts for the resonant first harmonic peak in the case of coupling of two nanostars under three different configurations. The distance in every case is defined as the physical separation between the metallic surfaces of the two adjacent nanostars. The first two configurations from the left resulted in blue-shifts, while the third resulted in a redshift that reverts at ca. 14 nm. The behavior observed for the first two configurations can be in first approximation explained by drawing a parallel to two nanorods coupling side-by-side. The behavior observed for the third configuration requires more insight. The linear region corresponds to the first few nanometers of separation between the tips coupling tip-to-tip. Within this region, because the first harmonic mode of the scattered enhanced field of the first nanostar reaches far enough to enter in resonance with the field localized at the core of the adjacent one, a strong resonance and a red-shift occur leading to an optimal coupling at ca. 14 nm. Beyond 14 nm of tip-to-tip separation the effect is reversed, as the coupling between the cores and the spikes of the adjacent nanostars weakens leading only the tips to interact, similar to two nanorods coupling tip-to-tip. Modeling of the interactions for various configurations and separation, allows us to better interpret the FTIR data and compare these results to the theoretical predictions and the Vis-NIR spectra. ATR-FTIR data were in fact collected at higher sample concentration than the Vis-NIR experiments, thus likely bringing the nanostars in close proximity to each other and, possibly, leading them to couple.

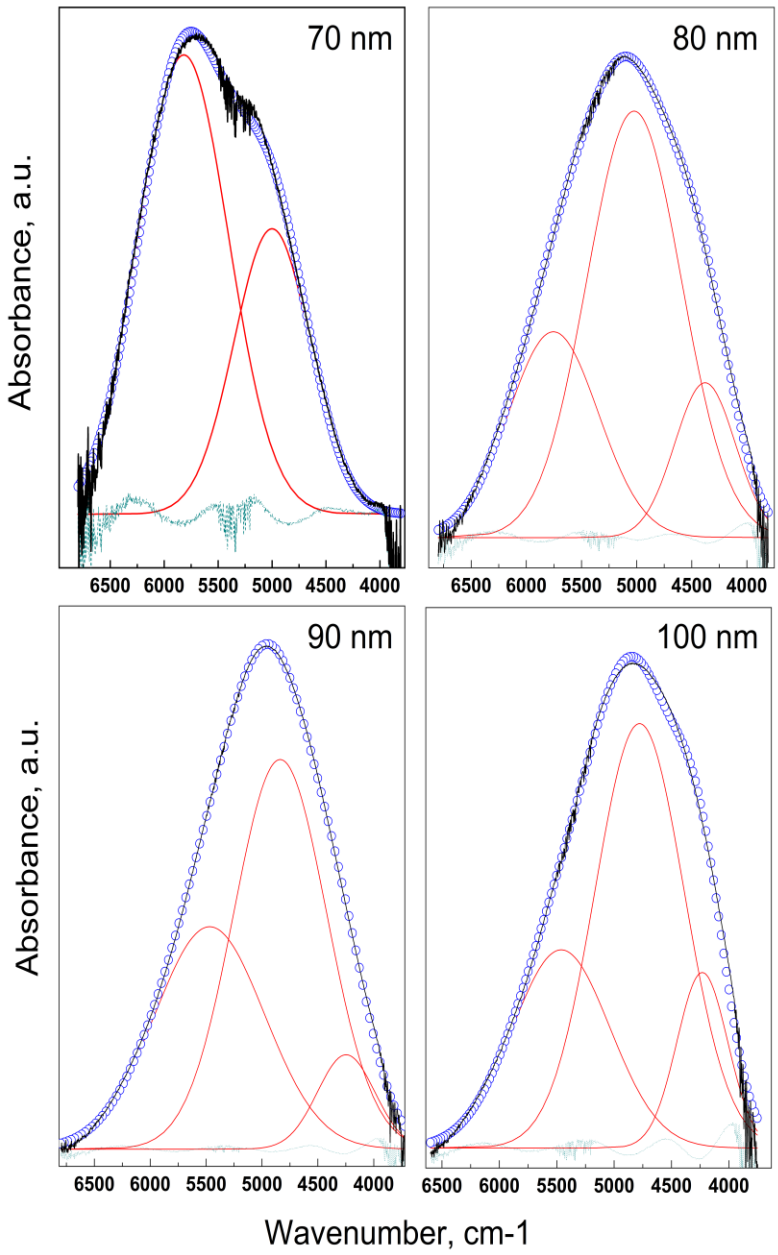

Figure S18. ATR-FTIR peak deconvolution carried out using Gauss functions based on the Levenberg–Marquardt algorithm. The error bars used in Figure 5d) were determined as the spectral distances between the experimentally determined peak maxima and the most intense of the peaks used for the deconvolution of each of the four spike-length cases.

Acknowledgment of Previous Publications

Chapter I of this thesis is based on our just accepted paper in The Journal of Physical Chemistry C, Section: C: Plasmonics; Optical, Magnetic, and Hybrid Materials: "Interface and Bulk Standing Waves Drive the Coupling of Plasmonic Nanostar Antennas". T.V. Tsoulos, L. Fabris. **2018.**

Chapter II of this thesis is based on our published paper in The Journal of Physical Chemistry C, Section: C: Plasmonics; Optical, Magnetic, and Hybrid Materials: "Shaping Gold Nanostar Electric Fields for Surface-Enhanced Raman Spectroscopy Enhancement via Silica Coating and Selective Etching". S. Atta, T.V. Tsoulos, L. Fabris. J. Phys. Chem. C, 120 (37), 20749-207585, **2016**.[53]

Chapter III of this thesis is based on our published paper in Nanoscale: "A closer look at the physical and optical properties of gold nanostars: an experimental and computational study". T.V. Tsoulos, L. Han, J. Weir, H.L. Xin, L. Fabris. Nanoscale, 9 (11), 3766-3773, **2017**. This work was also recently highlighted by the United States Department of Energy, Office of Science: (https://science.energy.gov/bes/highlights/2018/bes-2018-09-a/).[52]

Chapter IV of this thesis is based on our ChemRxiv paper: "Rational Design of Gold Nanostars with Tailorable Plasmonic Properties". T.V. Tsoulos, S. Atta, M.J. Lagos, P.E. Batson, G. Tsilomelekis, L. Fabris. (DOI: 10.26434/chemrxiv.6552743), **2018**.[43]

Bibliography

1. Rotz, M. W.; Culver, K. S. B.; Parigi, G.; MacRenaris, K. W.; Luchinat, C.; Odom, T. W.; Meade, T. J., High Relaxivity Gd(III)–DNA Gold Nanostars: Investigation of Shape Effects on Proton Relaxation. *ACS Nano* **2015,** *9* (3), 3385-3396.
2. Indrasekara, A. S. D. S.; Meyers, S.; Shubeita, S.; Feldman, L. C.; Gustafsson, T.; Fabris, L., Gold nanostar substrates for SERS-based chemical sensing in the femtomolar regime. *Nanoscale* **2014,** *6* (15), 8891-8899.
3. Sousa-Castillo, A.; Comesaña-Hermo, M.; Rodríguez-González, B.; Pérez-Lorenzo, M.; Wang, Z.; Kong, X.-T.; Govorov, A. O.; Correa-Duarte, M. A., Boosting Hot Electron-Driven Photocatalysis through Anisotropic Plasmonic Nanoparticles with Hot Spots in Au–TiO2 Nanoarchitectures. *J. Phys. Chem. C* **2016,** *120* (21), 11690-11699.
4. Bhamidipati, M.; Fabris, L., Multiparametric Assessment of Gold Nanoparticle Cytotoxicity in Cancerous and Healthy Cells: The Role of Size, Shape, and Surface Chemistry. *Bioconjugate Chem.* **2017,** *28* (2), 449-460.
5. Liu, Y.; Yuan, H.; Fales, A.; Register, J.; Vo-Dinh, T., Multifunctional gold nanostars for molecular imaging and cancer therapy. *Front. Chem.* **2015,** *3* (51).
6. Ginting, R. T.; Kaur, S.; Lim, D.-K.; Kim, J.-M.; Lee, J. H.; Lee, S. H.; Kang, J.-W., Plasmonic Effect of Gold Nanostars in Highly Efficient Organic and Perovskite Solar Cells. *ACS Appl. Mater. Interfaces* **2017,** *9* (41), 36111-36118.
7. Munkhbat, B.; Ziegler, J.; Pöhl, H.; Wörister, C.; Sivun, D.; Scharber, M. C.; Klar, T. A.; Hrelescu, C., Hybrid Multilayered Plasmonic Nanostars for Coherent Random Lasing. *J. Phys. Chem. C* **2016,** *120* (41), 23707-23715.
8. Hrelescu, C.; Sau, T. K.; Rogach, A. L.; Jäckel, F.; Feldmann, J., Single gold nanostars enhance Raman scattering. *Appl. Phys. Lett.* **2009,** *94* (15), 153113.
9. Shao, L.; Susha, A. S.; Cheung, L. S.; Sau, T. K.; Rogach, A. L.; Wang, J., Plasmonic Properties of Single Multispiked Gold Nanostars: Correlating Modeling with Experiments. *Langmuir* **2012,** *28* (24), 8979-8984.
10. Hrelescu, C.; Sau, T. K.; Rogach, A. L.; Jäckel, F.; Laurent, G.; Douillard, L.; Charra, F., Selective Excitation of Individual Plasmonic Hotspots at the Tips of Single Gold Nanostars. *Nano Lett.* **2011,** *11* (2), 402-407.
11. Hao, F.; Nehl, C. L.; Hafner, J. H.; Nordlander, P., Plasmon Resonances of a Gold Nanostar. *Nano Lett.* **2007,** *7* (3), 729-732.
12. Prodan, E.; Radloff, C.; Halas, N. J.; Nordlander, P., A Hybridization Model for the Plasmon Response of Complex Nanostructures. *Science* **2003,** *302* (5644), 419.
13. Rewitz, C.; Keitzl, T.; Tuchscherer, P.; Huang, J.-S.; Geisler, P.; Razinskas, G.; Hecht, B.; Brixner, T., Ultrafast Plasmon Propagation in Nanowires Characterized by Far-Field Spectral Interferometry. *Nano Lett.* **2012,** *12* (1), 45-49.
14. Payne, E. K.; Shuford, K. L.; Park, S.; Schatz, G. C.; Mirkin, C. A., Multipole Plasmon Resonances in Gold Nanorods. *J. Phys. Chem. B* **2006,** *110* (5), 2150-2154.

15. Piazza, L.; Lummen, T. T. A.; Quiñonez, E.; Murooka, Y.; Reed, B. W.; Barwick, B.; Carbone, F., Simultaneous observation of the quantization and the interference pattern of a plasmonic near-field. *Nat. Commun.* **2015,** *6*, 6407.
16. Ortiz, N.; Zoellner, B.; Hong, S. J.; Ji, Y.; Wang, T.; Liu, Y.; Maggard, P. A.; Wang, G., Harnessing Hot Electrons from Near IR Light for Hydrogen Production Using Pt-End-Capped-AuNRs. *ACS Appl. Mater. Interfaces* **2017,** *9* (31), 25962-25969.
17. González-Rubio, G.; Díaz-Núñez, P.; Rivera, A.; Prada, A.; Tardajos, G.; González-Izquierdo, J.; Bañares, L.; Llombart, P.; Macdowell, L. G.; Alcolea Palafox, M.; Liz-Marzán, L. M.; Peña-Rodríguez, O.; Guerrero-Martínez, A., Femtosecond laser reshaping yields gold nanorods with ultranarrow surface plasmon resonances. *Science* **2017,** *358* (6363), 640-644.
18. Hamon, C.; Postic, M.; Mazari, E.; Bizien, T.; Dupuis, C.; Even-Hernandez, P.; Jimenez, A.; Courbin, L.; Gosse, C.; Artzner, F.; Marchi-Artzner, V., Three-Dimensional Self-Assembling of Gold Nanorods with Controlled Macroscopic Shape and Local Smectic B Order. *ACS Nano* **2012,** *6* (5), 4137-4146.
19. Nehl, C. L.; Liao, H.; Hafner, J. H., Optical Properties of Star-Shaped Gold Nanoparticles. *Nano Lett.* **2006,** *6* (4), 683-688.
20. Khoury, C. G.; Vo-Dinh, T., Gold Nanostars For Surface-Enhanced Raman Scattering: Synthesis, Characterization and Optimization. *The journal of physical chemistry. C, Nanomaterials and interfaces* **2008,** *2008* (112), 18849-18859.
21. Hsiangkuo, Y.; Christopher, G. K.; Hanjun, H.; Christy, M. W.; Gerald, A. G.; Tuan, V.-D., Gold nanostars: surfactant-free synthesis, 3D modelling, and two-photon photoluminescence imaging. *Nanotechnology* **2012,** *23* (7), 075102.
22. Zhihua, X.; Kong, W.; Cheng, L.; Ma, A.; Lu, X.; Wang, Y.; Zhang, X.; Ya Zhang, X., *Universal Three-Dimensional Polarization-Dependent Optical Properties in Anisotropic Plasmonic Nanostar: a Route Boosting Single Particle 3D Orientation Determination and Orientation-Unlimited Polarization Information Detection*. 2015; Vol. 10.
23. Theodorou, I. G.; Jiang, Q.; Malms, L.; Xie, X.; Coombes, R. C.; Aboagye, E. O.; Porter, A. E.; Ryan, M. P.; Xie, F., Fluorescence enhancement from single gold nanostars: towards ultra-bright emission in the first and second near-infrared biological windows. *Nanoscale* **2018,** *10* (33), 15854-15864.
24. Zia, R.; Selker, M. D.; Catrysse, P. B.; Brongersma, M. L., Geometries and materials for subwavelength surface plasmon modes. *J. Opt. Soc. Am. A* **2004,** *21* (12), 2442-2446.
25. Weeber, J.-C.; Dereux, A.; Girard, C.; Krenn, J. R.; Goudonnet, J.-P., Plasmon polaritons of metallic nanowires for controlling submicron propagation of light. *Phys. Rev. B* **1999,** *60* (12), 9061-9068.
26. Koh, A. L.; Bao, K.; Khan, I.; Smith, W. E.; Kothleitner, G.; Nordlander, P.; Maier, S. A.; McComb, D. W., Electron Energy-Loss Spectroscopy (EELS) of Surface

Plasmons in Single Silver Nanoparticles and Dimers: Influence of Beam Damage and Mapping of Dark Modes. *ACS Nano* **2009,** *3* (10), 3015-3022.

27. Mock, J. J.; Hill, R. T.; Degiron, A.; Zauscher, S.; Chilkoti, A.; Smith, D. R., Distance-Dependent Plasmon Resonant Coupling between a Gold Nanoparticle and Gold Film. *Nano Lett.* **2008,** *8* (8), 2245-2252.

28. Hoang, C. V.; Hayashi, K.; Ito, Y.; Gorai, N.; Allison, G.; Shi, X.; Sun, Q.; Cheng, Z.; Ueno, K.; Goda, K.; Misawa, H., Interplay of hot electrons from localized and propagating plasmons. *Nat. Commun.* **2017,** *8* (1), 771.

29. Paolo, B.; Jer-Shing, H.; Bert, H., Nanoantennas for visible and infrared radiation. *Rep. Prog. Phys.* **2012,** *75* (2), 024402.

30. Knight, M. W.; Liu, L.; Wang, Y.; Brown, L.; Mukherjee, S.; King, N. S.; Everitt, H. O.; Nordlander, P.; Halas, N. J., Aluminum Plasmonic Nanoantennas. *Nano Lett.* **2012,** *12* (11), 6000-6004.

31. Nicoletti, O.; Wubs, M.; Mortensen, N. A.; Sigle, W.; van Aken, P. A.; Midgley, P. A., Surface plasmon modes of a single silver nanorod: an electron energy loss study. *Opt. Express* **2011,** *19* (16), 15371-15379.

32. Ritchie, R. H., Plasma Losses by Fast Electrons in Thin Films. *Phys. Rev.* **1957,** *106* (5), 874-881.

33. Schuller, J. A.; Barnard, E. S.; Cai, W.; Jun, Y. C.; White, J. S.; Brongersma, M. L., Plasmonics for extreme light concentration and manipulation. *Nat. Mater.* **2010,** *9*, 368.

34. Batson, P. E., Surface Plasmon Coupling in Clusters of Small Spheres. *Phys. Rev. Lett.* **1982,** *49* (13), 936-940.

35. Batson, P. E., Inelastic scattering of fast electrons in clusters of small spheres. *Surf. Sci.* **1985,** *156*, 720-734.

36. Batson, P. E., A new surface plasmon resonance in clusters of small aluminum spheres. *Ultramicroscopy* **1982,** *9* (3), 277-282.

37. Maier, S. A.; Atwater, H. A., Plasmonics: Localization and guiding of electromagnetic energy in metal/dielectric structures. *J. Appl. Phys.* **2005,** *98* (1), 011101.

38. Miyazaki, H. T.; Kurokawa, Y., Squeezing Visible Light Waves into a 3-nm-Thick and 55-nm-Long Plasmon Cavity. *Phys. Rev. Lett.* **2006,** *96* (9), 097401.

39. Mkhoyan, K. A.; Babinec, T.; Maccagnano, S. E.; Kirkland, E. J.; Silcox, J., Separation of bulk and surface-losses in low-loss EELS measurements in STEM. *Ultramicroscopy* **2007,** *107* (4), 345-355.

40. Hong, B. H.; Bae, S. C.; Lee, C.-W.; Jeong, S.; Kim, K. S., Ultrathin Single-Crystalline Silver Nanowire Arrays Formed in an Ambient Solution Phase. *Science* **2001**.

41. Gildenburg, V. B.; Kostin, V. A.; Pavlichenko, I. A., Excitation of surface and volume plasmons in a metal nanosphere by fast electrons. *Phys. Plasmas* **2016,** *23* (3), 032120.

42. Lemke, C.; Leißner, T.; Evlyukhin, A.; Radke, J. W.; Klick, A.; Fiutowski, J.; Kjelstrup-Hansen, J.; Rubahn, H.-G.; Chichkov, B. N.; Reinhardt, C.; Bauer, M., The Interplay between Localized and Propagating Plasmonic Excitations Tracked in Space and Time. *Nano Lett.* **2014,** *14* (5), 2431-2435.
43. Ted V., T.; Supriya, A.; Maureen J., L.; Philip E., B.; George, T.; Laura, F., *Rational Design of Gold Nanostars with Tailorable Plasmonic Properties*. 2018.
44. Rossouw, D.; Couillard, M.; Vickery, J.; Kumacheva, E.; Botton, G. A., Multipolar Plasmonic Resonances in Silver Nanowire Antennas Imaged with a Subnanometer Electron Probe. *Nano Lett.* **2011,** *11* (4), 1499-1504.
45. Nelayah, J.; Kociak, M.; Stéphan, O.; García de Abajo, F. J.; Tencé, M.; Henrard, L.; Taverna, D.; Pastoriza-Santos, I.; Liz-Marzán, L. M.; Colliex, C., Mapping surface plasmons on a single metallic nanoparticle. *Nat. Phys.* **2007,** *3*, 348.
46. Rivacoba, A.; Apell, P.; Zabala, N., Energy loss probability of STEM electrons in cylindrical surfaces. *Nucl. Instrum. Methods Phys. Res., Sect. B* **1995,** *96* (3), 465-469.
47. Siegman, A. E., Orthogonality properties of optical resonator eigenmodes. *Opt. Commun.* **1979,** *31* (3), 369-373.
48. D. S. Indrasekara, A. S.; Thomas, R.; Fabris, L., Plasmonic properties of regiospecific core-satellite assemblies of gold nanostars and nanospheres. *PCCP* **2015,** *17* (33), 21133-21142.
49. Loebich, O., The optical properties of gold. *Gold Bull.* **1972,** *5* (1), 2-10.
50. Suarez, I.; Ferrando, A.; Marques-Hueso, J.; Diez, A.; Abargues, R.; Rodriguez-Canto, P. J.; Martinez-Pastor, J. P., Propagation length enhancement of surface plasmon polaritons in gold nano-/micro-waveguides by the interference with photonic modes in the surrounding active dielectrics. *Nanophotonics* **2017,** *6* (5), 1109-1120.
51. Kéna-Cohen, S.; Stavrinou, P. N.; Bradley, D. D. C.; Maier, S. A., Confined Surface Plasmon–Polariton Amplifiers. *Nano Lett.* **2013,** *13* (3), 1323-1329.
52. Tsoulos, T. V.; Han, L.; Weir, J.; Xin, H. L.; Fabris, L., A closer look at the physical and optical properties of gold nanostars: an experimental and computational study. *Nanoscale* **2017,** *9* (11), 3766-3773.
53. Atta, S.; Tsoulos, T. V.; Fabris, L., Shaping Gold Nanostar Electric Fields for Surface-Enhanced Raman Spectroscopy Enhancement via Silica Coating and Selective Etching. *J. Phys. Chem. C* **2016,** *120* (37), 20749-20758.
54. Weber, D.; Albella, P.; Alonso-González, P.; Neubrech, F.; Gui, H.; Nagao, T.; Hillenbrand, R.; Aizpurua, J.; Pucci, A., Longitudinal and transverse coupling in infrared gold nanoantenna arrays: long range versus short range interaction regimes. *Opt. Express* **2011,** *19* (16), 15047-15061.
55. Grzelczak, M.; Perez-Juste, J.; Mulvaney, P.; Liz-Marzan, L. M., Shape control in gold nanoparticle synthesis. *Chem. Soc. Rev.* **2008,** *37* (9), 1783-1791.
56. Funston, A. M.; Novo, C.; Davis, T. J.; Mulvaney, P., Plasmon Coupling of Gold Nanorods at Short Distances and in Different Geometries. *Nano Lett.* **2009,** *9* (4), 1651-1658.

57. Jain, P. K.; Huang, W.; El-Sayed, M. A., On the Universal Scaling Behavior of the Distance Decay of Plasmon Coupling in Metal Nanoparticle Pairs: A Plasmon Ruler Equation. *Nano Lett.* **2007,** *7* (7), 2080-2088.
58. Karabeber, H.; Huang, R.; Iacono, P.; Samii, J. M.; Pitter, K.; Holland, E. C.; Kircher, M. F., Guiding Brain Tumor Resection Using Surface-Enhanced Raman Scattering Nanoparticles and a Hand-Held Raman Scanner. *ACS Nano* **2014,** *8* (10), 9755-9766.
59. Jeanmaire, D. L.; Van Duyne, R. P., Surface raman spectroelectrochemistry: Part I. Heterocyclic, aromatic, and aliphatic amines adsorbed on the anodized silver electrode. *J. Electroanal. Chem. Interfacial Electrochem.* **1977,** *84* (1), 1-20.
60. Kleinman, S. L.; Frontiera, R. R.; Henry, A.-I.; Dieringer, J. A.; Van Duyne, R. P., Creating, characterizing, and controlling chemistry with SERS hot spots. *PCCP* **2013,** *15* (1), 21-36.
61. Moskovits, M., Persistent misconceptions regarding SERS. *PCCP* **2013,** *15* (15), 5301-5311.
62. Schlücker, S., Surface-Enhanced Raman Spectroscopy: Concepts and Chemical Applications. *Angew. Chem. Int. Ed.* **2014,** *53* (19), 4756-4795.
63. Indrasekara, A. S. D. S.; Paladini, B. J.; Naczynski, D. J.; Starovoytov, V.; Moghe, P. V.; Fabris, L., Dimeric Gold Nanoparticle Assemblies as Tags for SERS-Based Cancer Detection. *Adv. Healthcare Mater.* **2013,** *2* (10), 1370-1376.
64. Fabris, L.; Schierhorn, M.; Moskovits, M.; Bazan, G. C., Aptatag-Based Multiplexed Assay for Protein Detection by Surface-Enhanced Raman Spectroscopy. *Small* **2010,** *6* (14), 1550-1557.
65. Pandian Senthil, K.; Isabel, P.-S.; Benito, R.-G.; Abajo, F. J. G. d.; Luis, M. L.-M., High-yield synthesis and optical response of gold nanostars. *Nanotechnology* **2008,** *19* (1), 015606.
66. Xie, J.; Lee, J. Y.; Wang, D. I. C., Seedless, Surfactantless, High-Yield Synthesis of Branched Gold Nanocrystals in HEPES Buffer Solution. *Chem. Mater.* **2007,** *19* (11), 2823-2830.
67. Baginskiy, I.; Lai, T.-C.; Cheng, L.-C.; Chan, Y.-C.; Yang, K.-Y.; Liu, R.-S.; Hsiao, M.; Chen, C.-H.; Hu, S.-F.; Her, L.-J.; Tsai, D. P., Chitosan-Modified Stable Colloidal Gold Nanostars for the Photothermolysis of Cancer Cells. *J. Phys. Chem. C* **2013,** *117* (5), 2396-2410.
68. Harmsen, S.; Huang, R.; Wall, M. A.; Karabeber, H.; Samii, J. M.; Spaliviero, M.; White, J. R.; Monette, S.; O'Connor, R.; Pitter, K. L.; Sastra, S. A.; Saborowski, M.; Holland, E. C.; Singer, S.; Olive, K. P.; Lowe, S. W.; Blasberg, R. G.; Kircher, M. F., Surface-enhanced resonance Raman scattering nanostars for high-precision cancer imaging. *Sci. Transl. Med.* **2015,** *7* (271), 271ra7.
69. Nehl, C. L.; Hafner, J. H., Shape-dependent plasmon resonances of gold nanoparticles. *J. Mater. Chem.* **2008,** *18* (21), 2415-2419.
70. Liu, X.-L.; Wang, J.-H.; Liang, S.; Yang, D.-J.; Nan, F.; Ding, S.-J.; Zhou, L.; Hao, Z.-H.; Wang, Q.-Q., Tuning Plasmon Resonance of Gold Nanostars for

Enhancements of Nonlinear Optical Response and Raman Scattering. *J. Phys. Chem. C* **2014,** *118* (18), 9659-9664.

71. de Puig, H.; Tam, J. O.; Yen, C.-W.; Gehrke, L.; Hamad-Schifferli, K., Extinction Coefficient of Gold Nanostars. *J. Phys. Chem. C* **2015,** *119* (30), 17408-17415.

72. Guerrero-Martínez, A.; Barbosa, S.; Pastoriza-Santos, I.; Liz-Marzán, L. M., Nanostars shine bright for you: Colloidal synthesis, properties and applications of branched metallic nanoparticles. *Curr. Opin. Colloid Interface Sci.* **2011,** *16* (2), 118-127.

73. Rodríguez-Fernández, J.; Pastoriza-Santos, I.; Pérez-Juste, J.; García de Abajo, F. J.; Liz-Marzán, L. M., The Effect of Silica Coating on the Optical Response of Sub-micrometer Gold Spheres. *J. Phys. Chem. C* **2007,** *111* (36), 13361-13366.

74. Papirer, E., *Adsorption on Silica Surfaces*. Taylor & Francis: 2000.

75. Huang, Y.-F.; Wu, D.-Y.; Zhu, H.-P.; Zhao, L.-B.; Liu, G.-K.; Ren, B.; Tian, Z.-Q., Surface-enhanced Raman spectroscopic study of p-aminothiophenol. *PCCP* **2012,** *14* (24), 8485-8497.

76. Wang, Y. Q.; Liang, W. S.; Geng, C. Y., Shape evolution of gold nanoparticles. *J. Nanopart. Res.* **2010,** *12* (2), 655-661.

77. Grzelczak, M.; Pérez-Juste, J.; Mulvaney, P.; Liz-Marzán, L. M., Shape control in gold nanoparticle synthesis. *Chem. Soc. Rev.* **2008,** *37* (9), 1783-1791.

78. Wu, H.-L.; Chen, C.-H.; Huang, M. H., Seed-Mediated Synthesis of Branched Gold Nanocrystals Derived from the Side Growth of Pentagonal Bipyramids and the Formation of Gold Nanostars. *Chem. Mater.* **2009,** *21* (1), 110-114.

79. Park, K.; Drummy, L. F.; Wadams, R. C.; Koerner, H.; Nepal, D.; Fabris, L.; Vaia, R. A., Growth Mechanism of Gold Nanorods. *Chem. Mater.* **2013,** *25* (4), 555-563.

80. Barmparis, G. D.; Lodziana, Z.; Lopez, N.; Remediakis, I. N., Nanoparticle shapes by using Wulff constructions and first-principles calculations. *Beilstein J. Nanotechnol.* **2015,** *6*, 361-368.

81. Ringe, E.; Van Duyne, R. P.; Marks, L. D., Kinetic and Thermodynamic Modified Wulff Constructions for Twinned Nanoparticles. *J. Phys. Chem. C* **2013,** *117* (31), 15859-15870.

82. Sau, T. K.; Murphy, C. J., Room Temperature, High-Yield Synthesis of Multiple Shapes of Gold Nanoparticles in Aqueous Solution. *JACS* **2004,** *126* (28), 8648-8649.

83. Link, S.; El-Sayed, M. A., Spectral Properties and Relaxation Dynamics of Surface Plasmon Electronic Oscillations in Gold and Silver Nanodots and Nanorods. *J. Phys. Chem. B* **1999,** *103* (40), 8410-8426.

84. Millstone, J. E.; Park, S.; Shuford, K. L.; Qin, L.; Schatz, G. C.; Mirkin, C. A., Observation of a Quadrupole Plasmon Mode for a Colloidal Solution of Gold Nanoprisms. *JACS* **2005,** *127* (15), 5312-5313.

85. Meng, X.; Baride, A.; Jiang, C., Ligand Controlled Morphology Evolution of Active Intermediates for the Syntheses of Gold Nanostars. *Langmuir* **2016,** *32* (26), 6674-6681.
86. Yuan, H.; Khoury, C. G.; Hwang, H.; Wilson, C. M.; Grant, G. A.; Vo-Dinh, T., Gold nanostars: surfactant-free synthesis, 3D modelling, and two-photon photoluminescence imaging. *Nanotechnology* **2012,** *23* (7), 075102.
87. Supriya, A.; Laura, F., *Understanding the Role of AgNO3 Concentration and Seed Morphology to Achieve Tunable Shape Control in Gold Nanostars*. 2018.
88. Pallavicini, P.; Dona, A.; Casu, A.; Chirico, G.; Collini, M.; Dacarro, G.; Falqui, A.; Milanese, C.; Sironi, L.; Taglietti, A., Triton X-100 for three-plasmon gold nanostars with two photothermally active NIR (near IR) and SWIR (short-wavelength IR) channels. *Chem. Commun.* **2013,** *49* (56), 6265-6267.
89. Chirea, M.; Collins, S. S. E.; Wei, X.; Mulvaney, P., Spectroelectrochemistry of Silver Deposition on Single Gold Nanocrystals. *J. Phys. Chem. Lett.* **2014,** *5* (24), 4331-4335.
90. Fischer, D.; Pötschke, P.; Brünig, H.; Janke, A., Investigation of the Orientation in Composite Fibers of Polycarbonate with Multiwalled Carbon Nanotubes by Raman Microscopy. *Macromol. Symp.* **2005,** *230* (1), 167-172.
91. Kalampounias, A. G.; Tsilomelekis, G.; Boghosian, S., Unraveling the role of microenvironment and hydrodynamic forces on the vibrational relaxation rates of pyridine–water complexes. *J. Mol. Liq.* **2014,** *198* (Supplement C), 299-306.
92. Kalampounias, A. G.; Tsilomelekis, G.; Boghosian, S., Glass-forming ability of TeO(2) and temperature induced changes on the structure of the glassy, supercooled, and molten states. *J Chem Phys* **2015,** *142* (15), 154503.
93. Pötschke, P.; Brünig, H.; Janke, A.; Fischer, D.; Jehnichen, D., Orientation of multiwalled carbon nanotubes in composites with polycarbonate by melt spinning. *Polymer* **2005,** *46* (23), 10355-10363.
94. Mazzucco, S.; Geuquet, N.; Ye, J.; Stéphan, O.; Van Roy, W.; Van Dorpe, P.; Henrard, L.; Kociak, M., Ultralocal Modification of Surface Plasmons Properties in Silver Nanocubes. *Nano Lett.* **2012,** *12* (3), 1288-1294.
95. Bosman, M.; Ye, E.; Tan, S. F.; Nijhuis, C. A.; Yang, J. K. W.; Marty, R.; Mlayah, A.; Arbouet, A.; Girard, C.; Han, M.-Y., Surface Plasmon Damping Quantified with an Electron Nanoprobe. *Sci. Rep.* **2013,** *3*, 1312.
96. Hale, G. M.; Querry, M. R., Optical Constants of Water in the 200-nm to 200-μm Wavelength Region. *Appl. Opt.* **1973,** *12* (3), 555-563.
97. Johnson, P. B.; Christy, R. W., Optical Constants of the Noble Metals. *Phys. Rev. B* **1972,** *6* (12), 4370-4379.
98. Ondrej, L. K.; Tracy, C. L.; Matthew, F. M.; Gwyn, S.; Philip, E. B.; Niklas, D., Towards sub-10 meV energy resolution STEM-EELS. *Journal of Physics: Conference Series* **2014,** *522* (1), 012023.